

From the Cécile and Oskar Vogt Institute of Brain Research
at the Heinrich-Heine University Düsseldorf

**Scrutiny and Application of Deep-Learning Based Methods for Cortical
and Subcortical Brain Mapping in the BigBrain Model**

Dissertation

to Obtain the Degree of “Doctor of Philosophy” (PhD) in Medical Sciences
from the Medical Faculty of the Heinrich-Heine University

Submitted by

Kai Lars Kiwitz

2022

Als Inauguraldissertation gedruckt mit Genehmigung der Medizinischen
Fakultät der Heinrich-Heine-Universität Düsseldorf

gez.:

Dekan: Prof. Dr. med. Nikolaj Klöcker

Gutachter/innen: Prof. Dr. med. Katrin Amunts, Prof. Dr. med. Rüdiger Seitz

“The mind is not a book, to be opened at will and examined at leisure.”

- Severus Snape

Publications

Parts of this thesis have been published in:

Peer-Reviewed Journals

Kiwitz, K., Schiffer, C., Spitzer, H., Dickscheid, T., Amunts, K., 2020. Deep learning networks reflect cytoarchitectonic features used in brain mapping. *Sci Rep* 10, 22039. doi: 10.1038/s41598-020-78638-y.

Kiwitz, K., Brandstetter, A., Schiffer, C., Bludau, S., Mohlberg, H., Omidyeganeh, M., Massicotte, P., Amunts, K., 2022. Cytoarchitectonic Maps of the Human Metathalamus in 3D Space. *Front. Neuroanat.* 16, 837485. <https://doi.org/10.3389/fnana.2022.837485>.

Schiffer, C., Spitzer, H., Kiwitz, K., Unger, N., Wagstyl, K., Evans, A.C., Harmeling, S., Amunts, K., Dickscheid, T., 2021. Convolutional neural networks for cytoarchitectonic brain mapping at large scale. *NeuroImage* 240, 118327. <https://doi.org/10.1016/j.neuroimage.2021.118327>

Data Publications - High-Resolution Maps

Schiffer, C., Kiwitz, K., Amunts, K., and Dickscheid, T. Ultrahigh resolution 3D cytoarchitectonic map of Area hOc1 (V1, 17, CalcS) created by a Deep-Learning assisted workflow: EBRAINS. doi: 10.25493/DGEZ-Q93.

Schiffer, C., Kiwitz, K., Amunts, K., and Dickscheid, T. Ultrahigh resolution 3D cytoarchitectonic map of Area hOc2 (V2, 18) created by a Deep-Learning assisted workflow: EBRAINS. doi: 10.25493/FVBY-84C.

Schiffer, C., Kiwitz, K., Amunts, K., and Dickscheid, T. Ultrahigh resolution 3D cytoarchitectonic map of Area hOc3v (LingG) created by a Deep-Learning assisted workflow: EBRAINS. doi: 10.25493/PH0C-EKX.

Schiffer, C., Kiwitz, K., Amunts, K., and Dickscheid, T. Ultrahigh resolution 3D cytoarchitectonic map of Area hOc5 (LOC) created by a Deep-Learning assisted workflow: EBRAINS. doi: 10.25493/2V62-TTG.

Schiffer, C., Kiwitz, K., Brandstetter, A., Mohlberg, H., Amunts, K., and Dickscheid, T. Ultrahigh resolution 3D cytoarchitectonic map of the human Corpus geniculatum mediale (CGM, MGB, MGBv, MGBd, MGBm, metathalamus): EBRAINS. doi: 10.25493/PNY0-NCW.

Data Publications - Probability Maps

Kiwitz, K., Mohlberg, H., Brandstetter, A., Bludau, S., and Amunts, K.

Probabilistic cytoarchitectonic map of the human Corpus geniculatum laterale (CGL, LGB, metathalamus): EBRAINS. doi: 10.25493/1H7R-M3R.

Kiwitz, K., Mohlberg, H., Brandstetter, A., Bludau, S., and Amunts, K.

Probabilistic cytoarchitectonic map of the human Corpus geniculatum mediale (CGM, MGB, metathalamus): EBRAINS. doi: 10.25493/75TH-FE9.

Data Publications - Reference Delineations

Kiwitz, K., Schiffer, C., Brandstetter, A., Mohlberg, H., Amunts, K., and

Dickscheid, T. Reference delineations of the human Corpus geniculatum mediale (CGM, MGB, MGBv, MGBd, MGBm, metathalamus) in individual sections of the BigBrain: EBRAINS. doi: 10.25493/3SM6-HGM.

Kiwitz, K., Schiffer, C., Dickscheid, T., and Amunts, K. Reference delineations of Area hOc1 (V1, 17, CalcS) in individual sections of the BigBrain:

EBRAINS. doi: 10.25493/3GSV-T4A.

Kiwitz, K., Schiffer, C., Dickscheid, T., and Amunts, K. Reference delineations of Area hOc2 (V2, 18) in individual sections of the BigBrain: EBRAINS. doi:

10.25493/8MKD-D77.

Kiwitz, K., Schiffer, C., Dickscheid, T., and Amunts, K. Reference delineations of Area hOc3v (LingG) in individual sections of the BigBrain: EBRAINS. doi:

10.25493/DBZG-QZ.

Kiwitz, K., Schiffer, C., Dickscheid, T., Malikovic, A., and Amunts, K. Reference delineations of Area hOc5 (LOC) in individual sections of the BigBrain:

EBRAINS. doi: 10.25493/4027-K9Y.

Summary

Cytoarchitectonic maps provide important microanatomy based parcellations of the brain. The current state-of-the-art approach for cytoarchitectonic brain mapping involves image analysis techniques quantifying cytoarchitecture by extracting cortical profiles orthogonal to the cortical surface. Despite continuous improvements, this profile-based approach remains limited in throughput and is only applicable to cortical areas. We therefore investigated the quality and anatomical plausibility of a revised deep-learning based brain mapping approach in the BigBrain – a high-resolution 3D histological model of the human brain. In a first study, four visual cortical areas were mapped using the profile-based approach to train and apply the revised deep-learning approach to dense series of histological sections in the BigBrain. A second study expanded the use of the deep-learning based approach to a nucleus of the metathalamus to evaluate its subcortical applicability. Additionally, cytoarchitectonic probabilistic maps of the metathalamic nuclei were computed based on mappings in ten postmortem brains as part of the Julich-Brain atlas. In a third study, an evaluation of the operational mode of the revised deep-learning approach was performed by analyzing its internal structure with regards to representations of cytoarchitectonic features. An additional comparison to cytoarchitectonic features and borders positions reflected by the profile-based approach aimed at providing an independent verification of the deep-learning approach's validity.

The revised deep-learning approach was able to consistently map the four cortical visual areas as well as the subcortical metathalamic nucleus. Throughout their whole extent in the BigBrain, the maps showed a high degree of quality and anatomical plausibility with regards to topography and extent. Detected borders of cortical areas were co-localized to borders found by the profile-based approach and reproduced findings from subcortical maps in microscopic histological atlases, respectively. The analysis of the internal structure of the revised deep-learning approach revealed cytoarchitectonic feature representations especially on the laminar level. At the same time the new approach allowed mapping of large series of histological sections.

Our analyses demonstrate the potential to overcome limitations of the profile-based approach and provide a first step towards using deep-learning based brain mapping on a routine basis in high-resolution brain models like the BigBrain dataset. The generated maps are publicly available and will help future investigators to integrate the interoperable BigBrain with high-resolution neuroimaging data as well as to develop better and more realistic human brain models.

Zusammenfassung

Zytoarchitektonische Karten liefern wichtige mikroanatomische Parzellierungen des Gehirns. Die derzeitige Methode zytoarchitektonischer Parzellierung beruht auf Bildanalysetechniken, welche die Zytoarchitektur anhand orthogonal zur kortikalen Oberfläche extrahierter Profile quantifizieren. Trotz ständiger Verbesserungen ist dieser Ansatz in seiner Verarbeitungsmenge begrenzt und nur auf kortikale Bereiche anwendbar. Hier wird daher die Qualität und die anatomische Plausibilität eines Deep-Learning-basierten Hirnkartierungsverfahrens im BigBrain - einem hochaufgelösten histologischen 3D-Modell des menschlichen Gehirns - untersucht. In einer ersten Studie wurden vier visuelle kortikale Areale mit Hilfe des profilbasierten Ansatzes kartiert, um einen adaptierten Deep-Learning-Ansatz zur Hirnkartierung auf dichten Serien histologischer Schnitten im BigBrain zu trainieren und anzuwenden. In einer zweiten Studie wurde die Anwendung des Deep-Learning-Ansatzes auf einen Kern des Metathalamus ausgedehnt, um die subkortikale Anwendbarkeit zu bewerten. Zusätzlich wurden probabilistische zytoarchitektonische Karten metathalamischer Kerne auf der Grundlage von Kartierungen in zehn post-mortem Gehirnen als Teil des Jülich-Brain-Atlas berechnet. In einer dritten Studie wurde die Funktionsweise des Deep-Learning-Ansatzes evaluiert, indem die interne Struktur auf widergespiegelte zytoarchitektonische Merkmale hin analysiert wurde. Ein zusätzlicher Vergleich mit widergespiegelten zytoarchitektonischen Merkmalen und Grenzpositionen des profilbasierten Ansatzes ermöglichte eine unabhängige Überprüfung der Validität des Deep-Learning-Ansatzes.

Der adaptierte Deep-Learning-Ansatz war in der Lage, die vier kortikalen visuellen Areale sowie den subkortikalen metathalamischen Kern konsistent zu kartieren. Die Karten wiesen über ihre gesamte Ausdehnung im BigBrain ein hohes Maß an Qualität und anatomischer Plausibilität in Bezug auf Topographie und Ausdehnung auf. Die ermittelten Grenzen der kortikalen Areale waren mit den durch den profilbasierten Ansatz gefundenen Grenzen ko-lokalisiert und reproduzierten die Befunde subkortikaler Karten in histologischen Atlanten. Die Analyse der internen Struktur des adaptierten Deep-Learning-Ansatzes zeigte zytoarchitektonische Merkmalsrepräsentationen insbesondere auf der laminaren Ebene auf. Gleichzeitig ermöglichte der neue Ansatz die Kartierung großer Serien histologischer Schnitte.

Unsere Analysen zeigen das Potenzial auf, die Einschränkungen des profilbasierten Ansatzes zu überwinden und stellen einen ersten Schritt zur routinemäßigen Anwendung von Deep-Learning-basierter Hirnkartierung in hochaufgelösten Gehirnmodellen wie dem BigBrain-Datensatz dar. Die generierten Karten sind öffentlich zugänglich und werden zukünftigen Forschern helfen, das interoperable BigBrain mit hochauflösenden Bildgebungsdaten zu integrieren sowie bessere und realistischere menschliche Gehirnmodelle zu entwickeln.

List of Abbreviations

BA	Brodmann Area
fMRI	Functional Magnetic Resonance Imaging
GLI	Grey Level Index
LGB	Lateral Geniculate Body
MGB	Medial Geniculate Body
MNI	Montreal Neurological Institute
MRI	Magnetic Resonance Imaging
PLI	Polarized Light Imaging

Table of Contents

1	Introduction.....	1
1.1	Cytoarchitecture of the Human Brain.....	1
1.1.1	Early Cytoarchitectonic Maps: Strengths and Limitations	1
1.1.2	Principles of Cytoarchitectonic Organization.....	3
1.2	Atlas Concepts for Neuroimaging	5
1.2.1	Probabilistic Brain Mapping – The Julich-Brain.....	6
1.2.2	Overview of Subcortical Atlases of the Brain’s Microstructure.....	6
1.2.3	The BigBrain as a High-Resolution Anatomical Model and Reference Space.....	7
1.3	Methods for Cytoarchitectonic Brain Mapping.....	8
1.3.1	Visual Inspections and First Quantitative Methods	8
1.3.2	Profile-based Image Analysis for Cortical Mapping.....	8
1.3.3	Deep-learning Based Approaches	10
1.4	Target Areas for Studying Deep-Learning Based Approaches	12
1.4.1	The Visual Cortex.....	12
1.4.2	The Metathalamus.....	13
1.5	Aim of the Studies	15
2	Convolutional neural networks for cytoarchitectonic brain mapping at large scale, Schiffer, C., Spitzer, H., Kiwitz, K., Unger, N., Wagstyl, K., Evans, A.C., Harmeling, S., Amunts, K., Dickscheid, T., NeuroImage, 240, 118327 (2021)	17
3	Cytoarchitectonic maps of the human metathalamus in 3D space, Kiwitz, K., Brandstetter, A., Schiffer, C., Bludau, S., Mohlberg, H., Omidyeganeh, M., Massicotte, P., Amunts, K., Frontiers in Neuroanatomy, 16 (2022).....	33

4	Deep learning networks reflect cytoarchitectonic features used in brain mapping, Kiwitz, K., Schiffer, C., Spitzer, H., Dickscheid, T. & Amunts, K., Sci Rep, 10, 22039 (2020).....	46
5	Discussion	62
5.1	Accuracy and Quality of Deep-Learning Based Brain Mapping	62
5.2	The Internal Structure of Deep-Learning Based Brain Mapping Approaches.....	65
5.2.1	Resemblances to Traditional Cytoarchitectonic Features	66
5.2.2	Comparisons to Profile-based Image Analysis	67
5.3	Advantages of Deep-Learning Assisted Brain Mapping	69
5.3.1	Time Efficiency	69
5.3.2	Mapping of Subcortical Nuclei	69
5.4	Current and Future Relevance of High-Resolution Brain Maps in the 3D – BigBrain	70
5.4.1	Linking BigBrain Histology with Neuroimaging.....	70
5.4.2	Brain Simulation and Modelling	72
5.4.3	Conclusion	73
6	References	75

1 Introduction

1.1 Cytoarchitecture of the Human Brain

Since the second half of the 19th century the microscopic architecture of the human brain has been studied. Differentiating and defining the architecture of cells in the cerebral cortex (*cytoarchitecture*) is strongly linked to the advent of histology. In his famous work from 1872 (Meynert, 1872a), Viennese psychiatrist Theodor Meynert already described regional differences in the cellular architecture of cerebral grey matter in cell-stained brain sections – establishing the scientific field of *cytoarchitectonics*. Following Meynert's observations an early faction of neuroanatomists (Campbell, 1904; Flechsig, 1898; Smith, 1907) parcellated the cerebral cortex into distinct areas in the following years. Above all stands Korbinian Brodmann's famous characterization of 43 cortical areas of the human brain (Brodmann, 1909). As a student and employee of Cecile and Oskar Vogt in Berlin, he developed the still to this date used nomenclature of the Brodmann Areas (BAs). In the first half of the 20th century Brodmann's work inspired others to further develop the cytoarchitectonic parcellation of the human brain, especially the monumental work of v. Economo and Koskinas (Economo and Koskinas, 1925) and the upcoming Russian school (Sarkisov et al., 1949). The early histological works mainly focused on the cytoarchitecture of the cortex. It was only later that subcortical structures like the thalamus gained attention (Grünthal, 1934; Vogt and Vogt, 1941) resulting in subcortical parcellations half a century later than the cortical parcellations (Hassler, 1959).

1.1.1 Early Cytoarchitectonic Maps: Strengths and Limitations

Especially the early works of Brodmann (1909) still have a great impact on contemporary neuroscientific work. They have paved the way for analyzing structure-function relations of the human brain and comparative multimodal neuroanatomical studies (Zilles and Amunts, 2010). A reflection of this impact is the still used nomenclature of the Brodmann areas as topographic descriptors for brain areas. Brodmann's map and his methodology did not remain uncriticized though. Bailey and Bonin (1951) were among the first to

address the inherent lack of observer-independency and reproducibility with respect to Brodmann's parcellations. Another major drawback constituted interindividual differences in cytoarchitecture that remained neglected in Brodmann's single subject map (Lashley and Clark, 1946). Both aspects also apply to the works of Brodmann's followers who provided more detailed maps that yet shared the same limitations (Economo and Koskinas, 1925; Sarkisov et al., 1949). Furthermore, the focus on the cytoarchitecture of the cortex in the early works also impeded to study possible structure-function relationships of subcortical structures.

The advent of modern neuroimaging in the 1980s and the need for anatomical reference spaces and atlases has renewed the interest in the early works once more. Along with this development new, more observer-independent quantitative image analysis methodologies (Wree et al., 1982; Zilles et al., 1978) were developed to support the renewed interest in cytoarchitectonic brain mapping that led to the current state-of-the-art approach for cytoarchitectonic brain mapping (Amunts et al., 2020; Schleicher et al., 1999; Zilles et al., 2002). This approach helped to overcome the inherent drawbacks of missing objectivity and single subject maps. Yet, the creation of new high-resolution anatomical reference spaces and the inability to quantitatively map subcortical nuclei challenge currently used methodologies once more and have prompted the first implementations of deep-learning based solutions (Spitzer et al., 2018; Spitzer et al., 2017) whose scrutiny and application is explored in this thesis.

The remainder of this introduction gives an overview of principles of cytoarchitectonic organizations (chapter 1.1.2) before introducing cytoarchitectonic maps in the context of atlas concepts for neuroimaging (chapter 1.2). Current approaches for cortical and subcortical cytoarchitectonic brain mapping are reviewed in chapter 1.3.1 and 1.3.2 before introducing deep-learning based approaches as a potential candidate to overcome limitations of the currently applied approaches (chapter 1.3.3). Chapter 1.4 argues to assess the scrutiny and applicability of a revised deep-learning based approach based on the well-studied visual cortical areas and subcortical metathalamic structures which constitutes the motivation behind this thesis work.

1.1.2 Principles of Cytoarchitectonic Organization

The cerebral cortex (from here on called *cortex*) constitutes the phylogenetically youngest part of the human brain. It forms the outer layer of neural tissue of the cerebrum (grey matter) and can be classified into the six-layered isocortex and the three- to eleven-layered allocortex (Strominger et al., 2012; Zilles and Amunts, 2012). Neocortical layers stretch from the pia mater on the brain's surface to the underlying white matter and are numbered from I to VI forming a cortical thickness of the isocortex of roughly 1.8 to 3.8 mm (Economo and Koskinas, 1925). The horizontal organization of the estimated 16 billion neurons in the human cortex (Herculano-Houzel, 2009) into layers is accompanied by cortical columns and minicolumns that form an additional radial organizational principle (**Figure 1**). Analyzing the cellular composition of cortical layers reveals a characteristic distribution of neurons and their connections to other cortical and subcortical areas (**Figure 1**).

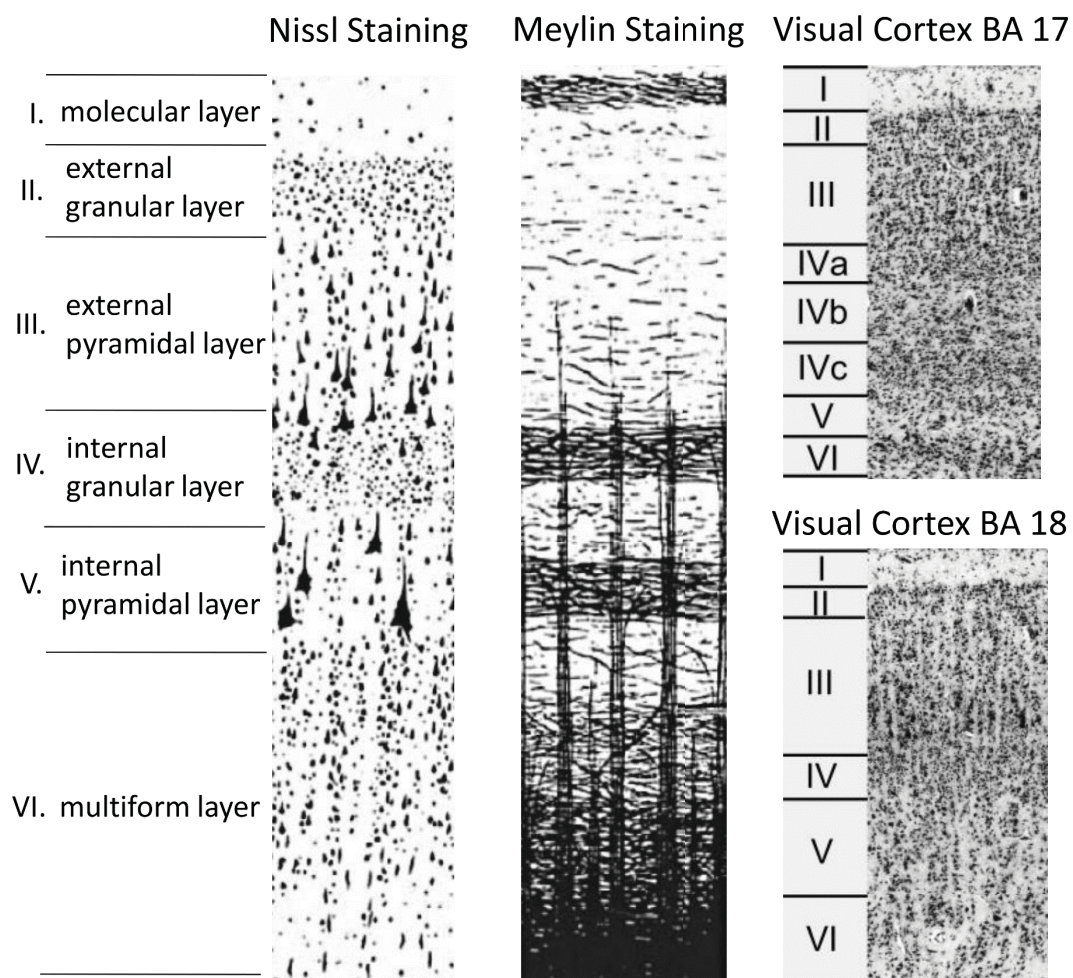


Figure 1: Schematic overview of cortical layers. The schematic representation of a cell-body stained image on the left shows the 6-layered neocortex with an accompanying fiber stained image in the middle showing vertical and horizontal axonal connections within the cortex (adapted and modified with permission from Amunts et al. (2010) © 2010 Springer and modified after Vogt and Vogt (1919)). Images on the right show the characteristic cellular composition of the cortical layers of the primary (BA 17) and secondary (BA 18) visual cortex on cell-body stained brain sections (adapted and modified after Kiwitz et al. (2020)). The secondary visual cortex shows clearly visible vertically-oriented cortical columns (layer III-V) in comparison to the primary visual cortex.

Differences in the cellular composition and laminar differentiation have led to the definition of cytoarchitectonic features including laminar thickness, laminar arrangement, as well as cell size, cell density, cellular clustering and the sharpness of the white matter/grey matter border that characterize the cytoarchitectonic appearance of a specific cortical region (Campbell, 1904; Economo and Koskinas, 1925; Flechsig, 1898; Smith, 1907). Due to the mostly missing laminar organization of subcortical nuclei, their delineation on cell-body stained sections mostly relies on cellular features like cell sizes and cell densities, as well as differences in cell morphology and the sharpness of borders to other subcortical nuclei.

1.2 Atlas Concepts for Neuroimaging

With the advent of modern neuroimaging it became possible to study the structural and functional organization of the living human brain. Along with the development of more and more advanced imaging techniques, milestone achievements regarding human cognition (Owen et al., 2005; Saxe and Kanwisher, 2003), neurodegenerative (Stoessl et al., 2011) and psychiatric diseases (Gong et al., 2019; Pantelis et al., 2003) as well as healthy brain function and development (Giedd et al., 1999; Raichle and Snyder, 2007) have been made.

From the beginning of modern neuroimaging on, the need for an anatomically plausible anchoring of imaging data increased the interest in the early cytoarchitectonic maps once more. To integrate structural and functional neuroimaging data, a common reference space was needed - of which the Talairach space was the first (Talairach and Tournoux, 1988). It incorporated a 3D-representation of Brodmann's map of cytoarchitectonic areas. The MRI-based MNI space (Evans et al., 2012) subsequently largely replaced the Talairach space. Other atlas concepts incorporated Brodmann's maps as well and helped to localize and quantify PET imaging data (Seitz et al., 1998; Seitz et al., 1990). Today, averaged reference spaces like the MNI ICBM 152 2009c nonlinear asymmetric space encompass interindividual variations (Evans et al., 2012), while disease- and ethnicity-specific reference spaces (Thompson et al.,

2001; Wang et al., 2013; Xiao et al., 2017) consider specific pathologies and populations.

1.2.1 Probabilistic Brain Mapping – The Julich-Brain

To overcome missing interindividual variations in existing atlases, advances in histological cytoarchitectonic brain mapping in the last 30 years have led to creating probabilistic atlases (Amunts et al., 2020; Amunts and Zilles, 2015; Eickhoff et al., 2005a; Mazziotta and Toga, 2002; Schleicher et al., 1999). The Julich-Brain (Amunts et al., 2020) for example constitutes a dynamic three-dimensional atlas of the brain's cortical and subcortical cytoarchitecture that incorporates probabilistic cytoarchitectonic maps of currently more than 200 areas. It also emphasizes the role of image analysis workflows to generate maps on a statistically reliable foundation. The integration into the MNI reference space makes the Julich-Brain interoperable with other brain atlases and resources. The cytoarchitectonic maps of the Julich-Brain are also included in frequently used toolboxes like SPM (Eickhoff et al., 2005b) and FSL (Jenkinson et al., 2012), as well as the EBRAINS multilevel human brain atlas (Amunts et al., 2022). This integration enables the neuroimaging community to link molecular, genomic, connectivity-based, and functional aspects of brain organization to the underlying cytoarchitectonic maps – contributing to the development of multimodal brain atlases (Amunts et al., 2020; Amunts and Zilles, 2015; Glasser et al., 2016; Toga et al., 2006).

1.2.2 Overview of Subcortical Atlases of the Brain's Microstructure

For subcortical structures the earliest implementation of histologically-derived maps into a reference space came from Schaltenbrand and Bailey (1959) who included the thalamic maps of Hassler (1959). Similar to Schaltenbrand and Bailey (1959), Mai et al. (2016) used fiber architectonic stainings to provide illustrations of the thalamus and basal ganglia, which was expanded by the stereotaxic atlas of Morel (2007) by additional staining procedures to define boundaries of thalamic nuclei normalized to the MNI space. Recently, Ding et al. (2016) provided an atlas that summarizes the contemporary knowledge regarding the microanatomy of subcortical nuclei. Unfortunately, similar to the first cortical maps, histological atlases of subcortical nuclei are often created on

the basis of a limited sample size (Ding et al., 2016; Mai et al., 2016; Morel, 2007).

The histologically-defined cytoarchitectonic parcellations of the Julich-Brain atlas and the aforementioned subcortical histological atlases constitute gold-standard references providing anatomical anchors for neuroimaging (Amunts et al., 2020; Pijnenburg et al., 2021), deep-brain stimulation (Chakravarty et al., 2006; Horn et al., 2019) and probabilistic in vivo MRI atlases (García-Gomar et al., 2019; Pauli et al., 2018; Saranathan et al., 2021). Yet, their integration into the MNI space relies on careful 3D-reconstructions (Amunts et al., 2020) and normalization is challenged by the limited anatomical detail of the MNI space, especially when anchoring small subcortical nuclei.

1.2.3 The BigBrain as a High-Resolution Anatomical Model and Reference Space

At the same time the spatial resolution of ultra-highfield functional MRI has increased to the submillimeter range in recent years, allowing for more and more detailed functional studies (Martino et al., 2018; van der Zwaag et al., 2016). This imposes further new challenges to link such data with the limited spatial resolution and anatomical details of the MNI space. For data integration on the level of cortical layers and columns, as well as small subcortical nuclei, a histological reference space that provides microscopic resolution is necessary. The BigBrain dataset based on its 7404 sections cell-body stained and 3D-reconstructed sections fulfils such requirements and provides an isotropic spatial resolution of 20 micrometers (Amunts et al., 2013). As such, it has previously been used to validate MRI based models of brain connectivity (Paquola et al., 2020b; Wei et al., 2019), functional and structural gradients (Paquola et al., 2019; Royer et al., 2020), as well as default mode network components (Paquola et al., 2019) by linking MRI-based measurements with the underlying microanatomy. Available transformations to the MNI space make it an interoperable high-resolution histological reference space for the neuroscientific community.

1.3 Methods for Cytoarchitectonic Brain Mapping

1.3.1 Visual Inspections and First Quantitative Methods

Brodmann (1909) and the other early 20th century neuroanatomists mainly used light-microscopy to delineate the cortex based on its cytoarchitectonic appearance. This procedure imposes a degree of subjectivity to the early cytoarchitectonic works – well reflected by the diverging numbers of delineated areas and their topography (Brodmann, 1909; Campbell, 1904; Smith, 1907; Zilles and Amunts, 2010). The subsequent analysis of the monumental work by Economo and Koskinas (1925) added quantitative criteria like mean cell sizes and densities for each cortical layer including their variability, as well as laminar and cortical thickness measurements to denote differences between cortical areas. The Economo atlas represents a whole-brain cytometric reference therein that is still used today to provide anatomical references for neuroimaging (Pijnenburg et al., 2021; Scholtens et al., 2015) and parameters for brain modelling (Pronold et al., 2018). Analyzing the microarchitecture of the brain using light-microscopy is nowadays accompanied by modern high-resolution tissue scanning technologies which enable the digitization of whole brain series of sections. Visual inspections using digitized sections and microscopes, as well as quantitative measures like cell counts and cell-densities remain important neuroanatomical tools to denote differences between brain areas. This is especially the case for subcortical areas for which a more observer-independent approach has not been established yet.

1.3.2 Profile-based Image Analysis for Cortical Mapping

On the cortical level, computerized image analysis workflows have enabled a more objective and reproducible identification of borders between cortical areas in the last 30 years (Schleicher et al., 2005; Schleicher et al., 1999; Schmitt et al., 2003; Zilles et al., 2002) – building the statistically reliable foundation of the Julich-Brain (Amunts et al., 2020). The current state-of-the-art method for quantitative cytoarchitectonic analysis uses a measure of the volume fraction of cell bodies – the grey level index (GLI) – extracted along profile traverses (Schleicher et al., 1999). The definition of the profiles follows the Laplacian field from the cortical layer I/layer II border to the white matter border on the GLI

images (Schleicher et al., 2005; Schleicher et al., 2000; Zilles et al., 2002) reflecting the cytoarchitecture of the analyzed region. Feature vectors of the profiles' shape functions are then extracted to analyze changes in cytoarchitecture. They contain the mean GLI value, the first four central moments about the mean: mean, standard deviation, skewness and kurtosis, as well as values of the feature vectors' first differential quotients (Schleicher et al., 1999; Zilles et al., 2002). A sliding-windows approach finally captures borders between cortical areas by calculating multivariate difference functions of the feature vectors while moving across the cortical ribbon (Schleicher et al., 1999).

Other profile-based approaches use excess mass functionals in the feature vectors to establish a relation to differences in cortical lamination in consecutive profiles (Schmitt et al., 2003) or wavelet analyses (Annese et al., 2004). The former reduces the complex shape of the profile to the number of local peaks and their differences, the later bundles profile data in large wavelet coefficients. Both have been applied in only a small number of applications.

A commonly shared drawback of the profile-based approach is that the extracted profiles only partly reflect traditional cytoarchitectonic criteria. It focuses more on statistical image criteria by relating the central moment parameters of profiles to aspects of cytoarchitecture, e.g., mean cell packing or differences in cell density between cortical layers (Schleicher et al., 2000; Zilles et al., 2002). Such a reasoning cannot be made unequivocally though, since one and the same profile can result from a higher density of small neurons or a lower density of large neurons (Schleicher et al., 2000). The conception to detect laminar differences in the cellular pattern also restricts the profile-based approach to analyzing the cytoarchitecture of the cortex – prohibiting a quantitative analysis of subcortical nuclei. Recent developments of high-resolution models like the BigBrain furthermore challenge the throughput of the labor- and time-intensive profile-based approach for future studies. This emphasizes the need for a more automatic, yet biologically valid alternative.

1.3.3 Deep-learning Based Approaches

Recently deep learning techniques have shown to be a new and promising alternative in the dynamically evolving field of medical image analysis (Komura and Ishikawa, 2018; Litjens et al., 2017; Madabhushi and Lee, 2016; Shen et al., 2017; Xing and Yang, 2016) to potentially overcome the limitations of the current profile-based approach. Adaptations for segmenting cortical areas of our group have demonstrated that deep-learning approaches generate more automatic, consistent segmentations across sections that are transferable to other brains with high throughput (Spitzer et al., 2018; Spitzer et al., 2017). These preliminary works nevertheless also showed that the existing methods are not yet accurate enough to effectively produce anatomically plausible segmentations (**Figure 2**). It is also unclear in how far they incorporate traditional cytoarchitectonic features and compare to the current profile-based approach. A more automatic classification of cytoarchitectonic areas remains challenging therefore and revised approaches to assist neuroanatomists with the time and labor intensive cytoarchitectonic mapping work are needed.

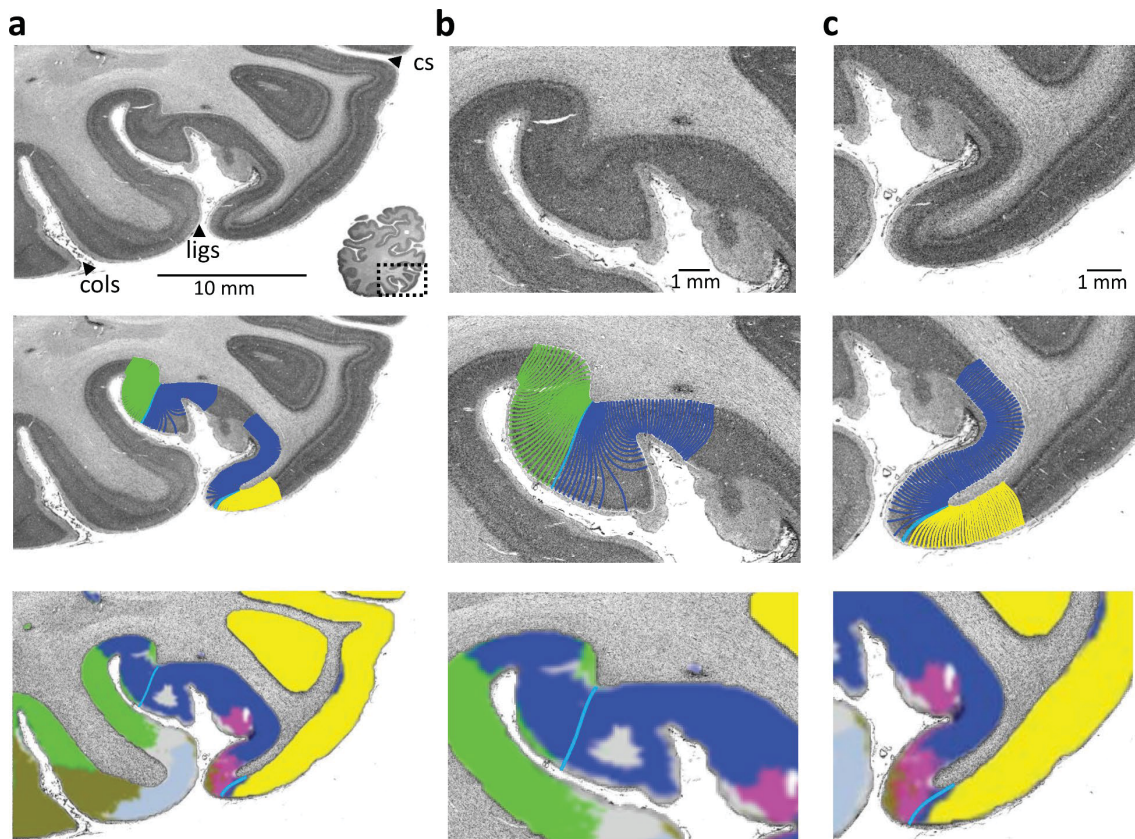


Figure 2: Comparing cytoarchitectonic brain mapping of visual cortical areas using profile-based and deep-learning based approaches. (a) upper image: excerpt from cell-body stained brain section of the left occipital lobe (adapted and modified with permission from Spitzer et al. (2017) © 2017 IEEE) of a postmortem brain that is part of the Julich-Brain (B1, section 1141 (Amunts et al., 2020)). The dashed box indicates the ventral part of the visual system with major sulci annotated (cs = calcarine sulcus, ligs = lingual sulcus, cols = collateral sulcus); middle image: statistically significant borders (cyan profiles) between the primary (yellow profiles), secondary (blue profiles) and ventrally adjacent (green profiles) visual cortex determined using the profile-based approach; bottom image: segmentations of seven visual cortical areas using a deep-learning based approach (Spitzer et al., 2017) with superimposed borders from the middle image. The depicted brain is part of the Julich-Brain **(b)** and **(c)** magnified excerpts from a) covering the secondary and ventrally adjacent (b) as well as primary and secondary (c) visual cortex (upper images) with borders determined by the profile-based approach (middle images) and segmentations of the deep-learning based approach (bottom images). The bottom images show that the deep-learning based segmentations do not match the border positions detected in (b) and misrepresent the topographic relation of the adjacent primary (yellow) and secondary (blue) visual cortex.

1.4 Target Areas for Studying Deep-Learning Based Approaches

1.4.1 The Visual Cortex

Studying the use of revised deep-learning approaches inevitably raises the question of target areas to test their performance and applicability on. As one of the most intensively studied parts of the mammalian brain (Espinosa and Stryker, 2012; Hubel and Wiesel, 1962; Tootell et al., 1988), the visual cortex constitutes a possible candidate to test and apply such new cytoarchitectonic mapping approaches.

The human visual cortex covers almost all of the occipital lobe of the brain and can be differentiated into a striate area (primary visual) mostly located inside the Calcarine sulcus (**Figure 2a**, upper image) and several extrastriate areas (Gennari, 1782; Meynert, 1872b). Like other parts of the cortex involved in sensory information processing, the visual cortex is characterized by its high granularity, i.e. a very pronounced layer II and IV (Orban et al., 2004). Layer IV of the primary visual cortex is further subdivided into multiple sublayers (**Figure 1**) and characterized by a “*tremendous abundance of granular cells*” (Economo and Koskinas, 1925), which contributes significantly to its striate appearance. The latter is especially apparent for sublayer IVc where visual information coming from the lateral geniculate body (LGB) of the metathalamus enters the cortex. Fiber-stained sections underline the special laminar characteristics by showing a distinct fiber bundle in sublayer IVb contemporaneously described by Francesco Gennari (Gennari, 1782) and Félix Vicq d’Azyr (Vicq-d’Azyr, 1786) from whose works the term *striate cortex* derives. The adjacent visual cortex maintains the clear laminar appearance by showing a very cell-sparse layer V in comparison to the cell-dense cortical layers IV and VI on cell-body stained sections (Amunts et al., 2000; Economo and Koskinas, 1925).

Retinotopically aligned information from the LGB enters layer IVc of the primary visual cortex with the horizontal meridian of the visual field represented in the fundus of the calcarine sulcus and the vertical meridian represented at the border to the secondary visual cortex (Abdollahi et al., 2014). The functional separation in the primary visual cortex including ocular dominance columns,

orientation columns as well as blob and inter-blob regions (Ts'o et al., 2009) has provided insights into the structural-function organization of early visual processing. These organizational principles build the foundation for higher visual processing in adjacent visual areas of the ventral and dorsal visual streams included in movement perception (Kolster et al., 2010; Malikovic et al., 2007), color perception (Nasr et al., 2016) as well as object and face recognition (Kanwisher et al., 1997; Weiner and Zilles, 2016). Early cytoarchitectonic works of Brodmann (1909) and Economo and Koskinas (1925) already established a widely accepted structural framework for visual information processing starting in the primary visual cortex (BA17 or OC after Economo and Koskinas' nomenclature) that transmits information via the dorsally and ventrally surrounding area BA18/OB to BA19/OA. This classical parcellation has been confirmed for BA17 and BA18 (Amunts et al., 2000) and more recent studies (Kujovic et al., 2013; Malikovic et al., 2016; Malikovic et al., 2007; Rottschy et al., 2007) have shown an even more differentiated parcellation of higher visual cortical areas than assumed in the classical works.

Studies investigating connectivity among visual cortical areas (Burkhalter and Bernardo, 1989; Caspers et al., 2015; Markov et al., 2014), have further shaped our understanding of the visual system - making it a holistically studied model system on a structural and functional level. The well-studied characteristics of the visual cortex have just recently been used to generate biologically-valid models of the macaque visual system (Schmidt et al., 2018) and create multimodal atlases of the human visual system (Rosenke et al., 2017). Especially the distinct cytoarchitectonic features of the early visual areas make it a suitable candidate system for scrutinizing the applicability of novel deep-learning based approaches for cytoarchitectonic brain mapping.

1.4.2 The Metathalamus

Before visual and auditory information enters the cortex, it is passed through the metathalamus. Its function as a subcortical relay station for visual and auditory information, makes it a target to expand the assessment of deep-learning based approaches to subcortical nuclei. The human metathalamus consists of two major nuclei: the lateral geniculate body (LGB) and the medial

geniculate body (MGB), which are located caudoventrally of the main body of the thalamus. The LGB receives visual information from axons of retinal ganglion cells covering the contralateral visual field via the optic tract. Afferents from layer 6 of the visual cortex and the reticular nucleus of the thalamus contribute information as well, modulating the retinogeniculate transmission (Sherman and Guillery, 2002). The human LGB has 6 layers, with 2 magnocellular and 4 parvocellular layers processing the functionally distinct magnocellular and parvocellular pathways from the retina separately for each eye. The most prominent efferent connection of the LGB constitutes the optic radiation which projects to the primary visual cortex. The LGB can be considered a visual relay station involved in sensory gating the thalamic output to the visual cortex (McCormick and Bal, 1994).

The MGB serves similar purposes for the auditory domain. It has previously been subdivided according to its cytoarchitecture into three major compartments: the ventral, dorsal and medial subdivisions (Ramón y Cajal, 1909; Winer, 1984). Evidence from studies in mammals support the notion that the ventral MGB receives ascending tonotopically-aligned projections via the medial lemniscus and inhibitory projections from the inferior colliculus (Caspary and Llano, 2017; Peruzzi et al., 1997; Saint Marie et al., 1997), whereas the dorsal and medial MGB receive input from the inferior colliculus, as well as feedback from the auditory cortex (Calford and Aitkin, 1983; Llano and Sherman, 2008). The ventral MGB has also been interpreted as a first-order sensory nucleus of the thalamus since it shows major projections to the auditory cortex (Malmierca et al., 2015; Winer et al., 2005). From a functional perspective, the MGB transforms the ascending sensory information and gates its saliency for its major output: the auditory cortex (Caspary and Llano, 2017; Winer et al., 1999).

Due to their importance for subcortical sensory information processing the LGB and MGB have previously been mapped as part of several subcortical atlases of the human brain (Ding et al., 2016; Mai et al., 2016; Morel, 2007; Schaltenbrand and Bailey, 1959). Recent efforts have been made to create *in vivo* subcortical atlases of the human thalamus (García-Gomar et al., 2019; Iglesias et al., 2018; Najdenovska et al., 2018) in combination with histological

maps (Ewert et al., 2018; Iglesias et al., 2018). Following this line, we sought to expand and scrutinize the applicability of deep-learning based approaches for cytoarchitectonic brain mapping with the MGB as a subcortical target area.

1.5 Aim of the Studies

The current state-of-the-art approach for cytoarchitectonic brain mapping has benefitted the field for the last 30 years by providing a statistically reliable image analysis framework. However, it is limited in throughput, which impedes brain mapping in high-resolution reference spaces like the BigBrain.

Furthermore, its application is not transferable to subcortical nuclei – emphasizing the need for an additional verification to perform such a task. Although contemporary deep-learning based cytoarchitectonic brain mapping approaches show first promising results to overcome throughput limitations, they are limited by two factors: They still lack sufficient anatomical plausibility to produce accurate cytoarchitectonic maps. Furthermore, it is unclear in how far they incorporate traditional cytoarchitectonic features and compare to resemblances of cytoarchitectonic features and border positions of the current profile-based approach.

Hence the first aim of this thesis was to provide an evaluation of the quality, plausibility and consistency of a revised deep-learning based brain mapping approach in the BigBrain targeting a broad range of visual cortical areas with different architecture in Study 1. Building up on previous deep-learning based approaches for mapping visual cortices (Spitzer et al., 2018; Spitzer et al., 2017), the evaluation was performed on automatically generated maps of four cortical visual areas including the primary and secondary visual cortex in the BigBrain model. Therefore, a few single sections were mapped using the profile-based approach, while remaining sections were filled using the deep learning approach to create high-resolution 3D reconstructions of the structures. The revised deep-learning based mapping approach was then expanded to the metathalamus, a subcortical nucleus of the diencephalon, in Study 2, to evaluate its applicability to mapping subcortical nuclei. In particular, the MGB was studied in complete histological sections resulting in high-resolution maps in the BigBrain that supplement already existing maps of the

lateral geniculate body (Brandstetter et al., 2021). Furthermore, cytoarchitectonic probabilistic maps of both nuclei of the metathalamus were computed based on their mappings in ten postmortem brain as part of Julich-Brain.

As a next step we evaluated in how far the revised deep-learning approach reflects traditional cytoarchitectonic features in Study 3. To do so, the internal structure of the revised deep-learning based approach was analyzed by using an application of the approach for identifying the primary and secondary visual cortex in the BigBrain from Study 1. Hereby we used the learned internal feature representations of the approach and compared them with the underlying histology. An additional comparison between the laminar and cellular features reflected by the current profile-based approach and the learned features of the deep-learning approach allowed for an independent verification and validity assessment. Taken together the performed studies aimed at evaluating the applicability of a revised deep-learning based approach on the basis of its quality, anatomical plausibility and validity in comparison to the current profile-based approach. All studies are covered by a vote (#4863) of the ethics committee of the Medical Faculty of the Heinrich Heine University Düsseldorf.

Study 1

Convolutional neural networks for cytoarchitectonic brain mapping at large scale

Schiffer, C.^{1,2}, Spitzer, H.³, Kiwitz, K.⁴, Unger, N.⁴, Wagstyl, K.⁵, Evans, A.C.⁶,
Harmeling, S.⁷, Amunts, K.^{1,4}, Dickscheid, T.^{1,4}

¹Institute of Neuroscience and Medicine (INM-1), Research Centre Jülich, Germany

²Helmholtz AI, Research Centre Jülich, Germany

³Institute of Computational Biology, Helmholtz Zentrum München, Germany

⁴Cécile & Oscar Vogt Institute for Brain Research, University Hospital Düsseldorf,
Heinrich-Heine-University Düsseldorf, Germany

⁵Wellcome Centre for Human Neuroimaging, University College London, London,
United Kingdom

⁶Department of Neurology & Neurosurgery, Montréal Neurological Institute (MNI),
McGill University, Montréal, Canada

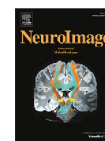
⁷Institute of Computer Science, Heinrich-Heine-University Düsseldorf, Germany



Contents lists available at ScienceDirect

NeuroImage

journal homepage: www.elsevier.com/locate/neuroimage



Convolutional neural networks for cytoarchitectonic brain mapping at large scale



Christian Schiffer^{a,b,*}, Hannah Spitzer^c, Kai Kiwitz^d, Nina Unger^d, Konrad Wagstyl^e, Alan C. Evans^f, Stefan Harmeling^g, Katrin Amunts^{a,d}, Timo Dickscheid^{a,b}

^a Institute of Neuroscience and Medicine (INM-1), Research Centre Jülich, Germany

^b Helmholtz AI, Research Centre Jülich, Germany

^c Institute of Computational Biology, Helmholtz Zentrum München, Germany

^d Céleste & Oscar Vogt Institute for Brain Research, University Hospital Düsseldorf, Heinrich-Heine-University Düsseldorf, Germany

^e Wellcome Centre for Human Neuroimaging, University College London, London, United Kingdom

^f Department of Neurology & Neurosurgery, Montréal Neurological Institute (MNI), McGill University, Montréal, Canada

^g Institute of Computer Science, Heinrich-Heine-University Düsseldorf, Germany

ARTICLE INFO

Keywords

Cytoarchitecture
Deep learning
Segmentation
Histology
Human brain
Brain mapping
Cortex

ABSTRACT

Human brain atlases provide spatial reference systems for data characterizing brain organization at different levels, coming from different brains. Cytoarchitecture is a basic principle of the microstructural organization of the brain, as regional differences in the arrangement and composition of neuronal cells are indicators of changes in connectivity and function. Automated scanning procedures and observer-independent methods are prerequisites to reliably identify cytoarchitectonic areas, and to achieve reproducible models of brain segregation. Time becomes a key factor when moving from the analysis of single regions of interest towards high-throughput scanning of large series of whole-brain sections. Here we present a new workflow for mapping cytoarchitectonic areas in large series of cell-body stained histological sections of human postmortem brains. It is based on a Deep Convolutional Neural Network (CNN), which is trained on a pair of section images with annotations, with a large number of un-annotated sections in between. The model learns to create all missing annotations in between with high accuracy, and faster than our previous workflow based on observer-independent mapping. The new workflow does not require preceding 3D-reconstruction of sections, and is robust against histological artefacts. It processes large data sets with sizes in the order of multiple Terabytes efficiently. The workflow was integrated into a web interface, to allow access without expertise in deep learning and batch computing. Applying deep neural networks for cytoarchitectonic mapping opens new perspectives to enable high-resolution models of brain areas, introducing CNNs to identify borders of brain areas.

1. Introduction

Human brain atlases provide a spatial framework for localizing information retrieved from neuroscientific studies of different brains, addressing brain organization from different angles and including different data modalities. The cerebral cortex of the brain is organized into cortical areas, which each have a specific functional role. They can be identified in cell body stained sections based on cytoarchitecture. Regional differences in the spatial arrangement and composition of the cells covary with changes in connectivity and function Goulas et al. (2018). Cytoarchitectonic borders can be identified in microscopic scans of histological brain sections, based on the analysis of the arrangement and distribution of cells, their different morphology and size, as well as differences in the appearance and relative thickness of cortical lay-

ers. Such criteria have been formulated for the first time more than a century ago to map the cerebral cortex, and still serve as guidelines for cytoarchitectonic analysis Amunts and Zilles (2015). Different approaches have been proposed in the past to identify positions of borders in a reliable manner Annese et al. (2004); Schleicher et al. (1999); Schmitt and Böhme (2002). The de-facto standard for identifying borders of cytoarchitectonic areas in the human cerebral cortex is a method based on multivariate statistical image analysis Schleicher et al. (1999), which has been applied for the identification of more than 200 areas to date Amunts et al. (2020). To map the whole extent of an area in both hemispheres, and to capture its intersubject variability through studies in large samples, however, is extremely time- and labor-intensive: Cytoarchitectonic maps need to aggregate properties across many histological sections and multiple brains. To address this challenge, mapping

* Corresponding author at: Institute of Neuroscience and Medicine (INM-1), Research Centre Jülich, Jülich, Germany.
E-mail address: c.schiffer@fz-juelich.de (C. Schiffer).

<https://doi.org/10.1016/j.neuroimage.2021.118327>

Received 25 November 2020; Received in revised form 5 May 2021; Accepted 30 June 2021

Available online 2 July 2021.

1053-8119/© 2021 The Authors. Published by Elsevier Inc. This is an open access article under the CC BY license (<http://creativecommons.org/licenses/by/4.0/>)

includes a subset of histological sections (every 15–60ths section, i.e. 0.3 mm to 1.2 mm distance between sections) of ten human postmortem brains resulting in analyses of several hundred sections per area, which corresponds to a workload in the order of one or even several person years per area Amunts et al. (2020).

Recent high-throughput scanning devices and powerful compute resources enable a much higher degree of automation in digitalization and analysis of whole human brain sections at microscopical resolution. Technological progress has made it possible to 3D-reconstruct a complete postmortem brain at 20 micron spatial resolution with more than 7000 sections - the BigBrain Amunts et al. (2013). This high-resolution brain model opens the possibility to produce complete maps of cytoarchitectonic areas at full microscopic resolution, and to cover large image stacks with brain areas extending across thousands of sections. Hereby, each section image has up to $120,000 \times 80,000$ pixels image size each. In order to address these challenges, a method is required, which

1. automatically classifies brain areas based on cytoarchitectonic criteria,
2. handles series with thousands of 2D images of histological sections with data in the Giga- to Terabyte range,
3. is robust against histological artefacts, which are inevitable in large section series,
4. provides stable results independently of the cutting plane, e.g. when changes in the cutting direction relative to the brain tissue prevents analysis of the 6-layered structure of the cerebral cortex (in the following referred to as *oblique cuts*), and
5. can be operated and supervised by neuroscience experts without requiring advanced computer science skills.

Previous experience in cytoarchitectonic mapping has shown that the identification of brain areas considers multiple parameters. This is true for traditional visual inspection using a light microscope, as well as for automated mapping approaches. It involves complex multi-scale texture patterns, from the level of neurons up to a level of cortical layers and areas. However, several parameters that can be used for identification of cortical areas heavily depend on the cutting plane of the histological sections with respect to the orientation of cortical columns. The highly folded cerebral cortex of the human brain hereby poses particular challenges, since brain areas may appear in a very different way in dependence on the cutting angle. Thus, brain mapping needs to operate in a variable data space, where no restrictions should be made on the orientation of the cutting plane relative to the course of cortical layers and the brain surface. In addition, automated brain mapping needs to consider variation in tissue quality and staining, as well as histological artefacts. Finally, automated mapping methods must take into account variations in cytoarchitecture between different brains and lead to identical parcellations, even if interindividual differences in cytoarchitecture are large.

Previous work on automated cytoarchitectonic area segmentation (Spitzer et al., 2017; 2018) proposes to use Convolutional Neural Networks (CNNs) for automatic segmentation of multiple cytoarchitectonic areas across multiple human brains. This is a remarkably challenging task, as the model needs to be robust against the considerable interindividual variability of the human brain, inevitable histological artefacts, variations in staining, and oblique cuts, to name only a few of the constraints. At the same time, it has to be highly sensitive to variations of cytoarchitecture in different brain areas, which may be subtle. This may result in a need for large amounts of training data, which is difficult to cover. Consequently, such generalized segmentation models are still subject to active research.

We here propose a new workflow for cytoarchitectonic mapping of a *target area* across large or complete series of histological human brain sections with a high degree of automation. The workflow is illustrated in Fig. 1. Following a “divide & conquer” approach, the full extent of a target brain area a is subdivided into intervals of sections, which are enclosed by annotations created at approximately regular section intervals.

Separate CNNs are then trained for each interval, using the enclosing annotations as training data. This results in a set of *local segmentation models*, each specialized to automatically map only the tissue sections which fall into the corresponding interval. By training local models for each interval of target area a , an interactive workflow is obtained that allows an expert to label cytoarchitectonic areas in full stacks of histological sections with minimal manual annotation, aided by Deep Learning, and at a speed that matches high throughput image acquisition.

In this work, we

1. introduce a method to automatically map cytoarchitectonic brain areas across large series of histological human brain sections (Section 2),
2. evaluate its precision on 18 cytoarchitectonic areas from the BigBrain dataset Amunts et al. (2013) to investigate its applicability to a wide range of different brain areas,
3. assess its precision for two areas in three brains with variable staining protocols Amunts et al. (2013, 2000); Ding et al. (2016) to investigate robustness against interindividual differences and different staining procedures, and
4. create highly detailed and complete 3D maps of four areas in the BigBrain dataset¹ and evaluate their anatomical plausibility.²

2. Materials and methods

2.1. GLI-based mapping of cytoarchitectonic areas for training and validation

Our proposed method requires annotations of the target area at roughly regular intervals in approximately 1% of sections in the stack. Such annotations consist of localizations of areal borders in the section, and are defined using the well-established GLI-based mapping procedure described in Schleicher et al. (1999). This approach starts by scanning the histological images and by building a Gray Level Index (GLI) image Schleicher et al. (1999). The GLI is a measure of the volume fraction of cell bodies Wree et al. (1982). In a next step, profiles extending from the cortical surface to the white matter border are extracted along Laplacians, which reflect laminar changes in the volume fraction of cell bodies, and thus encode cytoarchitecture. These Laplacians reflect an important feature of cortical cytoarchitecture, i.e. its columnar structure Schleicher et al. (2000). The cortical surface and the white matter border are manually identified. Using a sliding window procedure across the cortical ribbon, the similarity of blocks of profiles is being estimated by the Mahalanobis distance, a multi-variate distance measure, at each position, that is combined with a Hotelling’s t -test for checking significance. Borders between areas are indicated by significant peaks in the Mahalanobis distance function. The positions of borders are then labeled in the image. These borders are then used as a basis for the network training and validation.

2.2. Datasets

The datasets used in this study comprise image series of histological sections of three human brains, which have been stained for neuronal cell bodies Amunts et al. (2020); Ding et al. (2016). The brains vary in terms of cytoarchitecture and folding pattern, as well as staining properties, presence of histological artifacts and other features (Fig. 2). Areas have been mapped in the past (cf. Section 2.1) using at least every 60th section of the series. These maps provide the basis to train the neural network models and to perform automatic segmentation in previously unseen, close by sections.

¹ <https://www.bigbrainproject.org>

² The maps are released in the public domain as part of the multilevel human brain atlas in the EBRAINS platform <https://www.ebrains.eu>

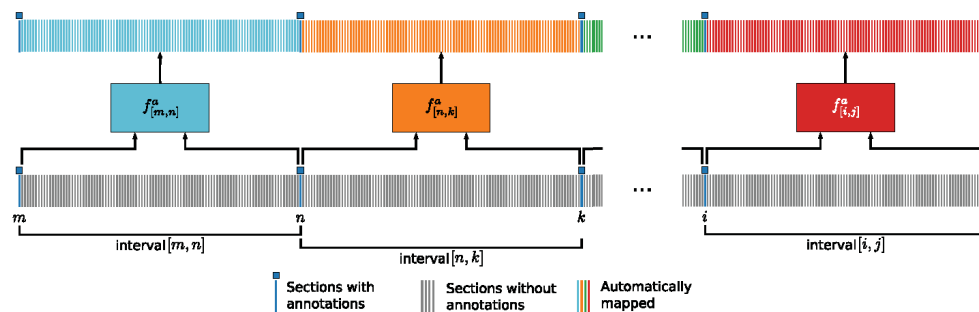


Fig. 1. Setup of our workflow. Images of histological sections are depicted as thin vertical bars, neural network models are depicted as colored boxes. The full extent of sections containing a target brain area a (sections m to j , bottom row) is subdivided into section intervals, which are defined by annotations at regular intervals (blue squares, m, n, k, \dots). One local segmentation model $f_{[m,n]}^a$ is trained for each interval enclosed by a pair of annotations $[m, n]$. After training, each model is applied to automatically map sections falling into the corresponding interval. (For interpretation of the references to color in this figure legend, the reader is referred to the web version of this article.)

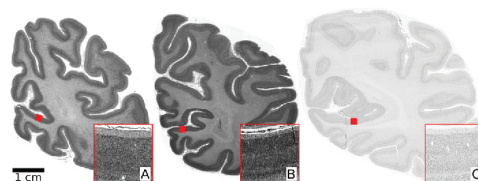


Fig. 2. Example images of cell body stained histological human brain sections taken from datasets B20(A), B01(B) and AAHB (C). All sections were sampled from a comparable region of the occipital lobe. Differences arise from intersubject variability and variations in staining and histological processing protocols. Locations of detail views ($2\text{ mm} \times 2\text{ mm}$) are marked with red squares. For B20 and B01, only the right hemisphere is shown. AAHB only includes a single hemisphere. Cerebellum was removed from B20 and AAHB for visualization. Scale bar: 1 cm (same for all three sections). (For interpretation of the references to color in this figure legend, the reader is referred to the web version of this article.)

The first dataset - denoted as B20 - is based on the original histological sections of the publicly available microscopic 3D model BigBrain (Amunts et al., 2013). The dataset consists of images of 7404 coronal sections with a thickness of $20\ \mu\text{m}$. A modified Merker stain (Merker (1983)) was used to stain cell bodies. A subset of sections was scanned at $1\ \mu\text{m}$ resolution using a high-throughput light-microscopic scanner (TissueScope HS, Huron Digital Pathology Inc.). Annotations based on the GLI-based method (Section 2.1) at an interval of approximately 60 sections ($\approx 1.2\text{ mm}$) were obtained for 18 cortical areas, belonging to different functional systems:

1. Visual areas $hOc1$, $hOc2$ (Amunts et al., 2000), $hOc3v$ (Rottschy et al., 2007) and $hOc5$ (Malikovic et al., 2007). Additional annotations at an interval of approximately 30 (0.6 mm) sections were created for $hOc5$, as well as on a small set of sections containing $hOc3v$ (Kowitz et al., 2019a; 2019b; 2020a; 2020b).
2. Areas of the frontal operculum $Op5$, $Op6$ and $Op7$ Unger et al. (2020a, 2020b, 2020c).
3. Areas 44 and 45 of Broca's region (Amunts et al., 1999; 2004) in the inferior frontal gyrus.
4. Areas $hIP5$, $hIP6$, $hIP7$ and $hIP8$ (Richter et al., 2019) in the intraparietal sulcus.

5. Supplementary motor area SMA and pre-supplementary motor area $preSMA$ Ruan et al. (2018).
6. Premotor areas $6d1$, $6d2$ and $6d3$ Sigl (2018); Sigl et al. (2019a, 2019b, 2019c).

The BigBrain dataset has been fully reconstructed at $20\ \mu\text{m}$ Amunts et al. (2013) and therefore opens the possibility to investigate the 3D consistency of the computed maps after transformation into the reconstructed space.

Brain areas differ in cytoarchitecture, as well as in size and in how much the morphology of an area changes across a series of consecutive brain sections. This has implications for the amount of annotations required to capture the relevant properties of certain areas. For example, $hOc1$ is large and shows only moderate changes across consecutive sections. In comparison, $hOc5$ is considerably smaller, and $hOc3v$ changes considerably across consecutive sections (see Fig. 10, C-F), resulting in a need for more annotations to capture their structure.

The second dataset - B01 - has also been used for mapping in the past, whereby every 15th section of the whole series of sections was stained and digitized. This brain was 3D reconstructed with a spatial resolution of 1 mm isotropic Amunts et al. (2020). Annotations for visual areas $hOc1$ and $hOc2$ at an interval of approximately every 60th section (Amunts et al., 2000) in a subset of sections have been used. This dataset serves to investigate robustness against intersubject variability, while the lab protocol is similar to the one used for B20.

The third dataset - AAHB - comes from the Allen Adult Human Brain Atlas Ding et al. (2016). It includes 106 unevenly spaced, publicly available sections. In contrast to the first two series of images, it differs in thickness ($50\ \mu\text{m}$), and the staining method (Nissl staining). Annotations are provided for cortical and subcortical gray matter according to a modified Brodmann scheme on one hemisphere (cf. (Ding et al., 2016)). This dataset is used to investigate robustness of the proposed method against variable lab protocols and delineation criteria with respect to areas $hOc1$ and $hOc2$, which correspond to "primary visual cortex (striate cortex, area $V1/17$)" (identifier 10269) and "parastriate cortex (area $V2$, area 18)" (identifier 10271), respectively, in the Allen ontology.

2.3. Local segmentation models

Annotations of cytoarchitectonic areas based on GLI mapping (Section 2.1) were used to train CNNs, which we refer to as local segmentation models. Each local segmentation model $f_{[s_1, s_2]}^a$ was trained on two sections s_1 and s_2 (the training sections) with available annotations for a target area a . Trained local segmentation models were then applied

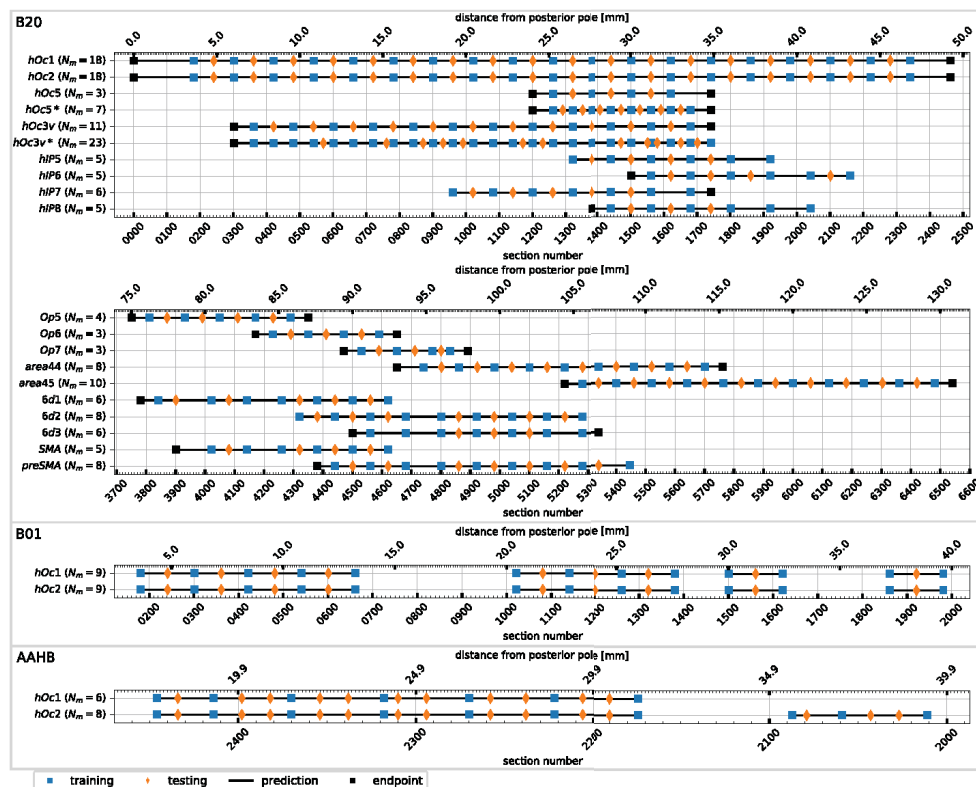


Fig. 3. Training and test sections from available annotations across stacks of histological sections. Consecutive pairs of training sections (blue squares) induce one local segmentation model. For example, model $f_{[181,301]}^{B20-hOc1}$ was trained on sections 181 and 301 of dataset B20, segments area *hOc1* in the full interval [182,300], and was tested on Section 2.1. N_m denotes the number of trained local segmentation models. * marks experiments performed with a smaller training interval. (For interpretation of the references to color in this figure legend, the reader is referred to the web version of this article.)

to “fill the gaps”, i.e. to automatically segment the target area in sections enclosed by the respective training sections s_1 and s_2 (Fig. 1). The focus on a single target area and a spatially restricted stack of consecutive sections reduces cytoarchitectonic and morphological variations that need to be captured by the respective models, which we expect to result in improved performance compared to training models for multiple areas or a wider range of sections as proposed in Spitzer et al. (2017).

We trained local segmentation models for 18 cytoarchitectonic areas in B20 and two areas in each of B01 and AAHB. Fig. 3 gives an overview of sections used for the individual areas. Most local segmentation models were trained on two training sections with annotations at ~ 2.4 mm distance, corresponding to ~ 120 sections for B20 and B01 and 48 sections for AAHB. Additional local segmentation models with a reduced interval size of 60 sections (1.2 mm) were trained for areas *hOc3v* and *hOc5* to account for highly variable morphology (*hOc3v*, see Fig. 10, C-F) and small area size (*hOc5*). For B01 and AAHB, local segmentation models were trained only for ranges of sections where annotations were available at the required interval. Segmentations of the outer most parts of cytoarchitectonic areas which were not enclosed by training sections (i.e. Sections 1 to 181 for *hOc1* in B20) were processed using the closest

available local segmentation model. For example, model $f_{[181,301]}^{B20-hOc1}$ was also applied to the section interval [1, 181].

2.4. Neural network architecture

For local segmentation models, the modified U-Net architecture (Ronneberger et al., 2015) proposed by Spitzer et al. (2017) was extended into a multi-scale neural network model (Fig. 5, C). U-Nets have proven to be very powerful for many applications in biomedical image segmentation (e.g. (Çiçek et al., 2016; Milletari et al., 2016)). They consist of an encoder and decoder branch, which are linked by skip-connections between layers of corresponding spatial resolution to allow recovery of fine-grained details during upsampling. Compared to the U-Net (Ronneberger et al., 2015), the modified architecture (Spitzer et al., 2017) employs additional encoder layers and a different number of filters to make processing of large image patches computationally tractable. To show the benefit of using a multi-scale variant of U-Nets, three network variants were used: A high-resolution encoder network (HR), a low-resolution network (LR), and a combined multi-scale architecture (MS).

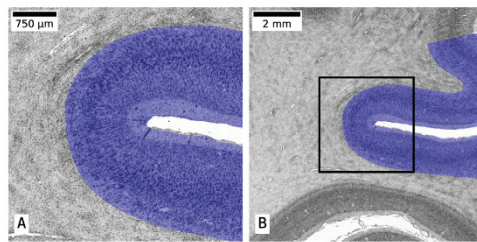


Fig. 4. Typical input patches for the proposed MSArchitecture. A high-resolution image patch (A, 2 μm per pixel) resolves fine-grained microstructural texture, while a lower resolution image patch (B, 16 μm per pixel) provides more information on macroanatomical context. The black rectangle indicates the position of patch (A) inside patch (B). Expert annotations of area $hOc2$ are overlaid in blue. (For interpretation of the references to color in this figure legend, the reader is referred to the web version of this article.)

High-resolution encoder architecture (HR)

The architecture proposed in Spitzer et al. (2017) was used as base architecture (Fig. 5, A). A high-resolution encoder E_{HR} receives high-resolution input patches with a size of 2025×2025 pixels at 2 μm pixel resolution ($4.05 \times 4.05 \text{ mm}^2$, Fig. 4, A) and enables recognition of fine-grained microstructural textures. It consists of six convolutional blocks, with the number of filters set to {16, 32, 64, 64, 128, 128} respectively. All but the last block are followed by a max-pooling operation with pool size 2 and stride 2. The first layer of the first block in E_{HR} uses a filter size of 5 and a stride of 4, which increases the receptive field while keeping memory consumption and computational effort tangible. All remaining convolutional layers of E_{HR} use a kernel size of 3 and stride 1. Following (Spitzer et al., 2018), we initialize E_{HR} from a network that has been pre-trained on a self-supervised task, specifically on predicting the geodesic distance along the brain surface between image patches from the BigBrain dataset. This auxiliary task has been shown to promote extraction of distinctive cytoarchitectonic features. The decoder consists of four convolutional blocks with the number of filters set to {128, 64, 64, 32} respectively. Each block is preceded by an upsampling block, which consists of a nearest neighbor upsampling with kernel size 2 and stride 2, followed by a zero-padded convolutional layer with kernel size 2 and stride 1. All convolutional operations in the network are followed by batch normalization Ioffe and Szegedy (2015) and Rectified Linear Unit (ReLU) non-linearity.

Multi-scale network architecture (MS)

The multi-scale network architecture was obtained by attaching a low-resolution encoder F_{LR} as a second branch to HR, which receives lower resolution image patches with a size of 682×682 pixels at 16 μm pixel resolution ($10.912 \times 10.912 \text{ mm}^2$), centered at the same location as E_{HR} patches (Fig. 4). This branch allows to learn features at the scale of local cortical folding patterns. Although such macroscopic features are not generally representative of cytoarchitecture in human brains, as they vary largely between individuals (Amunts and Zilles, 2015), they are appropriate in the present setting due to the locality of the network models. F_{LR} is based on E_{HR} , and composed of six convolutional blocks with the same number of filters as E_{HR} . All convolutional filters use a filter size of 3 and a stride of 1. Convolutional layers in the first block use a dilation rate of 1, while all other convolutional layers within F_{LR} use a dilation rate of 2 to enlarge the receptive field.

Low-resolution encoder architecture (LR)

The third architecture is based on HR, but replaces the encoder F_{HR} with F_{LR} (Fig. 5, B). By design, this model can only recognize macroscopic tissue features, and no detailed cytoarchitectonic properties at the level of cell bodies.

2.5. Training strategy

Stochastic gradient descent with Nesterov momentum (Sutskever et al., 2013) was used as optimizer for training the neural network models. Training was performed for 3000 iterations. The learning rate was initially set to 0.01 and decreased by a factor of 0.5 after 1000, 1400, 1800, 2200 and 2600 iterations. Momentum was set to 0.9. Categorical cross-entropy with a weight decay of 0.0001 was used as loss function.

Background class labels

Spitzer et al. (2017) reported convergence problems when training models with a single background class that includes both white and gray matter components, resulting in a mix of tissue parts with very high and very low similarity to the target area under the same classification label. Thus, the general background class was split into separate labels for gray matter (cor) and white matter (wm), resulting in a semantic segmentation problem with the four classes bg , wm , cor , and the target area a . For splitting the background class into wm and cor , different strategies were used for each dataset:

1. For B20, a volumetric tissue classification presented in Lewis et al. (2014) was projected onto the 2D histological sections using transformations provided by the authors of Amunts et al. (2013).
2. For B01, the gray white matter segmentation described in Spitzer et al. (2017) was used.
3. For AAHB, the respective delineations available from the Allen ontology Ding et al. (2016) were used.

Patchwise training

The full resolution scans of the whole-brain sections are by far too large to be used for training. Thus, a patchwise training procedure as also proposed in Ronneberger et al. (2015), Spitzer et al. (2017, 2018) was employed. However, due to the locality of local segmentation models, patches were sampled only in the direct proximity of the target brain area a , to effectively teach the models to distinguish a from its immediate surroundings. Only pixels with a distance of 5 mm or less to any pixel annotated as a were considered as potential center points for training patches.

Data augmentation

The following data augmentations were employed to simulate most frequently observed variations in the data: Both at test and training time, images were rotated by multiples of 90 degrees so that the y axis of coronal sections matches approximately the cranial direction. Random rotation by an angle sampled from a uniform distribution with support $[-45, 45]$ were applied to account for small differences in rotation angle. Intensity variations were addressed by random pixel intensity augmentation with the function $f(x) = \alpha x^\gamma + \beta$. The same intensity transformation is applied to all pixels of a training patch. Parameters were chosen from uniform distributions with $\alpha \sim U[0.9, 1.1]$, $\beta \sim U[-0.2, +0.2]$ and $\gamma \sim U[0.8, 1.214]$. The range of each parameter was empirically chosen to reflect natural variations occurring in the data.

Implementation

Training was performed on the supercomputer JURECA³ at the Jülich Supercomputing Centre at Research Centre Jülich (JSC) Krause and Thörnig (2018). Each compute node was equipped with four NVIDIA K80 GPUs with 12 Gigabyte of VRAM, 2 Intel Xeon E5-2680 v3 Haswell CPUs (12 2.5 GHz cores with hyperthreading each) and 128 Gigabyte of RAM (Krause and Thörnig, 2018). Training of one model occupied one GPU node, using all 4 GPUs and all 48 threads. Of the available 48 threads, 4 were assigned to one GPU each to coordinate the training process, while the remaining 44 threads read training patches from disk in a streaming fashion, applied data

³ https://www.fz-juelich.de/ias/jsc/EN/Expertise/Supercomputers/JURECA/JURECA_node.html

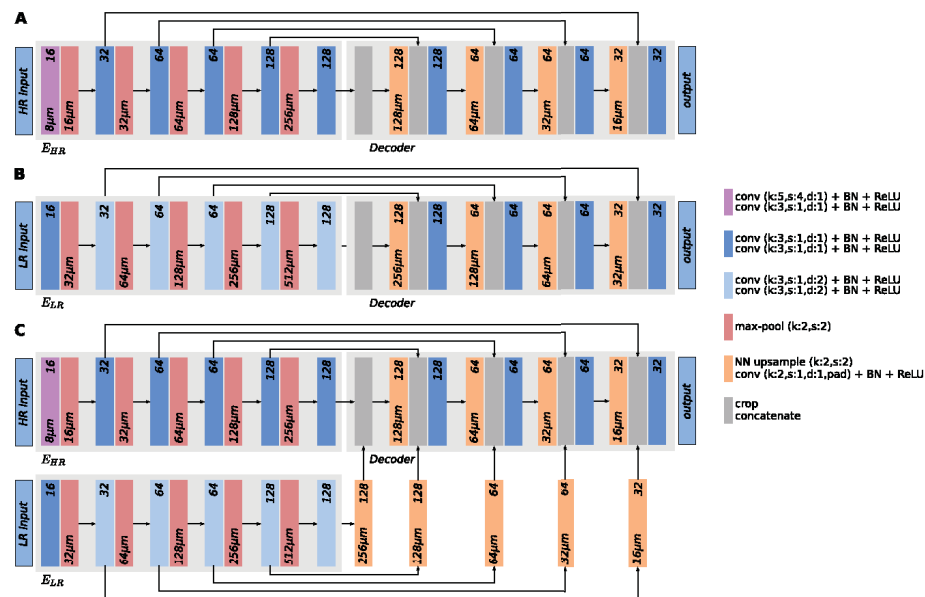


Fig. 5. Illustration of investigated neural network architectures. A: High-resolution architecture (HR) from (Spitzer et al., 2017), which can capture fine-grained microstructural textures. B: Low-resolution architecture (LR), which can capture macroscopic tissue features. C: Proposed multi-scale architecture (MS) to capture both fine and coarse grained tissue features. E_{HR} is pre-initialized with weights of the self-supervised network proposed in Spitzer et al. (2018). Numbers at the top of each block denote the number of filters used in the convolutional layers of this block. Numbers at the bottom denote the physical output spacing in μm per pixel for layers which change the physical spacing of the features.

augmentation and sent data to the training threads. Inter-process communication was implemented based on Message Passing Interface (MPI) using *mpi4py* (Dalcin et al., 2011). Training was implemented using *TensorFlow* (Abadi et al., 2016). Distributed training was performed using *Horovod* (Sergeev and Del Balso, 2018) and synchronous distributed stochastic gradient descent. Batch size was set to 16 image patches per GPU, resulting in a total effective batch size of 64 patches per iteration. The linear learning rate scaling rule for distributed training proposed in Goyal et al. (2017) was employed, scaling the learning rate by the number of GPUs.⁴ Batch normalization statistics were computed independently for each GPU and not averaged during training. Software code is publicly available⁵.

2.6. Web-based interactive workflow for efficient cytoarchitectonic mapping

The proposed workflow was implemented as an interactive web application (Fig. 6) to provide direct user control over the segmentation workflow through a web browser.⁶ The application allows entering annotations in a sparse set of reference sections, controlling the training workflow on a remote cluster, and efficiently inspecting predicted segmentations in the complete stack of histological sections. It does not require in-depth expertise in Deep Learning and/or batch computations.

⁴ Since we use a relatively small number of employed GPUs however, we do not apply the initial learning rate warm up phase described in Goyal et al. (2017).

⁵ Code available at <https://jugit.fz-juelich.de/c.schiffer/atlas>

⁶ Code available at <https://jugit.fz-juelich.de/c.schiffer/atlasui>

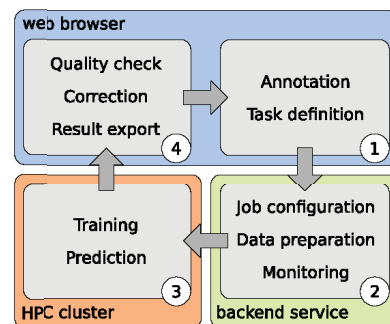


Fig. 6. Overview of the mapping workflow. The user starts by creating annotations (1) of a brain area a using the web-based annotation tool *microdraw*, and defines training tasks by specifying which annotations should be used to train local segmentation models (Section 2.5). Annotations and task definitions are then submitted to a backend web service (2) which prepares the data for training and submits a job to a HPC cluster. Training and subsequent prediction are performed on the HPC system (3). Obtained results can be viewed directly in *microdraw* for quality control (4). The user may decide to export results of sufficient quality for subsequent processing steps (e.g. 3D reconstruction), manually refine the predictions directly in *microdraw*, or repeat the workflow with additional annotations to improve performance.

Technically, it is designed as an extension of the web based annotation tool *microdraw*⁷, combined with a novel backend service that controls data exchange and job supervision on an ssh-accessible compute cluster. We used the workflow on the JURECA supercomputer at the Jülich Supercomputing Center (JSC). It uses common and freely available software components, and is portable to other sites, potentially requiring site-specific adjustments to account for differences in the software stack, scheduling system and data access.

The workflow typically iterates through the following steps:

1. The user enters annotations for a target brain area a in two tissue sections s_1 and s_2 , enclosing a local stack interval of ≈ 100 sections using *microdraw*, and this way defines a local segmentation model $f_{[s_1, s_2]}^a$ (Section 2.3).
2. A training task for the local segmentation model is submitted as a job to a GPU cluster at the push of a button, using default parameters (Section 2.5). It does not require any further configuration. Training typically takes 70 min on one compute node of the JURECA supercomputer. Multiple jobs can be submitted in parallel, if the cluster allows.
3. After training, predictions for all sections in the interval are automatically generated. For a large area like $hOc1$, this takes approximately 30 min for 120 sections. Computed segmentations are automatically displayed in the web frontend once they become available. Data synchronization between the web server and compute nodes is handled by the backend service.
4. After inspecting the segmentation quality, the user can choose to enter additional training data, either reducing the size of the current interval or initiating the next interval in the stack.

2.7. Validation framework and strategy

Additional sections with annotations in between the training sections were used for validating performance of local segmentation models on sections that were not seen during training (orange diamonds in Fig. 1). Segmentations of these test sections were quantitatively evaluated using the F1 score (also known as Dice score or Sørensen-Dice index), computed as the harmonic mean of precision of recall. Auxiliary labels added to ensure convergence (Section 2.5) were excluded from F1 score calculation, as the focus lies on segmentation performance for target area a .

Similar to the proximity sampling strategy employed for training (Section 2.5), segmentations on sections not seen during training were only created and evaluated in the approximate region containing a on the respective sections. These approximate regions were determined by projection of the closest reference annotations for a to the image in question using conventional linear image registration based on robust image features as in Dickscheid et al. (2019).

The benefit of a multi-scale architecture was investigated by training separate local segmentation models with neural network architectures HR, LR and MS for all areas in B20. For HR and MS, the high-resolution encoder E_{HR} was initialized with the weights of the network from Spitzer et al. (2018). Furthermore, the performance of multiple local segmentation models, each trained on a local subset of sections as described in Section 2.3, was compared to the performance of one single model trained on all annotations available for a target area a in the following way: For each target area in the B20 dataset, one model was trained using the union of all training sections of the local segmentation models (blue squares in Fig. 1), using the same training strategy as for local segmentation models. We conducted these experiments using HR, LR and MS architectures, and denote models trained on the whole stack as HR (ALL), LR (ALL) and MS (ALL), respectively, again pre-initializing the high-resolution encoder E_{HR} with weights from Spitzer et al. (2018)

The robustness of the proposed method against intersubject variability in brain structure and differences in staining protocols was investigated by training local segmentations models (with MS architecture) for areas $hOc1$ and $hOc2$ in datasets B01 and AAHB. To better understand the roles of the low and high-resolution branches (E_{LR} and E_{HR}) in the MS architecture, an experiment similar to occlusion sensitivity analysis (Zeiler and Fergus, 2014) was performed: Using model $f_{[90, 110, 121]}^{hOc2}$ which implements the MS architecture, we investigated how predictions change when we set the input patch for either E_{LR} or E_{HR} to zero, effectively preventing information extraction using the respective branch.

2.8. Generating high-resolution 3D cytoarchitectonic maps in the BigBrain dataset

Non-linear transformations described in Amunts et al. (2013); Omidyeganeh et al. (2020) from 2D histological sections into 3D reconstructed space available for the BigBrain dataset Amunts et al. (2013) were used to generate 3D maps for areas $hOc1$, $hOc2$, $hOc3v$ and $hOc5$ from 2D segmentations produced by our method. Segmentations were obtained using the workflow described in Section 2.3 and checked for quality by an expert (e.g. plausibility and consistency across consecutive sections). For areas $hOc3v$ and $hOc5$, results of segmentation models trained with a training interval size of 1.2 mm were used for reconstruction (marked with * in Fig. 3). Between 8% ($hOc3v$) and 23% ($hOc1$) of sections containing the investigated areas were not used for reconstruction due to histological artifacts (e.g. resulting from long-term storage or staining inhomogeneities). Segmentations that passed the quality check were transformed into the 3D reconstructed space. Excluded sections were replaced by interpolations from neighboring sections, using Laplacian fields as proposed in Schober et al. (2016).

Resulting 3D maps were smoothed using a median filter with kernel size $11 \times 11 \times 11$ pixel to compensate for small artefacts. The size of the filter was chosen to match the expected precision of annotations at boundaries (not higher than 100 μm), translating to 5 voxels at the target resolution of 20 μm . Furthermore, connected component analysis on the smoothed volume was performed to determine and remove spurious false positive predictions outside the target area, relying on the assumption that cytoarchitectonic areas are continuous in 3D. Only components with a minimum volume of 27 mm^3 ($3 \text{ mm} \times 3 \text{ mm} \times 3 \text{ mm}$) were kept. Effects of median filtering and connected component filtering are illustrated in Fig. 7.

To assess the improvement in 3D consistency and anatomical plausibility gained by the proposed workflow, a reference reconstruction of area $hOc1$ was computed, which performs a direct 3D interpolation between reference annotations obtained by GJI mapping. This reference reconstruction does not use the local segmentation models, and relies only on reference annotations and 3D reconstruction. It was computed by transforming the annotations of the training sections (blue squares in Fig. 3) into the 3D reconstructed space, and filling the gaps by Laplacian field interpolation (Schober et al., 2016).

The anatomical consistency of 3D reconstructed maps was further evaluated by computing their volume and surface area, which were then compared to reference values from Amunts et al. (2000). The volume of each area was computed by counting the total number of labeled voxels and multiplying the result by the physical size of each voxel.

The surface area was computed by first extracting a closed surface mesh of each area using the marching cubes algorithm Lewiner et al. (2003). The subset of mesh vertices lying on the pial surface was then determined by including all triangles where the cortical depth Bok (1929) was smaller than 0.25. To obtain the cortical depth of each mesh vertex, the procedure described in LePrince et al. (2015) was applied to the cortical ribbon defined by the gray and white matter segmentation provided with the BigBrain model (Lewis et al., 2014). The result was a volumetric dataset with voxels in the white matter labelled 1, voxels outside the brain labelled

⁷ <http://microdraw.pasteur.fr>

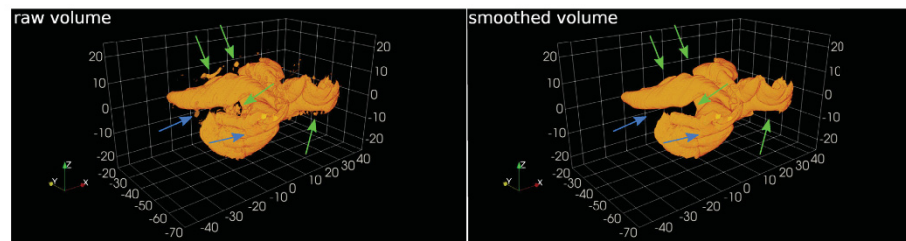


Fig. 7. Effects of median filtering and connected component filtering using the example of *hOc1*. Median filtering smooths the volume and removed small errors originating from registration errors or incorrect predictions (blue arrows). Filtering of small connected components removed small clusters of false positives from the volume (green arrows). Axes *x*, *y* and *z* correspond to left-to-right, posterior-to-anterior and ventral-to-dorsal directions, respectively. Axis labels are specified in mm and correspond to positions in the 3D reconstructed BigBrain space. See Fig. 14 for more images of *hOc1* from different viewing angles. (For interpretation of the references to color in this figure legend, the reader is referred to the web version of this article.)

0, and voxels inside the isocortex labelled with values between 0 and 1, representing their cortical depth according to the equivolometric model (Bok, 1929). Cortical depths of mesh vertices were then looked up in this volume. Finally, the surface area of the pial surface for each cytoarchitectonic area was computed by summing up the area of all triangles associated to the pial surface.

Both volume and surface area measurements were corrected for tissue shrinkage Amunts et al. (2000). The volume-based shrinkage factor for B20 has been determined in Amunts et al. (2005) based on the fresh weight and the volume after histological processing as $f_V = 1.931$. From this, an area-based (2D) shrinkage factor of $f_A = f_V^{2/3} = 1.551$ was derived.

3. Results

Differences in performance were observed depending on the network architecture (HR, LR, MS), the training setting (global vs. local segmentation models), the considered brain area, as well as the distance between annotated brain sections.

All architectures except for LR (ALL) show comparably good performance for *hOc1*. For most areas however, LR and MS achieved higher performance than other investigated models. For areas *hOc3v* and *hOc5*, where additional models were trained with reduced distance between training sections (indicated by * in Fig. 8), performance of LR and MS increased when reducing the distance between training sections, while only minor improvements were observed for the remaining architectures.

Representative image patches segmented by the MS architecture for each investigated area extracted from test sections of B20 are shown in Fig. 9. True positive, false positive and false negative predictions are indicated in green, red and blue, respectively. A large share of incorrectly classified pixels belonged to cortical regions with highly oblique cutting angles (Fig. 10 B, C). While large rifts tended to be excluded from the prediction (Fig. 10, A), smaller rifts or tissue foldings were correctly segmented as surrounding area (Fig. 9, A, D, E, G, O).

Scores obtained for areas *hOc1* and *hOc2* were overall consistent across different brain samples (Fig. 11). In all three cases, scores obtained for *hOc2* were lower compared to *hOc1*. Lowest median F1 score for *hOc2* was obtained for B20, along with an increased variance. Example patches showing the border between *hOc1* and *hOc2* on test sections extracted from approximately identical brain regions in the three datasets are shown in Fig. 12.

Models trained on all sections (HR (ALL), LR (ALL), MS (ALL)) obtained lower mean and median F1 scores than their locally trained counterparts HR, LR, and MS (Table 1). LR (ALL) and HR (ALL) showed comparable performance, MS (ALL) performed slightly better. The lowest

Table 1

F1 score statistics computed across all areas and test sections in the B20 dataset: obtained by the different network architectures HR, LR and MS (trained on local intervals), as well as HR (ALL), LR (ALL) and MS (ALL) (trained on all annotated sections per area). Higher mean/median values and lower standard deviation mean better performance.

model	median	mean	std
HR(all)	0.5319	0.5680	0.2075
LR(all)	0.5648	0.5533	0.1723
MS(all)	0.5869	0.6020	0.1973
HR	0.6294	0.6130	0.2105
LR	0.7439	0.7036	0.1865
MS	0.7469	0.7200	0.1825

scoring local model HR performs better than the highest scoring global model MS (ALL). Both LR and MS resulted in higher mean and median F1 scores than HR, with lower standard deviations. Highest mean and median performance was obtained by MS (Table 1, Fig. 8).

Setting the input patch of either E_{LR} or E_{HR} to zero provides indication on the influence of different scales in the proposed MS architecture (Fig. 13): Having access to only low-resolution image information, the model still identifies the approximate location of area *hOc2*, but with poorly defined borders. Using only high-resolution information, the model captures finer details, but has difficulties localizing the area correctly. When the model has access to both high- and low-resolution information, this results in better agreement with the reference annotations.

Locations, orientations and shapes of reconstructed 3D maps (computed using steps described in Section 2.8) were anatomically plausible and consistent (Fig. 14). The 3D map of *hOc5* showed partially missing extremal ends along the posterior anterior axis. Volume and surface estimates from the 3D maps reported in Table 2 corresponded well with the numbers reported in Amunts et al. (2000). Surface areas of *hOc1*, *hOc2* and *hOc5* were largely confirmed with the reference values, as well as the volumes derived from automatic segmentations of areas *hOc1* and *hOc2*. The reconstructed volume of area *hOc5* stood out by being considerably smaller than the reference volume.

Comparison of corresponding 3D reconstructions of area *hOc1* (Fig. 14 E vs. F) showed that the proposed approach provided anatomically more consistent results than direct spatial interpolation of GLI-based annotations, while both build on the same annotation effort. 3D interpolation produced abrupt transitions in anterior-posterior direction

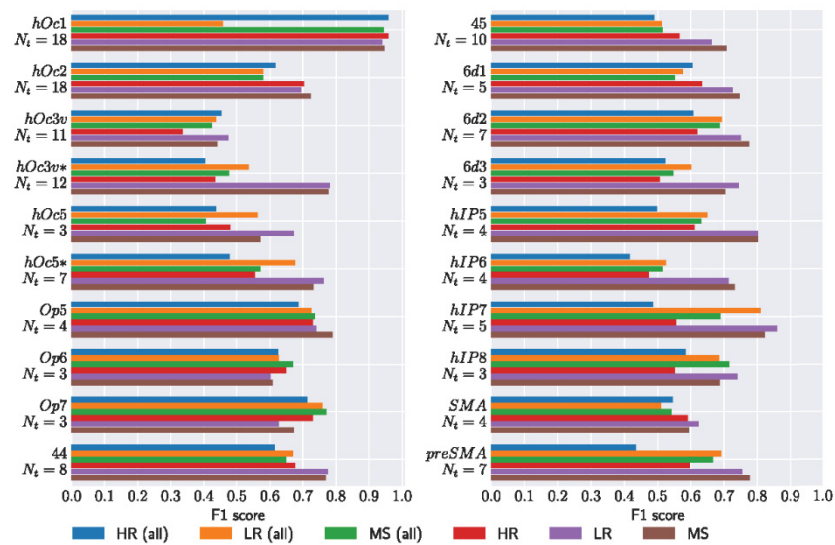


Fig. 8. Median F1 scores for HR (ALL), LR (ALL), MS (ALL), HR, LR and MS per investigated brain area in dataset B20. N_t denotes the number of test sections for which F1 scores were computed for a particular area. * indicates where training of local segmentation models was performed with reduced distance between training sections. Higher values denote better performance.

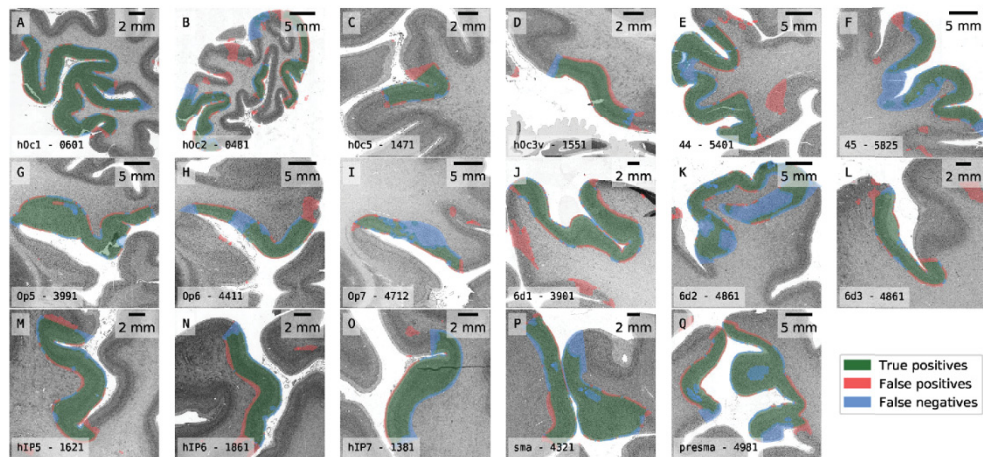


Fig. 9. Example image patches and corresponding model predictions extracted from test sections of B20 segmented using the proposed MSarchitecture. One image patch is shown for each investigated cytoarchitectonic area. Colors green, red and blue indicate true positive, false positive and false negative predictions, respectively. (For interpretation of the references to color in this figure legend, the reader is referred to the web version of this article.)

(Fig. 14, F, 1) and only captured structures already contained in the reference annotations, leading to inconsistencies near fine-grained morphological structures (e.g. Fig. 14 F, 2 and 3). The proposed method often produced reasonable segmentations for sections outside the training interval (Fig. 14, E, 1), which interpolation cannot provide by definition.

4. Discussion

In this work, we proposed a novel Deep Learning based workflow to create segmentations of cytoarchitectonic areas in large series of histological human brain sections using only a limited set of manually created annotations. We evaluated this approach across different cytoar-

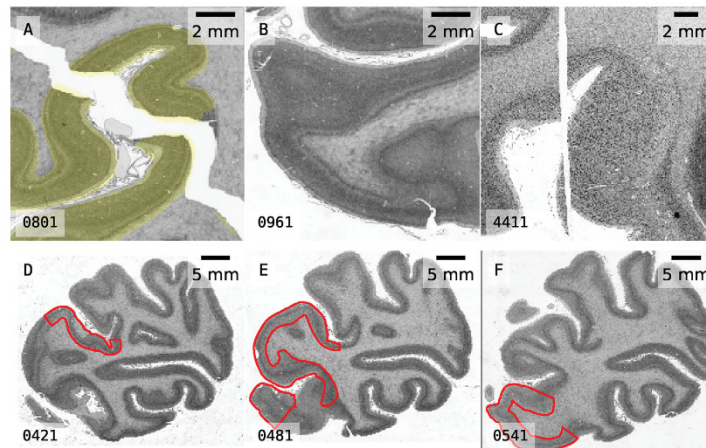


Fig. 10. Image patches extracted from B20 showing common challenges encountered during manual and automated cytoarchitectonic mapping. *A*: Mechanical damages resulting from histological processing. Prediction for *hOc1* shown in yellow demonstrate handling of larger mechanical damages. *B*: Region where the cutting angle is highly oblique, leading to partial or full occlusion of cortical layer structure (*oblique cuts*). *C*: Mechanically damaged and obliquely cut tissue. *C-P*: Example illustrating highly variable morphology of area *hOc3v* (highlighted in red) across 120 histological sections in B20. (For interpretation of the references to color in this figure legend, the reader is referred to the web version of this article.)

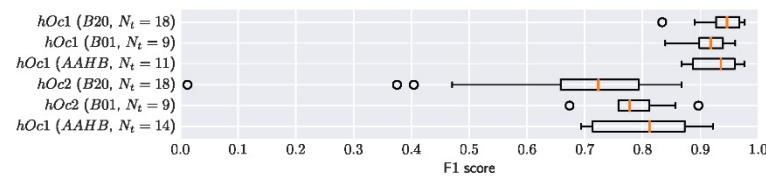


Fig. 11. F1 scores for segmentations of *hOc1* and *hOc2* obtained by the MSArchitecture on test sections of datasets B20, B01 and AAHB. N_t denotes the number of test sections for which F1 scores were computed for a particular area.

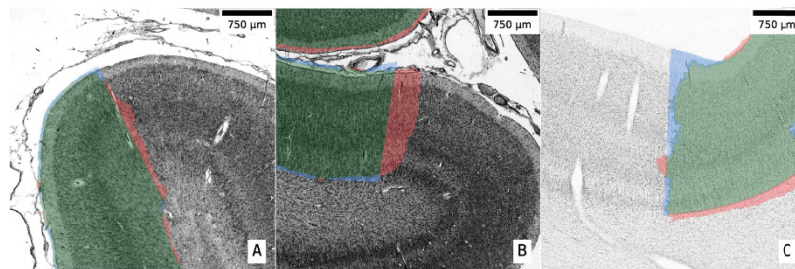


Fig. 12. Example patches and typical segmentation results extracted from test sections in datasets B20 (A), B01 (B) and AAHB (C). All three patches show the segmentation of *hOc2* obtained by a local segmentation model with MSArchitecture. Patches were extracted at the border between *hOc1* and *hOc2* and in comparable regions of the respective brain. Colors green, red and blue indicate true positive, false positive and false negative predictions, respectively (see also legend in Fig. 9). (For interpretation of the references to color in this figure legend, the reader is referred to the web version of this article.)

chitonic areas, brain samples and staining protocols. As a concrete use case, we then applied it to create high-resolution 3D maps of areas *hOc1*, *hOc2*, *hOc3v* and *hOc5* in the BigBrain Amunts et al. (2013).

4.1. Quality of derived 3D maps in the BigBrain

The proposed method produced 3D maps with a high degree of anatomical consistency and identified cytoarchitectonic areas precisely in the histological brain sections. Partially missing extremal ends re-

main a challenge, as seen in anterior-posterior direction of *hOc5*. Such parts are often difficult to identify even using manual methods. Therefore, training data for such extremal ends is difficult to obtain. The segmentation of extremal ends could potentially be addressed by providing additional GLI-based mappings (at the cost of additional annotation effort), or by an explicit shape-based inference step on top of the pixel segmentation. The 3D map of *hOc1* created with the proposed method is superior to the map obtained by direct spatial interpolation between GLI-based annotations. Methods based on 3D interpolation inherit any

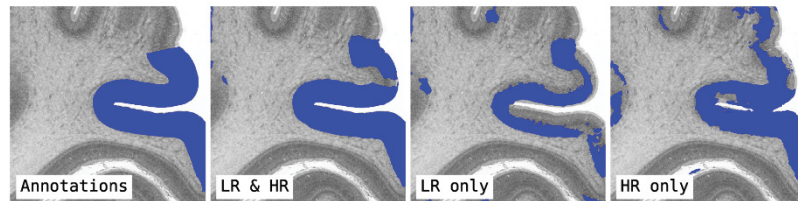


Fig. 13. Reference annotations and predictions of area *hOc2* (blue) for an example patch from section 961 of the B20dataset. Predictions were obtained by using both low- and high-resolution information (**LR & HR**), only low-resolution (**LR only**), and only high-resolution information (**HR only**). The input image patch for E_{LR} and E_{HR} was set to zero to investigate the role of low- and high-resolution image information, respectively. Predictions were created with model $f_{[901,1921]}^{hOc2}$ using the MSarchitecture. (For interpretation of the references to color in this figure legend, the reader is referred to the web version of this article.)

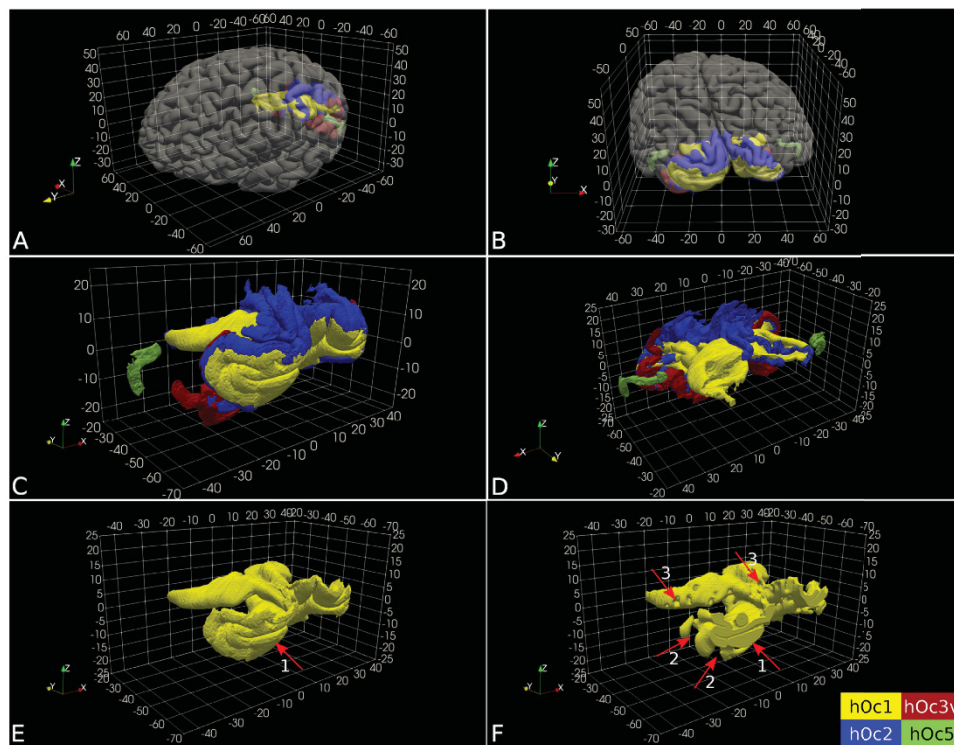


Fig. 14. 3D maps of visual cytoarchitectonic areas *hOc1* (yellow), *hOc2* (blue), *hOc3v* (red) and *hOc5* (green), obtained by transforming the independent 2D segmentations generated by the proposed method into the 3D reconstructed space of the B20dataset. *A+B*: Spatial embedding of reconstructed areas into the 3D reconstructed BigBrain volume. *C+D*: Detailed view of reconstructed cytoarchitectonic areas. *E+F*: Comparison of *hOc1* reconstructed based on our proposed method (*E*) and based on an interpolation between annotations in the reconstructed space, using Laplacian fields as proposed in Schöber et al. (2016) (*F*). Arrows in *F* mark example locations demonstrating shortcomings of the interpolation based reconstruction. Axes *x*, *y* and *z* correspond to left-to-right, posterior-to-anterior and ventral-to-dorsal directions, respectively. Axis labels are specified in mm and correspond to positions in the 3D reconstructed BigBrain space. (For interpretation of the references to color in this figure legend, the reader is referred to the web version of this article.)

Table 2

Estimated volumes (in mm^3) and surface areas (in mm^2) of brain areas derived from the full 3D maps in the 3D reconstructed space of the B20 dataset. Reference mean μ and standard deviation σ were computed based on male subjects from (Amunts et al., 2000). Shrinkage corrected volumes and surface areas was performed using correction factors $f_V = 1.931$ and $f_A = 1.551$ respectively (Amunts et al., 2005).

area	volume	corrected	μ	σ	z-score
<i>hOc1</i>	9019.30	17416.27	18042.2	2464.39	-0.25
<i>hOc2</i>	6448.60	12452.26	12634.2	2862.84	-0.06
<i>hOc3v</i>	1974.76	3813.26	n.a.	n.a.	n.a.
<i>hOc5</i>	304.10	587.21	1144.4	406.53	-1.37
area	surface	corrected	μ	σ	z-score
<i>hOc1</i>	6891.03	10685.76	12213.0	2225.55	-0.69
<i>hOc2</i>	6749.64	10466.52	10390.4	2925.37	0.03
<i>hOc3v</i>	2142.04	3321.62	n.a.	n.a.	n.a.
<i>hOc5</i>	319.79	495.89	450.2	135.92	0.34

error in the alignment of consecutive sections, making them inappropriate for stacks with only linear or no 3D reconstruction. The proposed method does not assume any prior 3D reconstruction - in fact its outputs might be used to guide image registration with landmarks.

4.2. Practical usefulness of the implemented workflow

The presented method showed good robustness against intersubject variability and different histological processing protocols. Thus it largely overcomes the need for brain or area specific parameter adjustments, which makes it well suited to be used as a self-contained tool for neuroscientists. Consequently, it was possible to implement it into a web application that provides a practical mapping workflow for end users from different disciplines. The web application is currently used by five neuroscientists in our institute for their research projects, without requiring support from a computer scientist. The interactive workflow enables efficient mapping of brain areas across full series of histological sections, en par with high throughput microscopy. Such efficiency of mapping was previously impossible in our experience. To give a concrete example, we consider that a trained expert typically needs 30–60 min to identify cytoarchitectonic borders for one cortical area on a single tissue section. Using the established GLI-based mapping approach (see Section 2.1), this would translate to an approximate effort of 150 work days (8 h per day) to map *hOc1* across the whole stack of 2461 sections. In comparison, the proposed method required annotation of only 18 sections to generate precise segmentations of the complete stack, corresponding to approximately 9 working hours. Altogether, including quality checks and computations, the presented workflow allows precise mapping of a large brain area in the order of 1–2 weeks - a task that would require almost a year of work with previously established methods.

Although the workflow provides a high degree of automation, we still recommend final inspection of results by an expert to ensure optimal quality. The interactive web application presented in Section 2.6 assists users with such quality control, by displaying predictions and allowing immediate correction of remaining errors with significantly less effort than annotating images from scratch. Of course, the typical amount of necessary manual corrections is an important indicator for the usefulness of the tool in practice. In our experience from mapping a whole range of different human brain regions, quality control and manual corrections typically take in the order of few hours per brain area, which may include several thousand sections.

Nevertheless, the need for manual supervision could be further reduced by investigating into methods for identifying prediction errors. Such methods could directly inform the user where additional annotations could help to further optimize the results, thereby realizing an active learning (Settles, 2009) scheme.

4.3. Ability to distinguish higher associative areas

In contrast to primary areas such as the primary visual cortex *hOc1*, so called higher associative areas have a less distinct cytoarchitecture, and less prominently differ from their neighbouring areas. Such observation lead Bailey and von Bonin to the conclusion that it is almost impossible to reliably distinguish such areas from each other, and to define borders between them (Bailey and von Bonin, 1951). This view is not supported any more due to the possibility to identify cytoarchitectonic borders in a reliable and reproducible way (for an overview see (Zilles and Amunts, 2010)). However, the fact that intersubject differences between identical areas of different brains may exceed cytoarchitectonic differences between two neighboring areas in one and the same brain creates challenges for modern brain mapping (Amunts et al., 1999).

Atzeni et al. (2018) also addressed automated mapping of histology. They segmented brain structures in a serial stack of human brain sections from the Allen Human Brain Atlas (Ding et al., 2016) (dataset AAHB used in our experiments). They used annotations from Ding et al. (2016) on a small set of sections at regular intervals, in order to train a probabilistic model that combines multi-atlas segmentation with a CNNs to segment the remaining sections. Compared to the present work however, their approach is restricted to brain structures that can be recognized at a resolution of 250 μm . The authors confirm in their paper that more subtle classes, in particular subdivisions of the isocortex, introduce excessive noise with their approach. The method presented here segmented both *hOc1* and *hOc2* in the same dataset with high accuracy by including more fine-grained texture features into the models, thus going clearly beyond this restriction.

4.4. Effect of the local segmentation models

Previous work on automatic cytoarchitectonic brain mapping using machine learning emphasized the importance of strategies for efficient exploitation of available training data and prior information. This includes incorporating probabilistic priors from brain atlases Spitzer et al. (2017) and self-supervised learning Spitzer et al. (2018). The key idea of the present paper is to use multiple local segmentation models, each of which focuses on a spatially restricted subset of sections in one specific brain area. In order to maximize practical benefit, we make an explicit design decision not to aim for a general classification model of multiple brain areas and brains. The benefit of such local segmentations models is confirmed by our experiments, which showed significantly improved performance of HR, LR, and MS compared to their globally trained counterparts HR (ALL), LR (ALL) and MS (ALL).

A major advantage of the local segmentation models is the ability to flexibly adjust the distance between training sections to account for regions with particularly simple or complex properties. This has been demonstrated for the challenging areas *hOc5* and *hOc3v*, where a reduction of the distance between training sections from 120 (2.4 mm) to 60 (1.2 mm) improved precision to a satisfactory level while keeping the annotation effort tractable.

Distance reduction results in major performance gains when using local segmentation models LR or MS, but only minor gains when using globally trained models LR (ALL) or MS (ALL). This suggests that local segmentation models make more efficient use of the additional training data.

In a similar fashion, larger areas or areas with distinct cytoarchitectonic features (e.g. *hOc1*) can be segmented with a coarser set of training sections, in this case reducing annotation effort.

The availability of expert annotations limits our ability to evaluate the effect of reducing distance between annotated sections. The results of our experiments for areas *hOc3v* and *hOc5* suggest, that the optimal distance between annotated sections depends on the cytoarchitectural and morphological complexity of a brain area. The proposed interactive

workflow allows users to add annotations incrementally until satisfied with the segmentation.

On the downside of local models, hyperparameter assessment (e.g. for learning rate or model architecture) is not straightforward when training multiple models on different training sets and evaluating them on individual test sets. Model performance needs to be evaluated across several areas, sections and brains, which can be computationally expensive and lead to a slow development process.

4.5. Effect of the multi-scale model architecture

Macroscopic features of the cerebral cortex (e.g. folding patterns) vary between individual brains. While the location of gyri and sulci can provide guidance for localizing brain areas, such coarse landmarks cannot generally be used to precisely predict cytoarchitectonic borders (Amunts and Zilles, 2015; Fischl et al., 2008; Im and Grant, 2019; Lebenberg et al., 2018). Consequently, established methods for identifying cytoarchitectonic areas rely on high-resolution microscopic information (Schleicher et al. (1999); Spitzer et al. (2017, 2018)). In contrast, the proposed local segmentation models are able to exploit macroscopic features for improving segmentation performance, thanks to their specialization on only a part of a specific brain area from one individual brain. This can be seen from the higher scores produced by the LR and MS architectures for local segmentations models (Table 1), and by the lack of such an effect for models trained on all sections of a brain area (HR (ALL), LR (ALL), MS (ALL)). Microscopic resolution features further contribute to the performance of the local segmentation models, as verified by a Wilcoxon signed-rank test (Wilcoxon, 1945) ($p = 0.011$) which confirms that the multi-scale approach of MS further improves the performance compared to LR. However, this is a relatively small effect compared to the improvement between HR and MS. We can therefore assume that macroscopic information is more relevant than microscopic information in the strictly local setting.

For further understanding the influence of the two scales in the model, it is helpful to compare predictions obtained when occluding (i.e. setting to zero) either the microscopic or macroscopic inputs in a MS model: Using only low-resolution inputs, the model is still able to approximately locate the area, but fails to capture the fine details. On the other hand, a model restricted to see only high-resolution inputs struggles to correctly locate the area. This confirms our assumption that the MS model mostly uses low-resolution inputs for localization and high-resolution inputs for local refinement. While the results of this experiment cover only a specific setting (e.g. model, area and input location), they give us some confidence that the model works as expected.

4.6. Failure mode analysis

The predictions produced by the proposed model typically include some remaining errors (Figs. 9, 12), which require careful interpretation.

Close to brain region boundaries, it must be noted that the GLI-based reference annotations enforce straight lines to model the border, which reflects the vertical arrangement of neurons in columns as a major principle in cortical organization (Schleicher et al., 2000; 1999). This may lead to discrepancies with the present segmentations, that do not enforce such constraints (see for example Fig. 12). In fact the location of the boundary is not determined down to the single pixel, and as a consequence, pixel-level metrics have a somewhat limited significance there.

Many of the remaining classification errors further coincide with highly oblique cutting angles of the tissue. As also reported in (Schleicher et al., 1999; Spitzer et al., 2017; 2018), identification of cortical areas is almost impossible at such angles, because the laminar composition of the cortex is then almost invisible in the 2D section. In such cases, experts would consult adjacent sections to identify areas, which the proposed method cannot do. An extension of the method

considering multiple adjacent sections for classification might be able to overcome this issue.

Whether or not remaining segmentation errors are critical in practice depends on the availability of postprocessing methods for correcting them. In the experiments that we carried out, the precise 3D reconstruction of the BigBrain dataset could be used for removing spurious errors (Section 2.8). However, if no precise 3D reconstruction is available, the manual effort for quality control of predictions and any necessary error corrections increases. For such settings, it would be beneficial to develop additional heuristics to identify errors, e.g. for detecting inter-section inconsistencies from only approximate section alignments.

5. Conclusion

A novel method based on Convolutional Neural Networks (CNNs) was introduced for automated mapping of cytoarchitectonic areas in large series of histological human brain sections. Segmentation models were trained for segmentation of different cytoarchitectonic areas in histological stacks obtained from three different brain samples. A key idea is to train separate local segmentation models based on annotations of one specific target area in only two training sections, to focus the learning process on microscopic and macroscopic tissue features close to the training sections. Local segmentation models enable exploitation of low-resolution macroscopic information and significantly improve performance over globally trained models. After training, local segmentation models were able to accurately segment sections in between their respective training sections. By concatenating results from multiple local segmentation models, segmentations for complete brain areas can be obtained. The proposed method opens up new possibilities to map complete stacks of histological human brain sections in a highly automated fashion, and thus provides an important basis for building high-resolution human brain maps for datasets like BigBrain. To the best of our knowledge, the maps of areas *hOc1*, *hOc2*, *hOc3v* and *hOc5* computed for the BigBrain model using this method are the first high-resolution 3D maps of human cytoarchitectonic areas created from full stacks of histological sections at cellular resolution. These maps enable precise studies of area-specific morphological and columnar features at microscopic resolution, and in combination with existing cortical layer maps (Wagstyl et al., 2020) an investigation into layer-specific aspects of each region. Dense maps further enable straightforward mapping from the volume to the whole brain mesh surface, which in turn facilitates comparison with other modalities, especially in-vivo imaging. They represent an important contribution for using BigBrain as a microscopic resolution reference space, since they provide direct links to probabilistic cytoarchitectonic reference parcellations at the macroscopic scale (Amunts et al., 2020) that are widely used in neuroimaging studies. As such, our work makes an important contribution to linking neuroscientific findings across spatial scales.

Ethics Statement

The study carried out requires no separate ethical approvals. Post-mortem brains were obtained in accordance to legal and ethical regulations and guidelines. Brain tissue for datasets B01 and B20 was obtained through the body donor program of the department of anatomy of the Heinrich Heine University Düsseldorf and with approval of the ethics committee of the medical faculty of the Heinrich Heine University Düsseldorf. Brain tissue for dataset AAHB was obtained from the University of Maryland Brain and Tissue Bank and with approval by the Human Investigation Committees and Institutional Ethics Committees of the University of Maryland.

Declaration of Competing Interest

The authors declare no competing interests.

Credit authorship contribution statement

Christian Schiffer: Conceptualization, Methodology, Software, Validation, Formal analysis, Investigation, Data curation, Writing - original draft, Writing - review & editing, Visualization. **Hannah Spitzer:** Conceptualization, Methodology, Software, Writing - review & editing. **Kai Kiwitz:** Data curation, Validation, Writing - review & editing. **Nina Unger:** Data curation, Validation, Writing - review & editing. **Konrad Wagstyl:** Software, Writing - review & editing. **Alan C. Evans:** Resources, Writing - review & editing, Funding acquisition. **Stefan Harmeling:** Writing - review & editing, Supervision. **Katrin Amunts:** Conceptualization, Investigation, Validation, Writing - review & editing, Supervision, Project administration, Resources, Funding acquisition. **Timo Dickscheid:** Conceptualization, Methodology, Supervision, Writing - original draft, Writing - review & editing, Project administration, Funding acquisition.

Acknowledgments

This project received funding from the European Union's Horizon 2020 Research and Innovation Programme, grant agreements 785907 (HBP SGA2) and 945539 (HBP SGA3), from the Helmholtz Association's Initiative and Networking Fund through the Helmholtz International BigBrain Analytics and Learning Laboratory (HIBALL) under the Helmholtz International Lab grant agreement InterLabs-0015, and from Priority Program 2041 (SPP 2041) "Computational Connectomics" of the German Research Foundation (DFG). This work was further supported by the German Federal Ministry of Education and Research (BMBF) and the Max Planck Society for the Advancement of Science through their joint initiative between German Universities and German Research Organizations Computing time was granted through JARA on the supercomputer JURECA at Jülich Supercomputing Centre (JSC) as part of the project CJINM16.

Supplementary material

Supplementary material associated with this article can be found, in the online version, at doi:10.1016/j.neuroimage.2021.118327.

References

- Abadi, M., Barham, P., Chen, J., Chen, Z., Davis, A., Dean, J., Devin, M., Ghemawat, S., Irving, G., Isard, M., 2016. TensorFlow: a system for large-scale machine learning. In: 12th USENIX Symposium on Operating Systems Design and Implementation OSDI 16, pp. 265–283.
- Amunts, K., Kedo, O., Kindler, M., Pieperhoff, P., Mohlberg, H., Shah, N.J., Habel, U., Schneider, F., Zilles, K., 2005. Cytoarchitectonic mapping of the human amygdala, hippocampal region and entorhinal cortex: intersubject variability and probability maps. *Anat. Embryol.* 210 (5–6), 343–352. doi:10.1007/s00429-005-0025-5.
- Amunts, K., Lepage, C., Borgeat, L., Mohlberg, H., Dickscheid, T., Rousseau, M.-É., Bludau, S., Bazin, P.-L., Lewis, L.B., Oros-Peusquens, A.-M., Shah, N.J., Lippert, T., Zilles, K., Evans, A.C., 2013. BigBrain: an ultrahigh-resolution 3D human brain model. *Science* 340 (6139), 1472–1475. doi:10.1126/science.1235381.
- Amunts, K., Malikovic, A., Mohlberg, H., Schormann, T., Zilles, K., 2000. Brodmann's areas 17 and 18 brought into stereotaxic space—where and how variable? *NeuroImage* 11 (1), 66–84. doi:10.1006/nimg.1999.0516.
- Amunts, K., Mohlberg, H., Bludau, S., Zilles, K., 2020. Jülich-Brain: a 3D probabilistic atlas of the human brain's cytoarchitecture. *Science* doi:10.1126/science.abb4588.
- Amunts, K., Schleicher, A., Bürgel, U., Mohlberg, H., Uylings, H.B.M., Zilles, K., 1999. Broca's region revisited: cytoarchitecture and intersubject variability. *J. Comp. Neurol.* 412 (2), 319–341. doi:10.1002/(SICI)1096-9861(19990920)412:2<319::AID-CNE10>3.0.CO;2-7.
- Amunts, K., Schleicher, A., Zilles, K., 2004. Outstanding language competence and cytoarchitecture in Broca's speech region. *Brain Lang.* 89 (2), 346–353. doi:10.1016/S0093-934X(03)00360-2.
- Amunts, K., Zilles, K., 2015. Architectonic mapping of the human brain beyond Brodmann. *Neuron* 88 (6), 1086–1107. doi:10.1016/j.neuron.2015.12.001.
- Anness, J., Pitiot, A., Dinov, I.D., Toga, A.W., 2004. A myelo-architectonic method for the structural classification of cortical areas. *NeuroImage* 21 (1), 15–26. doi:10.1016/j.neuroimage.2003.08.024.
- Atzeni, A., Jansen, M., Ourselin, S., Iglesias, J.E., 2018. A probabilistic model combining deep learning and multi-atlas segmentation for semi-automated labelling

- of histology. In: Frangi, A.F., Schnabel, J.A., Davatzikos, C., Alberola-López, C., Fichtinger, G. (Eds.), *Medical Image Computing and Computer Assisted Intervention – MICCAI 2018*, vol. 11071. Springer International Publishing, pp. 219–227. doi:10.1007/978-3-030-00934-2_25.
- Bailey, P., von Bonin, G., 1951. The isocortex of man. *Urbana* 3.
- Bok, S.T., 1929. Der Einfluß der in den Furchen und Windungen auftretenden Krümmungen der Großhirnrinde auf die Rindenarchitektur. *Zeitschrift für die gesamte Neurologie und Psychiatrie* 121 (1), 682. doi:10.1007/BF02864437.
- Çiçek, Ö., Abdulkadir, A., Lienkamp, S.S., Brox, T., Ronneberger, O., 2016. 3D U-Net: Learning dense volumetric segmentation from sparse annotation. In: *International Conference on Medical Image Computing and Computer-Assisted Intervention*. Springer, pp. 424–432.
- Dalcin, L.D., Paz, R.R., Kler, P.A., Cosimo, A., 2011. Parallel distributed computing using Python. *Adv. Water Resour.* 34 (9), 1124–1139. doi:10.1016/j.advwatres.2011.04.013.
- Dickscheid, T., Haas, S., Bludau, S., Glock, P., Huysegoms, M., Amunts, K., 2019. Towards 3D reconstruction of neuronal cell distributions from histological human brain sections. *Future Trends HPC Disruptive Scenario* 34, 223.
- Ding, S.-L., Boyall, J.J., Sunkin, S.M., Ng, L., Facer, B.A.C., Lesnar, P., Guillozet-Bongaarts, A., McMurray, B., Szafer, A., Dolbeare, T.A., Stevens, A., Tirrell, L., Benner, T., Caldejon, S., Dalley, R.A., Dee, N., Lau, C., Nyhus, J., Reding, M., Riley, Z.L., Sandman, D., Shen, E., van der Kouwe, A., Varjabedian, A., Write, M., Zollei, L., Dang, C., Knowles, J.A., Koch, C., Phillips, J.W., Sestan, N., Wohnot, P., Zielke, H.R., Hohmann, J.G., Jones, A.R., Bernard, A., Hawrylycz, M.J., Hof, P.R., Fischl, B., Lein, E.S., 2016. Comprehensive cellular-resolution atlas of the adult human brain. *J. Comp. Neurol.* 524 (16), 3127–3481. doi:10.1002/cne.24080.
- Fischl, B., Rajandran, N., Busa, E., Augustinack, J., Hinds, O., Yeo, B.T., Mohlberg, H., Amunts, K., Zilles, K., 2008. Cortical folding patterns and predicting cytoarchitecture. *Cereb. Cortex* 18 (8), 1973–1980.
- Goulas, A., Zilles, K., Hilgetag, C.C., 2018. Cortical gradients and laminar projections in mammals. *Trends Neurosci.* 41 (11), 775–788. doi:10.1016/j.tins.2018.06.003.
- Goyal, P., Dollár, P., Girshick, R., Noordhuis, P., Wesolowski, L., Kyrola, A., Tulloch, A., Jia, Y., He, K., 2017. Accurate, large minibatch SGD: training imagenet in 1 h. *arXiv preprint arXiv:1706.02677*.
- Im, K., Grant, P.E., 2019. Sulcal pits and patterns in developing human brains. *NeuroImage* 185, 881–890.
- Lotte, S., Szegedy, C., 2015. Batch normalization: accelerating deep network training by reducing internal covariate shift. In: *International Conference on Machine Learning*, pp. 448–456.
- Kiwitz, K., Schiffer, C., Dickscheid, T., Amunts, K., 2019. Reference delineations of area hOc1 (V1, 17, Cal5) in individual sections of the BigBrain [Data set]. *EBRAINS* doi:10.2593/3G5V-T4A.
- Kiwitz, K., Schiffer, C., Dickscheid, T., Amunts, K., 2019. Reference delineations of area hOc2 (V2, 18) in individual sections of the BigBrain [Data set]. *EBRAINS* doi:10.2593/BMKD-D77.
- Kiwitz, K., Schiffer, C., Dickscheid, T., Amunts, K., 2020. Reference delineations of area hOc3v (LingG) in individual sections of the BigBrain [Data set]. *EBRAINS* doi:10.2593/DBZG-QZ.
- Kiwitz, K., Schiffer, C., Dickscheid, T., Malikovic, A., Amunts, K., 2020. Reference delineations of area hOc5 (LOC) in individual sections of the BigBrain [Data set]. *EBRAINS* doi:10.2593/4027-K9Y.
- Krause, D., Thümg, P., 2018. JURECA: Modular supercomputer at Jülich supercomputing centre. *J. Large-Scale Res. Facil. JLSRF* 4, A132. doi:10.17815/jlsrf-4-121-1.
- Lebenberg, J., Labit, M., Auzias, G., Mohlberg, H., Fischer, C., Rivière, D., Duchesnay, E., Kabdebon, C., Leroy, F., Labra, N., Poupon, F., Dickscheid, T., Hertz-Pannier, E., Poupon, C., Dehaene-Lambertz, G., Hüppi, P.S., Amunts, K., Dubois, J., Mangin, J.-F., 2018. A framework based on sulcal constraints to align preterm, infant and adult human brain images acquired in vivo and post mortem. *Brain Struct. Funct.* 223 (9), 4153–4163. doi:10.1007/s00429-018-1735-9.
- Leprince, Y., Poupon, F., Delzescaux, T., Hasboun, D., Poupon, C., Rivière, D., 2015. Combined Laplacian-equivolumetric model for studying cortical lamination with ultra high field MRI (7 T). In: 2015 IEEE 12th International Symposium on Biomedical Imaging (ISBI), pp. 580–583. doi:10.1109/ISBI2015.7163940.
- Lewiner, T., Lopes, H., Vieira, A.W., Tavares, G., 2003. Efficient implementation of marching cubes' cases with topological guarantees. *J. Graphics Tools* 8 (2), 1–15. doi:10.1080/10867651.2003.10487582.
- Lewis, L., Lepage, C., Fournier, M., Zilles, K., Amunts, K., Evans, A.C., 2014. BigBrain: initial tissue classification and surface extraction. 20th Annual Meeting of the Organization for Human Brain Mapping (OHBM).
- Malikovic, A., Amunts, K., Schleicher, A., Mohlberg, H., Eickhoff, S.B., Wilms, M., Palomero-Gallagher, N., Armstrong, E., Zilles, K., 2007. Cytoarchitectonic analysis of the human extrastriate cortex in the region of V5/MT+: a probabilistic, stereotaxic map of area hOc5. *Cereb. Cortex* 17 (3), 562–574. doi:10.1093/cercor/bhj181.
- Merker, B., 1983. Silver staining of cell bodies by means of physical development. *J. Neurosci. Methods* 9 (3), 235–241. doi:10.1016/0165-0276(83)90086-9.
- Milietari, F., Navab, N., Ahmadi, S.A., 2016. V-Net: fully convolutional neural networks for volumetric medical image segmentation. In: 2016 Fourth International Conference on 3D Vision (3DV). IEEE, pp. 565–571.
- Omidyeganeh, M., Lepage, C., Wagstyl, K., Spitzer, H., Dickscheid, T., Amunts, K., Evans, A., 2020. Non-linear registration of 1 µm histology sections into 3D 20 µm BigBrain space. 26th Annual Meeting of the Organization for Human Brain Mapping.
- Richter, M., Amunts, K., Mohlberg, H., Bludau, S., Eickhoff, S.B., Zilles, K., Caspers, S., 2019. Cytoarchitectonic segregation of human posterior intraparietal and adjacent parieto-occipital sulcus and its relation to visuo-motor and cognitive functions. *Cereb. Cortex* 29 (3), 1305–1327. doi:10.1093/cercor/bhy245.

- Ronneberger, O., Fischer, P., Brox, T., 2015. U-Net: convolutional networks for biomedical image segmentation. In: *International Conference on Medical Image Computing and Computer-Assisted Intervention*. Springer, pp. 234–241.
- Rotschy, C., Eickhoff, S.B., Schleicher, A., Mohlberg, H., Kujovic, M., Zilles, K., Amunts, K., 2007. Ventral visual cortex in humans: cytoarchitectonic mapping of two extrastriate areas. *Hum. Brain Mapp.* 28 (10), 1045–1059. doi:10.1002/hbm.20348.
- Ruan, J., Bludau, S., Palomero-Gallagher, N., Caspers, S., Mohlberg, H., Eickhoff, S.B., Seitz, R.J., Amunts, K., 2018. Cytoarchitecture, probability maps, and functions of the human supplementary and pre-supplementary motor areas. *Brain Struct. Funct.* 223 (9), 4169–4186. doi:10.1007/s00429-018-1738-6.
- Schleicher, A., Amunts, K., Geyer, S., Kowalski, T., Schormann, T., Palomero-Gallagher, N., Zilles, K., 2000. A stereological approach to human cortical architecture: identification and delineation of cortical areas. *J. Chem. Neuroanat.* 20, 31–47. doi:10.1016/S0891-0618(00)00076-4.
- Schleicher, A., Amunts, K., Geyer, S., Morosan, P., Zilles, K., 1999. Observer-independent method for microstructural parcellation of cerebral cortex: a quantitative approach to cytoarchitectonics. *NeuroImage* 9 (1), 165–177. doi:10.1006/nimg.1998.0385.
- Schmitt, O., Böhm, M., 2002. A robust transcortical profile scanner for generating 2-D traverses in histological sections of richly curved cortical courses. *NeuroImage* 16 (4), 1103–1119. doi:10.1006/nimg.2002.1159.
- Schober, M., Axer, M., Huysegoms, M., Schubert, N., Amunts, K., Dickscheid, T., 2016. Morphing image masks for stacked histological sections using Laplace's equation. In: Tolandorff, T., Deserno, T.M., Handels, H., Meinzer, H.-P. (Eds.), *Bildverarbeitung Für Die Medizin 2016*. Springer, pp. 146–151. doi:10.1007/978-3-662-49465-3_27.
- Sergeev, A., Del Balso, M., 2018. Horovod: fast and easy distributed deep learning in TensorFlow. *arXiv preprint arXiv:1802.05799*.
- Settles, B., 2009. *Active Learning Literature Survey*. Computer Sciences Technical Report. University of Wisconsin-Madison.
- Sigl, B., 2018. *Zytoarchitektur, Netzwerke und Funktionen der Areale des menschlichen dorsolateralen prämotorischen Kortex - Komponenten motorischer Planung und Kandidat für das Frontale Augenfeld* Dissertation.
- Sigl, B., Bludau, S., Mohlberg, H., Eickhoff, S.B., Amunts, K., 2019a. Interpolated 3D map of area 6d1 (PreCG) in the BigBrain [Data set]. EBRAINS doi:10.25493/KOX6-KKB.
- Sigl, B., Bludau, S., Mohlberg, H., Eickhoff, S.B., Amunts, K., 2019b. Interpolated 3D map of area 6d2 (PreCG) in the BigBrain [Data set]. EBRAINS doi:10.25493/8WSN-JQ8.
- Sigl, B., Bludau, S., Mohlberg, H., Eickhoff, S.B., Amunts, K., 2019c. Interpolated 3D map of area 6c3 (PreCG) in the BigBrain [Data set]. EBRAINS doi:10.25493/BS7N-ZDX.
- Spitzer, H., Amunts, K., Harmeling, S., Dickscheid, T., 2017. Parcellation of visual cortex on high-resolution histological brain sections using convolutional neural networks. In: 2017 IEEE 14th International Symposium on Biomedical Imaging (ISBI 2017). IEEE, pp. 920–923. doi:10.1109/ISBI.2017.7950666.
- Spitzer, H., Kwitz, K., Amunts, K., Harmeling, S., Dickscheid, T., 2018. Improving cytoarchitectonic segmentation of human brain areas with self-supervised siamese networks. In: *Medical Image Computing and Computer Assisted Intervention – MICCAI 2018*. Springer International Publishing, pp. 663–671.
- Sutskever, I., Martens, J., Dahl, G., Hinton, G., 2013. On the importance of initialization and momentum in deep learning. In: *International Conference on Machine Learning*, pp. 1139–1147.
- Unger, N., Bladau, S., Mohlberg, H., Caspers, S., Amunts, K., 2020a. Probabilistic cytoarchitectonic map of area OP5 (Frontal Operculum) (v2.0) [Data set]. EBRAINS doi:10.25493/TWFH-BJZ.
- Unger, N., Bladau, S., Mohlberg, H., Caspers, S., Amunts, K., 2020b. Probabilistic cytoarchitectonic map of area OP6 (Frontal Operculum) (v2.0) [Data set]. EBRAINS doi:10.25493/41KE-8HT.
- Unger, N., Bladau, S., Mohlberg, H., Caspers, S., Amunts, K., 2020c. Probabilistic cytoarchitectonic map of area OP7 (Frontal Operculum) (v2.0) [Data set]. EBRAINS doi:10.25493/T2M3-2ST.
- Wagsstyl, K., Larocque, S., Cuccurull, G., Lepage, C., Cohen, J.F., Bludau, S., Palomero-Gallagher, N., Lewis, L.B., Funck, T., Spitzer, H., 2020. BigBrain 3D atlas of cortical layers: cortical and laminar thickness gradients diverge in sensory and motor cortices. *PLoS Biol.* 18 (4), e3000678.
- Wilcoxon, F., 1945. Individual comparisons by ranking methods. *Biometrics Bull.* 1 (6), 80–83. doi:10.2307/3001968.
- Wree, A., Schleicher, A., Zilles, K., 1982. Estimation of volume fractions in nervous tissue with an image analyzer. *J. Neurosci. Methods* 6 (1), 29–43. doi:10.1016/0165-0270(82)90014-0.
- Zeller, M.D., Fergus, R., 2014. Visualizing and understanding convolutional networks. In: *European Conference on Computer Vision*. Springer, pp. 818–833.
- Zilles, K., Amunts, K., 2010. Centenary of Brodmann's map—conception and fate. *Nat. Rev. Neurosci.* 11 (2), 139–145. doi:10.1038/nrn2776.

Study 2

Cytoarchitectonic maps of the human metathalamus in 3D space

Kai Kiwitz^{1,2}, Andrea Brandstetter³, Christian Schiffer^{3,4}, Sebastian Bludau³,
Hartmut Mohlberg³, Mona Omidyeganeh^{5,6}, Philippe Massicotte⁵, Katrin
Amunts^{1,2,3}

¹Cécile and Oskar Vogt Institute of Brain Research, Univ. Hospital Düsseldorf,
Heinrich-Heine University Düsseldorf, Germany

²Max Planck School of Cognition, Stephanstrasse 1a, Leipzig, Germany

³Institute of Neuroscience and Medicine (INM-1), Forschungszentrum Jülich, German

⁴Helmholtz AI, Research Centre Jülich, Germany

⁵McGill Centre for Integrative Neuroscience, McConnell Brain Imaging Center,
Montreal Neurological Institute, Canada

⁶National Research Council of Canada, Canada



Cytoarchitectonic Maps of the Human Metathalamus in 3D Space

Kai Kiwitz^{1,2*}, Andrea Brandstetter³, Christian Schiffer^{3,4}, Sebastian Bludau⁵, Hartmut Mohlberg³, Mona Omidyeganeh^{5,6}, Philippe Massicotte⁵ and Katrin Amunts^{1,2,3}

¹ Cécile and Oskar Vogt Institute of Brain Research, University Hospital Düsseldorf, Medical Faculty, Heinrich Heine University, Düsseldorf, Germany, ² Max Planck School of Cognition, Stephanstraße 1a, Leipzig, Germany, ³ Institute of Neuroscience and Medicine (INM-1), Forschungszentrum Jülich, Jülich, Germany, ⁴ Helmholtz AI, Forschungszentrum Jülich, Jülich, Germany, ⁵ McGill Centre for Integrative Neuroscience, McConnell Brain Imaging Center, Montreal Neurological Institute, McGill University, Montreal, QC, Canada, ⁶ National Research Council of Canada, Ottawa, ON, Canada

The human metathalamus plays an important role in processing visual and auditory information. Understanding its layers and subdivisions is important to gain insights in its function as a subcortical relay station and involvement in various pathologies. Yet, detailed histological references of the microanatomy in 3D space are still missing. We therefore aim at providing cytoarchitectonic maps of the medial geniculate body (MGB) and its subdivisions in the BigBrain – a high-resolution 3D-reconstructed histological model of the human brain, as well as probabilistic cytoarchitectonic maps of the MGB and lateral geniculate body (LGB). Therefore, histological sections of ten postmortem brains were studied. Three MGB subdivisions (MGBv, MGBd, MGBm) were identified on every 5th BigBrain section, and a deep-learning based tool was applied to map them on every remaining section. The maps were 3D-reconstructed to show the shape and extent of the MGB and its subdivisions with cellular precision. The LGB and MGB were additionally identified in nine other postmortem brains. Probabilistic cytoarchitectonic maps in the MNI “Colin27” and MNI ICBM152 reference spaces were computed which reveal an overall low interindividual variability in topography and extent. The probabilistic maps were included into the Julich-Brain atlas, and are freely available. They can be linked to other 3D data of human brain organization and serve as an anatomical reference for diagnostic, prognostic and therapeutic neuroimaging studies of healthy brains and patients. Furthermore, the high-resolution MGB BigBrain maps provide a basis for data integration, brain modeling and simulation to bridge the larger scale involvement of thalamocortical and local subcortical circuits.

Keywords: metathalamus, BigBrain, cytoarchitectonic maps, lateral geniculate body, medial geniculate body, human, 3D histology

OPEN ACCESS

Edited by:

Kathleen S. Rockland,
Boston University, United States

Reviewed by:

Laurent Petit,
Centre National de la Recherche
Scientifique (CNRS), France
John M. Allman,
California Institute of Technology,
United States

*Correspondence:

Kai Kiwitz
kai.kiwitz@med.uni-duesseldorf.de

Received: 16 December 2021

Accepted: 18 January 2022

Published: 08 March 2022

Citation:

Kiwitz K, Brandstetter A, Schiffer C, Bludau S, Mohlberg H, Omidyeganeh M, Massicotte P and Amunts K (2022) Cytoarchitectonic Maps of the Human Metathalamus in 3D Space. *Front. Neuroanat.* 16:837485. doi: 10.3389/fnana.2022.837485

INTRODUCTION

The human metathalamus, located caudoventrally of the main body of the thalamus, plays an important role in processing visual and auditory information. Visual and auditory processing is encoded separately in the two major nuclei of the metathalamus, i.e., the lateral geniculate body (LGB) and the medial geniculate body (MGB). The LGB is a 6-layered structure, innervated by optic tract fibers covering the contralateral visual field. Its two magnocellular and four parvocellular layers process functionally distinct retinal pathways. The MGB on the other hand receives input from ascending tonotopically organized projections *via* the medial lemniscus, as well as projections

from the inferior colliculus and the auditory cortex (Peruzzi et al., 1997; Saint Marie et al., 1997; Llano and Sherman, 2008; Caspary and Llano, 2017). It can cytoarchitectonically be subdivided into three major compartments: the ventral, dorsal and medial subdivisions (Winer, 1984). Both nuclei have prominent projections to cortical areas and serve as subcortical relay stations.

Investigating the structural-functional relationship of the MGB and LGB including its subdivisions and layers is also relevant from a clinical perspective, e.g., to understand the MGB's involvement in tinnitus (Llinas et al., 2002; Rauschecker et al., 2010; Leaver et al., 2011; Ridder et al., 2015; Caspary and Llano, 2017; Berlot et al., 2020), speech recognition (Mihai et al., 2019), and developmental dyslexia (Diaz et al., 2012) as well as the LGB's role in glaucoma (Wang et al., 2015; Stein et al., 2021), multiple sclerosis (Korsholm et al., 2007; Papadopoulou et al., 2019), Parkinson's (Lee et al., 2016), and psychiatric diseases (Butler and Javitt, 2005; Selemon and Begovic, 2007).

Since the spatial resolution of ultra-highfield fMRI has increased to the submillimeter range in recent years, more detailed studies have become feasible including the possibility to measure laminar brain activity (Huber et al., 2018; Jia et al., 2021) as well as identifying functional subdivisions of subcortical (Rijk et al., 2021) and cortical (Martino et al., 2015; Nasr et al., 2016) structures.

However, existing histological maps of the human thalamus do not include subdivisions of the MGB and/or layers of the LGB or do not cover the metathalamus over its whole extent (Morel, 2007; Krauth et al., 2010; Ding et al., 2016; Mai et al., 2016). The same holds true for MRI based probabilistic atlases of the thalamus (Iglesias et al., 2018; Najdenovska et al., 2018; García-Gomar et al., 2019). Furthermore, no probabilistic histologically based reference maps of the metathalamus exist so far, which make it difficult to account for individual variability in topography and volume, as well as to compare histological maps with findings from neuroimaging. More detailed maps of subdivisions and layers of the MGB and LGB could provide micro-anatomical reference data for high-field MRI investigations, to inform neuroimaging studies, and to provide reference data for biologically realistic brain modeling and simulation.

The BigBrain model based on its 7404 cell-body stained and 3D-reconstructed sections constitutes an anatomical brain model at a spatial resolution of 20 micrometers isotropic in this regard (Amunts et al., 2013). It has been used, for example, to interpret MRI based models of brain connectivity (Wei et al., 2019; Paquola et al., 2020b), functional and structural gradients (Paquola et al., 2019; Royer et al., 2020), as well as default mode network components (Margulies et al., 2016; Paquola et al., 2019).

In the present study, we aimed to create a cytoarchitectonic map of the MGB and its subdivisions in the BigBrain model and supplement previously published maps of the LGB with its six layers (Brandstetter et al., 2021). To construct a high-resolution map of the MGB, a novel deep-learning based cytoarchitectonic mapping tool was applied (Schiffer et al., 2021c). Secondly, the MGB and LGB were identified in histological sections of ten postmortem brains and volumes, as

well as probabilistic cytoarchitectonic maps were computed to address the intersubject variability of the two nuclei.

MATERIALS AND METHODS

Processing of Postmortem Brains

Cytoarchitectonic mapping was performed in serial histological sections of ten human brains from body donors (5 female, age 59–85 years, 5 male, 30–75 years, Table 1). The brains were obtained in accordance to legal and ethical regulations and guidelines as part of the body donor program of the Department of Anatomy of the Heinrich Heine University Düsseldorf. Body donors gave written informed consent for the general use of brain tissue for aims of research and education. All usage in this work is covered by a vote of the ethics committee of the Medical Faculty of the Heinrich Heine University Düsseldorf (#4863). The postmortem delay did not exceed 24–36 h. The list of brains also included the BigBrain dataset (Amunts et al., 2013).

The procedure of processing the brain tissue was described in detail in Amunts et al. (2020). In short, the brains were fixed in 4% buffered formalin (pH 7.4) or Bodian's fixative for at least 3 months. All brains underwent magnetic resonance imaging using a T1-weighted 3D FLASH sequence (flip angle 40°, repetition time TR 40 ms, echo time TE 5 ms). MR images were used as an undistorted spatial reference for the 3D-reconstruction of the histological sections. After scanning, the brains were embedded in paraffin and serially sectioned in the coronal plane on a large-scale microtome (20 µm thickness), whereby series of blockface images of the paraffin-embedded brains were obtained. Every 15th section (every section in case of the BigBrain) was stained for cell bodies using a silver staining technique (Merker, 1983), and digitized using tissue scanners (1 µm in-plane resolution).

Cytoarchitectonic Probability Maps

To create probability maps of the MGB and LGB, both nuclei were delineated and traced over their whole extent on every 15th section (distance between sections: 300 µm) in all 10

TABLE 1 | List of postmortem brains used for cytoarchitectonic mapping and analysis.

Brain ID	Gender	Age (Years)	Cause of death	Fresh weight (g)
pm 1	Female	79	Carcinoma of the bladder	1,350
pm 4	Male	75	Necrotizing glomerulonephritis	1,349
pm 5	Female	59	Cardiorespiratory insufficiency	1,142
pm 7	Male	37	Acute right heart failure/cardiac arrest	1,437
pm 8	Female	72	Renal failure/renal arrest	1,216
pm 9	Female	79	Cardiorespiratory insufficiency	1,110
pm 10	Female	85	Mesenteric infarction	1,046
pm 13	Male	39	Drowning	1,234
pm 20	Male	65	Cardiorespiratory insufficiency	1,392
pm 21	Male	30	Bronchopneumonia	1,409

brains using an in-house software (Online Section Tracer). The MGB was identified based on previous microscopical studies and its characteristic topography (Kuhlenbeck, 1954; Winer, 1984). Delineation criteria for the LGB were adapted from the literature (Clark, 1932; Brandstetter et al., 2021). The delineations of the MGB and LGB in the left and the right hemisphere were 3D-reconstructed. Hereby, spatial transformations of the whole-brain histological datasets were used that were earlier computed based on the MR-images and the blockface images of the paraffin-embedded brains. The delineated nuclei were then spatially normalized and transferred to the T1-weighted single-subject template of the Montreal Neurological Institute (MNI), “Colin27”, as well as the MNI ICBM152 2009c non-linear asymmetric reference space (Evans et al., 2012). The individual maps of the MGB and the LGB were superimposed in both templates to calculate probabilistic maps. Values from 0 to 100% overlap were calculated to indicate the probability for each voxel of the reference brain to contain either the MGB or the LGB at a certain position (Amunts et al., 2020).

Volumetric Analysis

Volumes were calculated and corrected for shrinkage based on the delineations of the MGB and LGB in histological sections based on Cavalieri's principle (Amunts et al., 2007). A volume normalization was applied by calculating the proportion of the volume of the structures and the total brain volume to make the results comparable (Bludau et al., 2014). Differences in volume proportions were tested for significant effects caused by hemisphere (left vs. right) and sex (male vs. female) with pairwise permutation tests. For each of these tests, the corresponding values (male/female; left/right hemisphere) were grouped and a contrast estimate was calculated between the means of these groups. The null distribution was estimated by a Monte-Carlo simulation. All values were randomly redistributed into two groups, calculating the same contrast with a repetition of 1,000,000 iterations. Differences were considered statistically significant if the contrast estimate of the true comparison was larger than 95% of the values under the null distribution ($p < 0.05$). Differences in mean volumes between the MGB and LGB were analyzed using a paired two-sided *t*-test with an α error-rate set to 0.05.

High-Resolution Cytoarchitectonic Brain Mapping in the BigBrain

In addition, the MGB and its subdivisions were delineated on every 5th section of the BigBrain dataset (Amunts et al., 2013) using the high-resolution digitized scans. The range of sections covered a distance of 3.20 mm in the left and 3.08 mm in the right hemisphere. To map the three subdivisions on every section, a deep-learning based brain mapping tool designed to map cytoarchitectonic structures in full stacks (Schiffer et al., 2021c) was applied. The deep-learning network architecture has shown to resemble cytoarchitectonic criteria (Kiwitz et al., 2020) and has successfully been used to generate whole-stack maps of several cytoarchitectonic areas (Schiffer et al., 2021c). The method was trained on 57 delineated sections containing the

MGB and its subdivisions. Training was performed remotely *via* a web-based interface (Schiffer et al., 2021c) on the supercomputer JURECA at Jülich Supercomputing Centre (Krause and Thörnig, 2018). Automatically created maps were subsequently controlled to exclude falsely qualified sections, which were manually corrected *via* the tool's web-based interface. The annotations were transformed into the 3D-reconstructed BigBrain space by applying a non-linear registration of the high-resolution digitized sections (Omidyeganeh et al., 2020) and available transformations for the BigBrain (Amunts et al., 2013) to generate a volume for each MGB subdivision. The total number of volume voxels, their physical size and a shrinkage factor of 1.931 for the BigBrain (Bludau et al., 2014) were subsequently used to calculate the volume of the MGB and its subdivisions. The total volume of the subdivisions of this straight-forward approach was compared to the estimated MGB volume based on Cavalieri's principle as described above.

3D-surface meshes of the subdivisions were generated using the marching cube algorithm (Lewiner et al., 2003). The 3D reconstruction directly followed the protocol described in Schiffer et al. (2021c). Rough edges on the mesh surfaces were subsequently smoothed locally using normalized curvature operators in the normal direction preserving their specific structure. Surface meshes of the LGB have been generated and 3D-reconstructed in a similar manner based on publicly available whole brain maps of the LGB and its layers in the BigBrain (Brandstetter et al., 2021; Schiffer et al., 2021a).

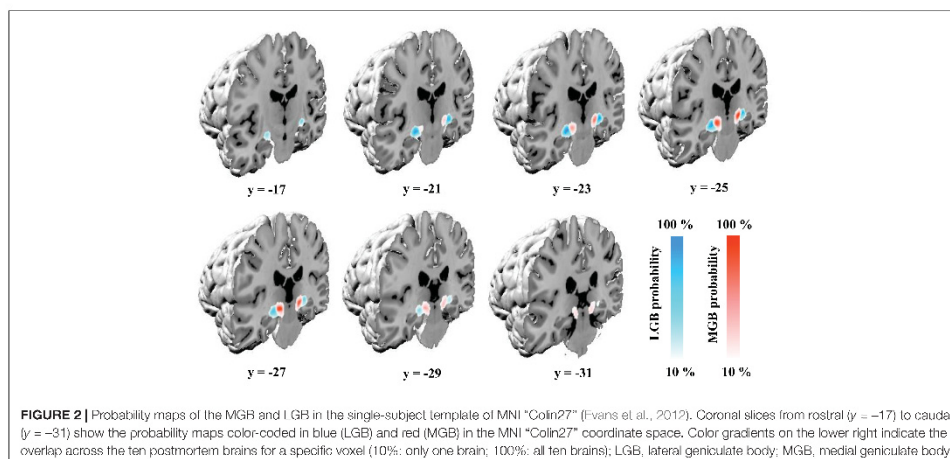
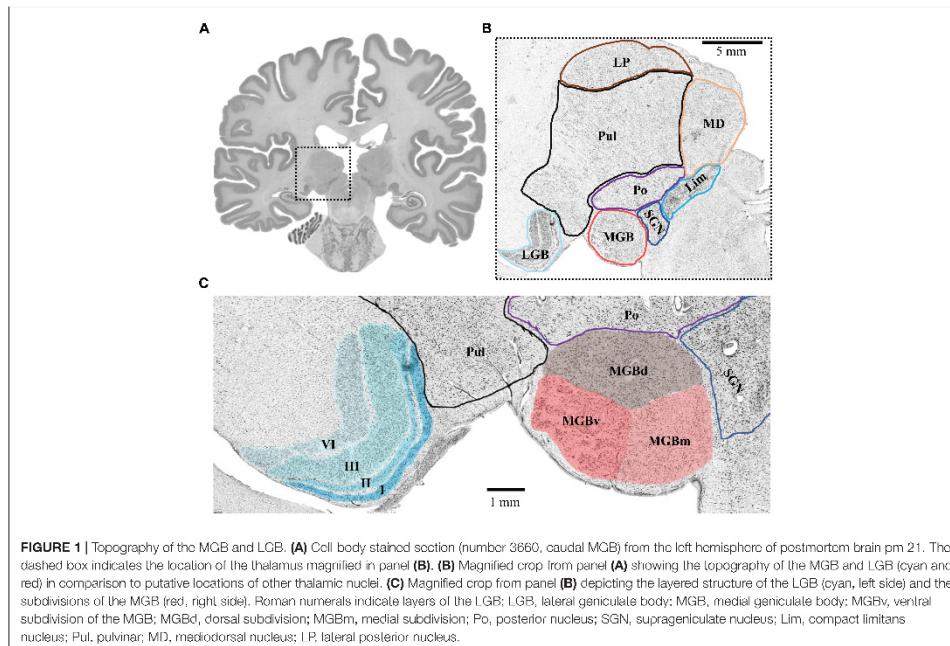
RESULTS

Localization of the Medial and Lateral Geniculate Bodies

The MGB and LGB followed a consistent topography in all analyzed postmortem brains. The LGB was located ventrolaterally of the pulvinar of the thalamus. It showed the typical 6-layered pattern with sharp bends. The MGB was always located medially to the LGB. Its caudal pole protruded from the caudal extremity of the diencephalon. The caudal pole itself was located caudoventrally of the posterior nuclear complex (i.e., the compact limitans, supragenulate and posterior nucleus of the thalamus) and medially of the inferior pulvinar nucleus of the thalamus (Figure 1). The caudal surface of the pretectum formed the dorsomedial flank of the MGB.

Probabilistic Cytoarchitectonic Maps of the Medial and Lateral Geniculate Bodies

Delineations of the MGB and LGB in the sample of 10 postmortem brains were transferred to the MNI Colin 27 and MNI ICBM152 2009c non-linear asymmetric reference spaces. The probability maps of the two nuclei show their paired arrangement caudoventrally of the main body of the thalamus. The LGB is located dorsally of the hippocampal formation along its whole extent with the MGB adjoining it medially (Figure 2). Center of mass coordinates in the Colin 27 and MNI ICBM152 2009c non-linear asymmetric spaces (in parentheses) constituted



$x = -24, y = -24, z = -10$ ($-24, -25, -9$) for the left LGB,
 $x = 22, y = -24, z = -10$ ($23, -24, -9$) for the right LGB,
 $x = -16, y = -27, z = -8$ ($-15, -27, -7$) for the left MGB, as

well as $x = 14, y = -27, z = -9$ ($15, -26, -8$) for the right MGB.
 The y -coordinates of the center of masses demonstrate the more rostral location of the LGB ($y = -24$) in comparison to the MGB

TABLE 2 | Mean volumes, standard deviations (SD) as well as minimal and maximal values of the shrinkage-corrected mean volumes of the MGB and LGB in ten postmortem brains for both hemispheres measured in mm³.

Nucleus	Statistic	Left hemisphere	Right hemisphere	Sum
MGB	Mean	124.3	134.4	258.7
	Min	91.9	89.0	
	Max	164.2	209.3	
	SD	27.4	35.3	59.2
LGB	Mean	166.9	165.5	332.4
	Min	116.3	120.4	
	Max	220.8	218.3	
	SD	28.5	26.6	54.6

MGB, medial geniculate body; LGB, lateral geniculate body.

($y = -27$) as shown in **Figure 2**. The color-coded probability maps of both nuclei (**Figure 2**) show a central peak with a steady decrease when moving away from the center of mass in all three dimensions – emphasizing the central location of the two nuclei within the probability maps in both hemispheres.

Volumetric Analysis of the Metathalamus

Results of the volumetric analysis of the ten postmortem brains are shown in **Table 2**. Shrinkage-corrected mean volumes of the MGB (Mean = 258.7 mm³, SD = 59.2 mm³) were significantly smaller than the LGB (Mean = 332.4 mm³, SD = 54.6 mm³) volumes ($t(9) = -7.0$, $p < 0.001$, two-sided test). Permutation tests did not reveal any significant effects of hemisphere and sex as well as their interaction on the shrinkage-corrected volumes for each nucleus ($p > 0.05$).

Cytoarchitecture of the Medial Geniculate Body

Three subdivisions of the MGB were identified and delineated in the BigBrain (**Figure 3**): The ventral subdivision (MGBv) formed the ventrolateral part of the MGB and was mainly comprised of small and medium sized perikarya, some of which formed row-like clusters as described previously (Winer, 1984). These contributed to a layer-like appearance of the ventral subdivision (**Figure 3B**). The MGBv was flanked by white matter that extended ventrally to the lateral border of the cerebral peduncle and ringed the free surface of the caudal pole of the MGB (**Figure 3G**). It could easily be separated from the medial and dorsal subdivisions by cell-sparse zones (**Figure 3H**), as well as differences in cell-density, size and composition. Similar to observations by Winer (1984), we found a small cluster of larger cells in the ventrolateral part of the ventral subdivision on some sections (**Figure 3E**).

The dorsal subdivision (MGBd) covered the whole caudo-rostral extent of the MGB forming a cap on top of the ventral and medial subdivisions. It showed a reduced cell-density in comparison to the ventral subdivision (**Figure 3C**). The largest cells in the dorsal subdivision could be found on the medial and ventromedial limb, right at the border to the medial subdivision (**Figure 3F**). They marked the border to the medial subdivision. The border to the medial subdivision was also characterized

by a fine cell-sparse zone, which was more profound in rostral sections (**Figure 3F**).

The medial subdivision (MGBm) formed the ventromedial part of the MGB and, on average, contained the largest perikarya of all subdivisions (**Figure 3D**). The MGBm showed a caudo-rostral gradient of increasing cell size which facilitated the separation from the ventral subdivision in rostral sections. At the same time, the increase in cell size impeded the separation from the dorsal subdivision with its especially large somata at the border to the medial subdivision (**Figure 3F**).

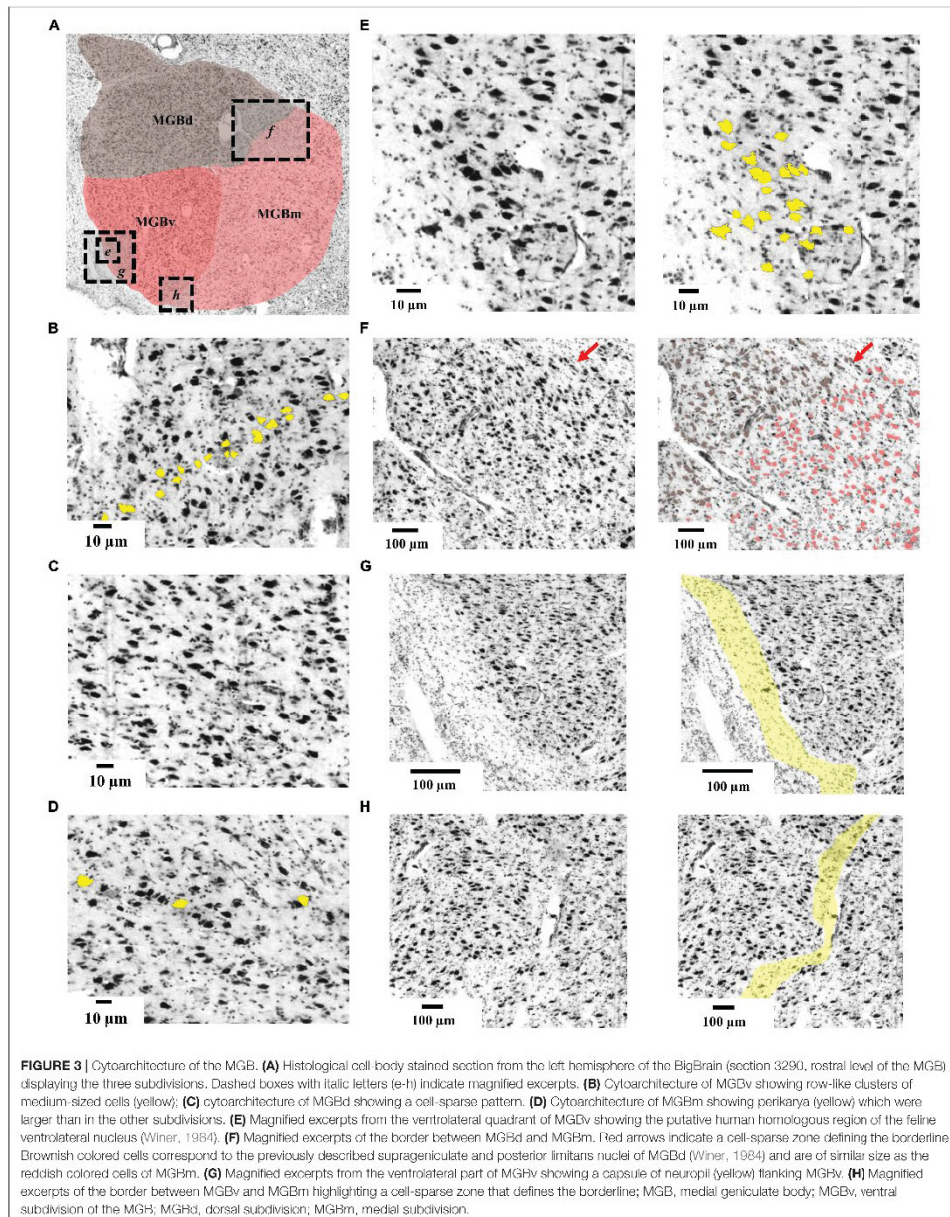
High-Resolution 3D-Reconstructions of the Medial Geniculate Body in the BigBrain

The deep-learning based brain mapping tool allowed to identify delineations of the three subdivisions of the MGB on 132 sections of the left and 165 sections of the right hemisphere in the BigBrain. Combined 3D-reconstructions of the MGB and LGB (Brandstetter et al., 2021) with its subdivisions and layers in the BigBrain are shown in **Figure 4** (see **Supplementary Video**) and demonstrate the paired arrangement of the two nuclei in proximity of the hippocampal formation ventrolaterally (**Figure 4C**). The MGBd forms a cap across the whole extent of the MGB. The ventral and medial subdivisions share the lower half of the MGB. On rostral sections, MGBd and MGBm are flanked by white matter and parts of the ventrobasal complex of the thalamus (**Figure 4C**). Here, the darkly stained substantia nigra of the mesencephalon can be seen ventromedially of the MGB (**Figure 4C**). Caudally, the MGBd and MGBm border the posterior nuclear complex along their dorsomedial surface, whereas the MGBd and MGBv border the most caudal tip of the inferior pulvinar nucleus (see **Figures 1B, C** for an illustration).

Shrinkage-corrected volumes of MGBv and MGBm were larger in the left hemisphere, whereas the MGBd subdivision showed a similar size in both hemispheres (**Table 3**). The sum of all three subdivisional volume measurements corresponds to the mean MGB volume calculated based on mappings on every 15th section in postmortem brain pm20 (BigBrain). The latter fits within 0.8 standard deviations of the left and 1.3 standard deviations of the right hemisphere of the mean volume measurements based on all ten postmortem brains (**Table 2**).

DISCUSSION

The present study introduces high-resolution 3D brain maps of the human MGB and its subdivisions in the BigBrain utilizing a novel deep-learning based brain mapping tool. Together with the recently published LGB layer maps (Brandstetter et al., 2021) they provide a high-resolution whole-brain histological reference of the metathalamus at 20 micrometer resolution. Additionally, probabilistic cytoarchitectonic maps of the MGB and LGB were calculated in a sample of ten brains, with a spatial resolution of 1 mm. They have been aligned with two commonly used reference spaces (MNI “Colin27” and MNI ICBM152 2009c non-linear asymmetric) and are part the Julich-Brain atlas (Amunts et al., 2020). All datasets are publicly available on



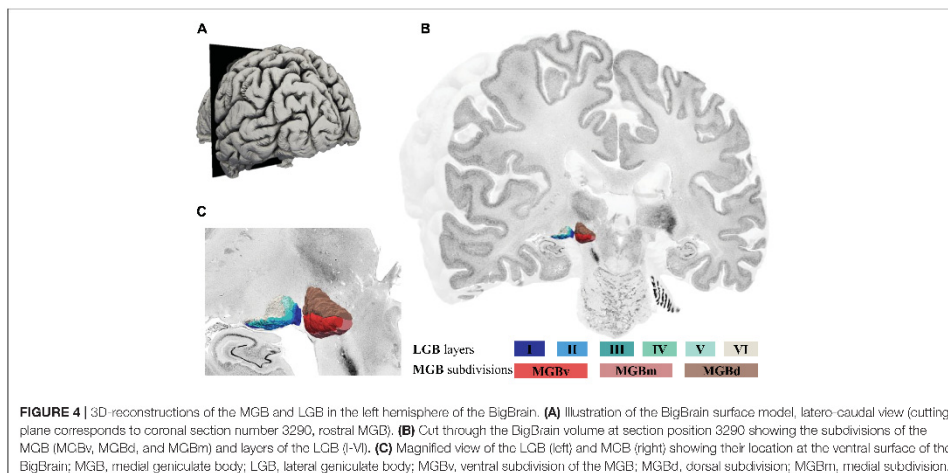


FIGURE 4 | 3D reconstructions of the MGB and LGB in the left hemisphere of the BigBrain. **(A)** Illustration of the BigBrain surface model, latero-caudal view (cutting plane corresponds to coronal section number 3290, rostral MGB). **(B)** Cut through the BigBrain volume at section position 3290 showing the subdivisions of the MGB (MGBv, MGBd, and MGBm) and layers of the LGB (I-VI). **(C)** Magnified view of the LGB (left) and MGB (right) showing their location at the ventral surface of the BigBrain; MGB, medial geniculate body; LGB, lateral geniculate body; MGBv, ventral subdivision of the MGB; MGBd, dorsal subdivision; MGBm, medial subdivision.

TABLE 3 | Volumes of the MGB subdivisions in the BigBrain for both hemispheres.

MGB subdivision	Volume in mm ³	
	Left hemisphere	Right hemisphere
MGBv	18.7	13.1
MGBd	44.8	45.3
MGBm	39.6	31.6
Sum of subdivisions	103.1	90.0

Measurements show shrinkage-corrected volumes obtained from the 3D-reconstructed surface meshes of the MGB subdivisions (MGBv, MGBd, and MGBm); MGB, medial geniculate body; MGBv, ventral subdivision of the MGB; MGBd, dorsal subdivision; MGBm, medial subdivision.

EBRAINS (Kiwitz et al., 2021b; Schiffer et al., 2021b) and the multi-level atlas of the Human Brain Project.¹

Comparison With Previous Histological Studies and Atlases

The overall characterization of three distinct subdivisions of the MGB in the BigBrain is in accordance to histological studies in human (Hassler, 1959; Winer, 1984; Morel, 2007; Ding et al., 2016; Mai et al., 2016) and animal brains (Morest, 1964; Clerici and Coleman, 1990). The topography of the three MGB subdivisions in the BigBrain resembles that shown by Morel (2007), Hassler (1959), and Winer (1992). Following their localization of the subdivisions, our analysis consolidates the notion for the ventromedial location of the magnocellular subdivision MGBm. This subdivision has previously also been reported to be located more ventrolateral by Amunts et al. (2012). The cytoarchitectonic features in our investigation correspond

¹<https://interactive-viewer.apps.hbp.eu/>

well with those found by Winer (1984), with the exception of the described size of perikarya in MGBm. In the BigBrain, MGBm still contains the largest perikarya of all subdivisions, yet the size difference seems to be not as distinct as previously described (Winer, 1984). Although we were able to detect some correspondences to even finer subparcellations, i.e., the suprageniculate and posterior limitans nuclei of the dorsal subdivision (Figure 3F) and a cell cluster possibly corresponding to the feline ventrolateral nucleus (Strick and Sterling, 1974; Winer, 1984), further subdivisions found in human (Winer, 1984) and animal studies (Morest, 1964; Harrison and Howe, 1974) could not reliably be replicated in the BigBrain.

Intersubject Variability of Volumes

Currently available histological atlases mostly contain metathalamic structures based on single brains (Ding et al., 2016) with the exception of Morel (2007), who compared the topography of structures to a previously published atlas using a different postmortem brain. The present analysis addresses intersubject variability in a larger sample. The here provided shrinkage-corrected mean volumes of the MGB add to the limited literature of histological volume measurements (Glendenning and Masterton, 1998; Rademacher et al., 2002; Sitek et al., 2019). The interindividual variability in MGB volume resembles data of a more than twofold variability reported earlier (Rademacher et al., 2002). The same is true for the LGB volumes and their approximately twofold interindividual variation (Zvorykin, 1980; Andrews et al., 1997). Similar to previous histological investigations, we found no significant hemispheric asymmetries of MGB and LGB volumes (Eidelberg and Galaburda, 1982; Andrews et al., 1997; Rademacher et al., 2002).

At the same time, volume measurements derived from MRI-based measurements differ to a varying degree from our histological volumes. Comparable MGB volumes have been reported using postmortem MRI (Sitek et al., 2019) and structural *in vivo* MRI (Kitajima et al., 2015; Amaral et al., 2016). At the same time higher MGB, as well as higher and lower LGB volumes have been reported using functional and structural *in vivo* MR measurements (Li et al., 2012; García-Gomar et al., 2019; Jonak et al., 2020).

These inconsistencies may reflect the inherent difficulty of manually segmenting small subcortical nuclei in MR-images. A direct localization of the LGB in structural MR images under low field strengths (1.5 Tesla) requires prior enhancement and co-registration to anatomical surroundings (Li et al., 2012). At 3 Tesla, the LGB has been delineated indirectly using prior masking (Wang et al., 2015; Cecchetti et al., 2016). A more direct segmentation of the LGB and MGB using structural and diffusion-weighted imaging becomes feasible at higher (7 Tesla) field strengths (García-Gomar et al., 2019). Although the MGB becomes detectable at such field strengths, a clear segmentation has only been reported for postmortem structural MR (Sitek et al., 2019). Yet, even under high field strengths a histological validation still seems to be needed to rule out possible confounds such as low diffusion anisotropy due to crossing fibers, as well as to assist investigators with anatomical landmark information when creating segmentations (García-Gomar et al., 2019). The task difficulty of perceiving the LGB and MGB in MR images is significantly impacted by the image acquisition procedure (Kitajima et al., 2015) – imposing a threat to the objectivity of such segmentations. Therefore, *in vivo* segmentations of metathalamic nuclei in particular for the MGB remains challenging due to the nuclei's small size and low contrast – confirming the notion for a more precise histologically derived reference that our probability maps provide.

The new maps constitute a probabilistic representation of the MGB and LGB in the general population and include five female and five male donors with a wide age range including brains from older body donors. The older age of some body donors may raise the question of possible structural changes of the MGB in the context of age-related hearing loss. Several studies indicate age-related changes of the subcortical auditory system with regards to neurotransmitter and calcium-binding protein expression (reviewed in Caspary and Llano, 2019). Both for normal aging and pathological conditions such as deafness, structural changes have been reported for the temporal cortex including the primary auditory cortex (Lin et al., 2014; Wong et al., 2014; Qian et al., 2017), but not for the MGB (Stanton and Harrison, 2000; Butler and Lomber, 2013; Caspary and Llano, 2019). Other pathologies like Alzheimer's disease and Leber's hereditary disease have shown to alter human MGB volumes (Jonak et al., 2020; Bernstein et al., 2021). The clinical records of the body donors did not include any information of such pathologies, and did not mention any changes in hearing abilities. Therefore, the here presented volumes seem to represent mean volumes of the investigated age range.

Neuroscientific and Clinical Relevance

The maps are part of the Julich-Brain (Amunts et al., 2020), an atlas that is part of the multilevel atlas of the Human Brain Project and its research infrastructure EBRAINS.² This way, the maps may provide a reference to localize findings from neuroimaging and serve as seed regions for functional connectivity and diffusion weighted imaging analyses. In this regard, they can be used to study brain disorders and functional impairments, including the LGB's involvement in visual field and eye movement deficits (Dai et al., 2011; Pasu et al., 2015; Usrey and Alitto, 2015; Wang et al., 2015), multiple sclerosis (Sepulcre et al., 2009; Hickman et al., 2014; Papadopoulou et al., 2019), Parkinson's disease (Lee et al., 2016), psychiatric disorders (Mai et al., 1993; Selemon and Begovic, 2007; Dorph-Petersen et al., 2009), as well as the MGB's involvement in tinnitus (Llinas et al., 2002; Rauschecker et al., 2010; Leaver et al., 2011; Ridder et al., 2015; Caspary and Llano, 2017; Berlot et al., 2020), and both structures' involvement in Leber's hereditary optic neuropathy (Jonak et al., 2020). In tinnitus patients, the maps have the potential to aid future neurosurgical planning for deep-brain stimulation (Smit et al., 2016; van Zwieten et al., 2021). The latter already benefits from the development of multimodal deep-brain stimulation atlases (Ewert et al., 2018) to which our metathalamic probability maps can contribute.

The high-resolution MGB BigBrain maps show the topography of the three subdivisions at nearly cellular resolution, and are interoperable with any reference space used in the neuroimaging community. This way, they can be used to bridge the microscale histology of the metathalamic BigBrain maps with macroscale functional measurements. Evidence from ultrahigh-field-fMRI studies for example shows a mirror-symmetric tonotopic gradient in the ventral MGB (Moerel et al., 2015), which is well reflected by the row-like cell clusters (Winer, 1984; Moerel et al., 2015) that were also detected in the BigBrain (Figure 3B). At the same time, the MGB and its ascending and descending connections seem to be involved in a tinnitus-related network (Rauschecker et al., 2010; Leaver et al., 2011; Caspary and Llano, 2017). Modulation of the ventral MGB is also behaviorally relevant for speech recognition (Mihai et al., 2019) explaining the MGB's involvement in developmental dyslexia (Díaz et al., 2012). The MGB BigBrain maps may facilitate studies of these larger scale involvements of thalamocortical circuits and local subcortical circuits.

Together with the already published LGB BigBrain maps (Brandstetter et al., 2021), the MGB maps provide a subcortical target space for neuroimaging data integration and comparative histological approaches at the level of specific subdivisions and layers of the metathalamus. Several studies have already used the 20-micron isotropic resolution of the BigBrain dataset for such integrative approaches (Paquola et al., 2020a; Royer et al., 2020) including subcortical structures of the auditory system (Sitek et al., 2019). The BigBrainWarp toolbox (Paquola et al., 2021, preprint) and the EBRAINS VoluBA toolbox for spatial anchoring in the BigBrain space³ enable such an integration.

²<https://ebrains.eu/>

³<https://ebrains.eu/service/voluba/>

Such a relationship is not only relevant to support MR measurements with the cellular architecture, but also to develop better and more realistic human brain models. The incorporation of cytoarchitectonic parameters has recently led to more biologically valid models of the macaque visual system including cortical areas of different architectural types (Schmidt et al., 2018), as well as models of the human cerebellar granular layer (Florimbi et al., 2021). However, such models usually lack quantitative metathalamic input parameters, forcing them to be estimated indirectly based on other network parameters (Schmidt et al., 2018). Following this line of arguments, the metathalamic maps in the BigBrain can enrich current brain modeling approaches by directly extracting cytoarchitectonic features from the BigBrain (Paquola et al., 2020a; Dickscheid, 2021) at the cellular level (Dickscheid et al., 2019; Behuet et al., 2021). Recent advances in reconstructing the white matter fiber architecture from Nissl-stained glia cells (Schurr and Mezer, 2021) could allow to complement such features with sample specific connectivity data of layers and subdivisions of the metathalamus.

As the BigBrain dataset is continuously expanded by cortical and subcortical cytoarchitectonic parcellations, as well as intracortical surface models (DeKraker et al., 2020; Paquola et al., 2020a; Wagstyl et al., 2020), it provides an increasingly rich resource for such integrative approaches. The here provided high-resolution maps of the MGB contribute to this development.

DATA AVAILABILITY STATEMENT

The probability maps of the MGB and LGB (Kiwitz et al., 2021a,b) and the MGB BigBrain maps along with the respective reference delineations (Kiwitz et al., 2021c; Schiffer et al., 2021b) are available on EBRAINS: <https://ebrains.eu/>.

ETHICS STATEMENT

The studies involving human brain tissue from body donors were reviewed and approved by Ethics Committee of the Medical Faculty of the Heinrich Heine University Düsseldorf. The body donors provided written informed consent for the general use of their brain tissue for aims of research and education.

AUTHOR CONTRIBUTIONS

KK developed the concept for the manuscript, conducted the cytoarchitectonic brain mapping, validated the quality of the maps and wrote the manuscript. CS designed and implemented the deep-learning based brain mapping tool and

created automatic mappings. AB validated the quality of the results of the MGB maps in the BigBrain and contributed LGB specific parts of the manuscript. SB conducted the comparative volumetric analysis of the ten postmortem brains and provided methodological advice. HM provided the calculations for image registration in the BigBrain dataset, calculated the probabilistic maps and integrated them into the Jülich-Brain. PM and MO provided critical advice on 3D-visualizations and calculated smoothed volume meshes for the BigBrain maps. KA developed the concept of the study, coordinated the research, and provided neuroanatomical expertise. All authors contributed to the article and approved the submitted version.

FUNDING

The authors are supported by the European Union's Horizon 2020 Research and Innovation Program under Grant Agreement 945539 (Human Brain Project SGA3) and by the Helmholtz Association's Initiative and Networking Fund through the Helmholtz International BigBrain Analytics and Learning Laboratory (HIBALL) under the Helmholtz International Lab grant agreement InterLabs-0015. This work was further supported by the German Federal Ministry of Education and Research (BMBF) and the Max Planck Society for the Advancement of Science through their joint initiative between German Universities and German Research Organizations. Computing time was granted through JARA-HPC on the supercomputer JURECA at Jülich Supercomputing Centre (JSC). The work received further support by the Joint LAB "Supercomputing and Modeling for the Human Brain" at Forschungszentrum Jülich.

ACKNOWLEDGMENTS

We would like to thank Casey Paquola, Kimberley Lothmann, Ariane Bruno and Marten Hein for providing valuable feedback on figure design and reviewing the manuscript.

SUPPLEMENTARY MATERIAL

The Supplementary Material for this article can be found online at: <https://www.frontiersin.org/articles/10.3389/fnana.2022.837485/full#supplementary-material>

Supplementary Video 1 | Zoom into the BigBrain model, left hemisphere, latero-caudal view (cutting plane corresponds to coronal section number 3290, rostral MGB). Subdivisions of the MGB are shown on the right, layers of the LGB are shown on the left.

REFERENCES

- Amaral, L., Ganho Ávila, A., Osório, A., Soares, M. J., He, D., Chen, Q., et al. (2016). Hemispheric asymmetries in subcortical visual and auditory relay structures in congenital deafness. *Eur. J. Neurosci.* 44, 2334–2339. doi: 10.1111/ejn.13340
- Amunts, K., Armstrong, E., Malikovic, A., Hömke, L., Mohlberg, H., Schleicher, A., et al. (2007). Gender-specific left-right asymmetries in human visual cortex. *J. Neurosci.* 27, 1356–1364. doi: 10.1523/JNEUROSCI.4753-06.2007
- Amunts, K., Lepage, C., Borgeat, L., Mohlberg, H., Dickscheid, T., Rousseau, M.-É., et al. (2013). BigBrain: an ultrahigh-resolution 3D human brain model. *Science* 340, 1472–1475. doi: 10.1126/science.1235381

- Amunts, K., Mohlberg, H., Bludau, S., and Zilles, K. (2020). Julich-brain: a 3D probabilistic atlas of the human brain's cytoarchitecture. *Science* 369, 988–992. doi: 10.1126/science.abb4588
- Amunts, K., Morosan, P., Hilbig, H., and Zilles, K. (2012). "Auditory system," in *The Human Nervous System*, eds J. K. Mai and G. Paxinos (Amsterdam: Elsevier Academic Press).
- Andrews, T. J., Halpern, S. D., and Purves, D. (1997). Correlated size variations in human visual cortex, lateral geniculate nucleus, and optic tract. *J. Neurosci.* 17, 2859–2868. doi: 10.1523/JNEUROSCI.17-08-02859.1997
- Behuet, S., Bludau, S., Kedo, O., Schiffer, C., Dickscheid, T., Brandstetter, A., et al. (2021). "A high-resolution model of the human entorhinal cortex in the 'BigBrain' – use case for machine learning and 3D analyses," in *Brain-Inspired Computing*, eds K. Amunts, L. Grandinetti, T. Lippert, and N. Petkov (Cham: Springer International Publishing), 3–21.
- Berlot, E., Arts, R., Smit, J., George, E., Gulban, O. F., Moerel, M., et al. (2020). A 7 Tesla fMRI investigation of human tinnitus percept in cortical and subcortical auditory areas. *NeuroImage Clin.* 25, 102166. doi: 10.1016/j.nicl.2020.102166
- Bernstein, A. S., Rapcsak, S. Z., Hornberger, M., and Saranathan, M. (2021). Structural changes in thalamic nuclei across prodromal and clinical Alzheimer's disease. *J. Alzheimers Dis.* 82, 361–371. doi: 10.3233/JAD-201583
- Bludau, S., Eickhoff, S. B., Mohlberg, H., Caspers, S., Laird, A. R., Fox, P. T., et al. (2014). Cytoarchitecture, probability maps and functions of the human frontal pole. *NeuroImage* 93(Pt 2), 260–275. doi: 10.1016/j.neuroimage.2013.05.052
- Brandstetter, A., Bolakhrif, N., Schiffer, C., Dickscheid, T., Mohlberg, H., and Amunts, K. (2021). "Deep learning-supported cytoarchitectonic mapping of the human lateral geniculate body in the BigBrain," in *Brain-Inspired Computing*, eds K. Amunts, L. Grandinetti, T. Lippert, and N. Petkov (Cham: Springer International Publishing), 22–32.
- Butler, B. E., and Lomber, S. G. (2013). Functional and structural changes throughout the auditory system following congenital and early-onset deafness: implications for hearing restoration. *Front. Syst. Neurosci.* 7, 92. doi: 10.3389/fnys.2013.00092
- Butler, P. D., and Javitt, D. C. (2005). Early-stage visual processing deficits in schizophrenia. *Curr. Opin. Psychiatry* 18, 151–157. doi: 10.1097/00001504-200503000-00008
- Caspary, D. M., and Llano, D. A. (2017). Auditory thalamic circuits and GABA_A receptor function: Putative mechanisms in tinnitus pathology. *Hear. Res.* 349, 197–207. doi: 10.1016/j.heares.2016.08.009
- Caspary, D. M., and Llano, D. A. (2019). "Aging processes in the subcortical auditory system," in *The Oxford Handbook of the Auditory Brainstem*, eds K. Kandler, D. M. Caspary, and D. A. Llano (Oxford: Oxford University Press), 638–680.
- Cecchetti, L., Ricciardi, E., Handjaras, G., Kupers, R., Ptito, M., and Pietrini, P. (2016). Congenital blindness affects diencephalic but not mesencephalic structures in the human brain. *Brain Struct. Funct.* 221, 1465–1480. doi: 10.1007/s00429-014-0984-5
- Clark, W. E. (1932). A morphological study of the lateral geniculate body. *Br. J. Ophthalmol.* 16, 264–284. doi: 10.1136/bjo.16.5.264
- Clerici, W. J., and Coleman, J. R. (1990). Anatomy of the rat medial geniculate body: I. Cytoarchitecture, myeloarchitecture, and neocortical connectivity. *J. Comp. Neurol.* 297, 14–31. doi: 10.1002/cne.902970103
- Dai, H., Mu, K. T., Qi, J. P., Wang, C. Y., Zhu, W. Z., Xia, L. M., et al. (2011). Assessment of lateral geniculate nucleus atrophy with 3T MR imaging and correlation with clinical stage of glaucoma. *Am. J. Neuroradiol.* 32, 1347–1353. doi: 10.3174/ajnr.A2486
- DeKraker, J., Lau, J. C., Ferko, K. M., Khan, A. R., and Köhler, S. (2020). Hippocampal subfields revealed through unfolding and unsupervised clustering of laminar and morphological features in 3D BigBrain. *NeuroImage* 206:116328. doi: 10.1016/j.neuroimage.2019.116328
- Diaz, B., Hintz, F., Kiebel, S. J., and Von Kriegstein, K. (2012). Dysfunction of the auditory thalamus in developmental dyslexia. *Proc. Natl. Acad. Sci. U.S.A.* 109, 13841–13846. doi: 10.1073/pnas.1119828109
- Dickscheid, T. (2021). *siibra – Python Interface for Interacting With Brain Atlases*. Available online at <https://github.com/EZJ-INMI-BDA/siibra-python> (accessed December 16, 2021).
- Dickscheid, T., Haas, S., Bludau, S., Glock, P., Huysegoms, M., and Amunts, K. (2019). Towards 3D reconstruction of neuronal cell distributions from histological human brain sections. *Adv. Paral. Comput.* 34, 223–239. doi: 10.3233/APC190016
- Ding, S.-L., Royall, J. J., Sunkin S. M., Ng, L., Facer, B. A. C., Lesnar, P., et al. (2016). Comprehensive cellular-resolution atlas of the adult human brain. *J. Comp. Neurol.* 524, 3127–3481. doi: 10.1002/cne.24080
- Dorph-Petersen, K.-A., Caric, D., Saghati, R., Zhang, W., Sampson, A. R., and Lewis, D. A. (2009). Volume and neuron number of the lateral geniculate nucleus in schizophrenia and mood disorders. *Acta Neuropathol.* 117, 369–384. doi: 10.1007/s00401-008-010-2
- Eidelberg, D., and Galaburda A. M. (1982). Symmetry and asymmetry in the human posterior thalamus. I. Cytoarchitectonic analysis in normal persons. *Arch. Neurol.* 39, 325–332. doi: 10.1001/archneur.1982.00510180003001
- Evans, A. C., Janke, A. L., Collins, D. L., and Baillet, S. (2012). Brain templates and atlases. *NeuroImage* 62, 911–922. doi: 10.1016/j.neuroimage.2012.01.024
- Ewert, S., Plettig, P., Li, N., Chakravarty, M. M., Collins, D. L., Herrington, T. M., et al. (2018). Toward defining deep brain stimulation targets in MNI space: a subcortical atlas based on multimodal MRI, histology and structural connectivity. *NeuroImage* 170, 271–282. doi: 10.1016/j.neuroimage.2017.05.015
- Florinbi, G., Torti, E., Masoli, S., D'Angelo, E., and Leporati, F. (2021). Granular layer simulator: Design and multi-GPU simulation of the cerebellar granular layer. *Front. Comput. Neurosci.* 15:630795. doi: 10.3389/fncom.2021.630795
- García-Gomar, M. G., Strong, C., Toschi, N., Singh, K., Rosen, B. R., Wald, L. L., et al. (2019). *In vivo* probabilistic structural atlas of the inferior and superior colliculi, medial and lateral geniculate nuclei and superior olivary complex in humans based on 7 Tesla MRI. *Front. Neurosci.* 13:764. doi: 10.3389/fnins.2019.00764
- Glendenning, K. K., and Masterton, R. B. (1998). Comparative morphometry of mammalian central auditory systems: variation in nuclei and form of the ascending system. *BBE* 51, 59–89. doi: 10.1159/00006530
- Harrison, J. M., and Howe, M. J. (1974). "Anatomy of the afferent auditory nervous system of mammals," in *Auditory System*, eds H. W. Ades, A. Axelsson, I. L. Baird, G. v. Békésy, R. L. Boord, C. B. G. Campbell, et al. (Berlin: Springer Berlin Heidelberg), 283–336.
- Hassler, R. (1959). "Anatomy of the thalamus," in *Introduction to Stereotaxic Operations With an Atlas of the Human Brain*, eds G. Schaltenbrand and P. Bailey (New York, NY: Georg Thieme Verlag).
- Hickman, S. J., Raouf, N., McLean, R. J., and Gottlob, I. (2014). Vision and multiple sclerosis. *Multip. Scleros. Relat. Disord.* 3, 3–16. doi: 10.1016/j.msard.2013.04.004
- Huber, L., Tse, D. H. Y., Wiggins, C. J., Uludag, K., Kashyap, S., Jangraw, D. C., et al. (2018). Ultra-high resolution blood volume fMRI and BOLD fMRI in humans at 9.4 T: capabilities and challenges. *NeuroImage* 178, 769–779. doi: 10.1016/j.neuroimage.2018.06.025
- Iglesias, J. E., Insausti, R., Lerma-Usabiaga, G., Bocchetta, M., van Leemput, K., Greve, D. N., et al. (2018). A probabilistic atlas of the human thalamic nuclei combining ex vivo MRI and histology. *NeuroImage* 183, 314–326. doi: 10.1016/j.neuroimage.2018.08.012
- Jia, K., Zamboni, E., Rua, C., Goncalves, N. R., Kemper, V., Ng, A. K. T., et al. (2021). A protocol for ultra-high field laminar fMRI in the human brain. *STAR Protoc.* 2:100415. doi: 10.1016/j.xpro.2021.100415
- Jonak, K., Krukow, P., Jonak, K. E., Radzikowska, E., Baj, J., Niedzialek, A., et al. (2020). Decreased volume of lateral and medial geniculate nuclei in patients with LHON disease-7 Tesh MRI study. *J. Clin. Med.* 9:2914. doi: 10.3390/jcm9092914
- Kitajima, M., Hirai, T., Yoneda T., Iryo, Y., Azuma, M., Tateishi, M., et al. (2015). Visualization of the medial and lateral geniculate nucleus on phase difference enhanced imaging. *Am. J. Neuroradiol.* 36, 1669–1674. doi: 10.3174/ajnr.A4356
- Kiwitz, K., Mohlberg, H., Brandstetter, A., Bludau, S., and Amunts, K. (2021a). *Probabilistic Cytoarchitectonic Map of the Human Corpus geniculatum laterale (CGL, LGB, Metathalamus) [Data set]*. EBRAINS. doi: 10.25493/1H7R-M3R
- Kiwitz, K., Mohlberg, H., Brandstetter, A., Bludau, S., and Amunts, K. (2021b). *Probabilistic Cytoarchitectonic Map of the Human Corpus geniculatum mediale (CGM, MGB, Metathalamus) [Data set]*. EBRAINS. doi: 10.25493/75TH-FE9
- Kiwitz, K., Schiffer, C., Brandstetter, A., Mohlberg, H., Amunts, K., and Dickscheid, T. (2021c). *Reference Delineations of the Human Corpus Geniculatum Mediale (CGM, MGB, MGB_l, MGB_m, Metathalamus) in Individual Sections of the BigBrain*. EBRAINS. doi: 10.25493/3SM6-HGM
- Kiwitz, K., Schiffer, C., Spitzer, H., Dickscheid, T., and Amunts, K. (2020). Deep learning networks reflect cytoarchitectonic features used in brain mapping. *Sci. Rep.* 10:22039. doi: 10.1038/s41598-020-78638-y

- Korsholm, K., Madsen, K. H., Frederiksen, J. L., Skimminge, A., and Lund, T. E. (2007). Recovery from optic neuritis: an ROI-based analysis of LGN and visual cortical areas. *Brain* 130, 1244–1253. doi: 10.1093/brain/awm045
- Krause, D., and Thörnig, P. (2018). JURECA: modular supercomputer at jülich supercomputing centre. *JLSRF* 4:132. doi: 10.17815/jlsrf-4-121-1
- Kranth, A., Blanc, R., Poveda, A., Jeanmonod, D., Morel, A., and Székely, G. (2010). A mean three-dimensional atlas of the human thalamus: generation from multiple histological data. *Neuroimage* 49, 2053–2062. doi: 10.1016/j.neuroimage.2009.10.042
- Kuhlenbeck, H. (1954). The human diencephalon; a summary of development, structure, function, and pathology. *Confin. Neurol.* 14, 1–230.
- Leaver, A. M., Renier, L., Chevillet, M. A., Morgan, S., Kim, H. J., and Rauschecker, J. P. (2011). Dysregulation of limbic and auditory networks in tinnitus. *Neuron* 69, 33–43. doi: 10.1016/j.neuron.2010.12.002
- Lee, J.-Y., Yoon, E. J., Lee, W. W., Kim, Y. K., Lee, J.-Y., and Jeon, B. (2016). Lateral geniculate atrophy in Parkinson's with visual hallucination: a trans-synaptic degeneration? *Mov. Disord.* 31, 547–554. doi: 10.1002/mds.26533
- Lewiner, T., Lopes, H., Vieira, A. W., and Tavares, G. (2003). Efficient implementation of marching cubes' cases with topological guarantees. *J. Graph. Tools* 8, 1–15. doi: 10.1080/10867651.2003.10487582
- Li, M., He, H. G., Shi, W., Li, J., Lv, B., Wang, C. H., et al. (2012). Quantification of the human lateral geniculate nucleus *in vivo* using MR imaging based on morphometry: volume loss with age. *Am. J. Neuroradiol.* 33, 915–921. doi: 10.3174/ajnr.A2884
- Lin, F. R., Ferrucci, L., An, Y., Goh, J. O., Doshi, J., Metter, E. J., et al. (2014). Association of hearing impairment with brain volume changes in older adults. *Neuroimage* 90, 84–92. doi: 10.1016/j.neuroimage.2013.12.059
- Llano, D. A., and Sherman, S. M. (2008). Evidence for nonreciprocal organization of the mouse auditory thalamocortical-corticothalamic projection systems. *J. Compar. Neurol.* 507, 1209–1227. doi: 10.1002/cne.21692
- Llinas, R. R., Leznik, E., and Urbano, F. J. (2002). Temporal binding via cortical coincidence detection of specific and nonspecific thalamocortical inputs: a voltage-dependent dye-imaging study in mouse brain slices. *Proc. Natl. Acad. Sci. U.S.A.* 99, 449–454. doi: 10.1073/pnas.012604899
- Mai, J. K., Berger, K., and Sofroniew, M. V. (1993). Morphometric evaluation of neurophysin-immunoreactivity in the human brain: pronounced inter-individual variability and evidence for altered staining patterns in schizophrenia. *J. Hirnforsch.* 34, 133–154.
- Mai, J. K., Majtanik, M., and Paxinos, G. (2016). *Atlas of the Human Brain*. Amsterdam: Elsevier AP.
- Margulies, D. S., Ghosh, S. S., Goulas, A., Falkiewicz, M., Huntenburg, J. M., Langs, G., et al. (2016). Situating the default-mode network along a principal gradient of macroscale cortical organization. *Proc. Natl. Acad. Sci. U.S.A.* 113, 12574–12579. doi: 10.1073/pnas.1608282113
- Martino, F., de Moerel, M., Ugurbil, K., Goebel, R., Yacoub, E., and Formisano, E. (2015). Frequency preference and attention effects across cortical depths in the human primary auditory cortex. *Proc. Natl. Acad. Sci. U.S.A.* 112, 16036–16041. doi: 10.1073/pnas.1507552112
- Merker, B. (1983). Silver staining of cell bodies by means of physical development. *J. Neurosci. Methods* 9, 235–241. doi: 10.1016/0165-0270(83)90086-9
- Mihai, P. G., Moerel, M., Martino, F., de Trampel, R., Kiebel, S., and von Kriegstein, K. (2019). Modulation of tonotopic ventral medial geniculate body is behaviorally relevant for speech recognition. *eLife Sci.* 8:44837. doi: 10.7554/eLife.44837
- Moerel, M., Martino, F., de Ugurbil, K., Yacoub, E., and Formisano, E. (2015). Processing of frequency and location in human subcortical auditory structures. *Sci. Rep.* 5:17048. doi: 10.1038/srep17048
- Morel, A. (2007). *Stereotactic Atlas of the Human Thalamus and Basal Ganglia*. New York, NY: Informa Healthcare.
- Morest, D. K. (1964). The neuronal architecture of the medial geniculate body of the cat. *J. Anat.* 98, 611–630.
- Najdenovska, E., Alemán-Gómez, Y., Battistella, G., Descoteaux, M., Hagmann, P., Jacquemont, S., et al. (2018). *In-vivo* probabilistic atlas of human thalamic nuclei based on diffusion-weighted magnetic resonance imaging. *Sci. Data* 5:180270. doi: 10.1038/sdata.2018.270
- Nasi, S., Polimeni, J. R., and Tootell, R. B. H. (2016). Interdigitated color- and disparity-selective columns within human visual cortical areas V2 and V3. *J. Neurosci.* 36, 1841–1857. doi: 10.1523/JNEUROSCI.3518-15.2016
- Omidiyeganeh, M., Lepage, C., Wagstyl, K., Spitzer, H., Dickscheid, T., Amunts, K., et al. (2020). "Non-linear registration of 1µm histology sections into 3D 20µm BigBrain space," in *2020 Organization for Human Brain Mapping Annual Meeting: A Virtual Experience for Engaging Minds & Empowering Brain Science*, ed. Organization for Human Brain Mapping (Minneapolis, MN: Organization for Human Brain Mapping).
- Papadopoulou, A., Gaetano, L., Pfister, A., Altermatt, A., Tsakas, C., Morency, F., et al. (2019). Damage of the lateral geniculate nucleus in MS: assessing the missing node of the visual pathway. *Neurology* 92, e2240–e2249. doi: 10.1212/WNL.00000000000007450
- Paquola, C., Seidlitz, J., Benkarim, O., Royer, J., Klimes, P., Bethlehem, R. A. I., et al. (2020b). A multi-scale cortical wiring space links cellular architecture and functional dynamics in the human brain. *PLoS Biol.* 18:e3000979. doi: 10.1371/journal.pbio.3000979
- Paquola, C., Benkarim, O., DeKraker, J., Larivière, S., Frässle, S., Royer, J., et al. (2020a). Convergence of cortical types and functional motifs in the human mesiotemporal lobe. *eLife Sci.* 9:60673. doi: 10.7554/eLife.60673
- Paquola, C., Royer, J., Lewis, L. B., Lepage, C., Glatard, T., Wagstyl, K., et al. (2021). BigBrainWarp: toolbox for integration of BigBrain 3D histology with multimodal neuroimaging. *bioRxiv* [Preprint]. Available online at: <https://www.biorxiv.org/content/10.1101/2021.05.04.442563v1> (accessed December 16, 2021).
- Paquola, C., Vos De Wael, R., Wagstyl, K., Bethlehem, R. A. I., Hong, S.-J., Seidlitz, J., et al. (2019). Microstructural and functional gradients are increasingly dissociated in transmodal cortices. *PLoS Biol.* 17:e3000284. doi: 10.1371/journal.pbio.3000284
- Pasu, S., Ridha, B. H., Wagh, V., Jindhra, P., Siddiqui, A., Plant, G., et al. (2015). Homonymous sectoranopia: asymptomatic presentation of a lateral geniculate nucleus lesion. *Neuroophthalmology* 39, 289–294. doi: 10.3109/01658107.2015.1079221
- Peruzzi, D., Bartlett, E., Smith, P. H., and Oliver, D. L. (1997). A monosynaptic GABAergic input from the inferior colliculus to the medial geniculate body in rat. *J. Neurosci.* 17, 3766–3777. doi: 10.1523/JNEUROSCI.17-10-03766.1997
- Qian, Z. J., Chang, P. D., Moons, G., and Lalwani, A. K. (2017). A novel method of quantifying brain atrophy associated with age-related hearing loss. *NeuroImage Clin.* 16, 205–209. doi: 10.1016/j.nicl.2017.07.021
- Rademacher, J., Bürgel, U., and Zilles, K. (2002). Stereotaxic localization, intersubject variability, and interhemispheric differences of the human auditory thalamocortical system. *Neuroimage* 17, 142–160. doi: 10.1006/nimg.2002.1178
- Rauschecker, J. P., Leaver, A. M., and Mühlau, M. (2010). Tuning out the noise: limbic-auditory interactions in tinnitus. *Neuron* 66, 819–826. doi: 10.1016/j.neuron.2010.04.032
- Ridder, D., de Vanneste, S., Lazguth, B., and Llinas, R. (2015). Thalamocortical dysrhythmia: a theoretical update in tinnitus. *Front. Neurol.* 6:124. doi: 10.3389/fneur.2015.00124
- Rijk, M. M., de van den Hurk, J., Rahnama'i, M. S., and van Koeveeringe, G. A. (2021). Parcellation of human periaqueductal gray at 7-T fMRI in full and empty bladder state: the foundation to study dynamic connectivity changes related to lower urinary tract functioning. *NeuroUrol. Urodynam.* 40, 616–623. doi: 10.1002/nau.24602
- Royer, J., Paquola, C., Larivière, S., Vos De Wael, R., Tavakol, S., Lowe, A. J., et al. (2020). Myeloarchitecture gradients in the human insula: Histological underpinnings and association to intrinsic functional connectivity. *Neuroimage* 216:116859. doi: 10.1016/j.neuroimage.2020.116859
- Saint Marie, R. L., Stanforth, D., and Jubelier, E. (1997). Substrate for rapid feedforward inhibition of the auditory forebrain. *Brain Res.* 765, 173–176. doi: 10.1016/S0006-8993(97)00654-9
- Schiffer, C., Spitzer, H., Kiwitz, K., Unger, N., Wagstyl, K., Evans, A. C., et al. (2021c). Convolutional neural networks for cytoarchitectonic brain mapping at large scale. *Neuroimage* 240:118327. doi: 10.1016/j.neuroimage.2021.118327
- Schiffer, C., Brandstetter, A., Bolakhrif, N., Mohlberg, H., Amunts, K., and Dickscheid, T. (2021a). *UltraHigh Resolution 3D Cytoarchitectonic Map of the LGB (Lam 1-6, CGL, Metathalamus) Created by a Deep-Learning Assisted Workflow*. EBRAINS. doi: 10.25493/33Z0-BX
- Schiffer, C., Kiwitz, K., Brandstetter, A., Mohlberg, H., Amunts, K., and Dickscheid, T. (2021b). *UltraHigh Resolution 3D Cytoarchitectonic map of the Human Corpus*

- Geniculatum Mediale* (CGM, MGB, MGBv, MGBd, MGBm, *Metathalamus*). EBRAINS. doi: 10.25493/PNY0-NCW
- Schmidt, M., Bakker, R., Shen, K., Bezgin, G., Diesmann, M., and van Albada, S. J. (2018). A multi-scale layer-resolved spiking network model of resting-state dynamics in macaque visual cortical areas. *PLoS Comput. Biol.* 14:e1006359. doi: 10.1371/journal.pcbi.1006359
- Schurr, R., and Mezer, A. A. (2021). The glial framework reveals white matter fiber architecture in human and primate brains. *Science* 374, 762–767. doi: 10.1126/science.abb7960
- Selemon, L. D., and Begovic, A. (2007). Stereologic analysis of the lateral geniculate nucleus of the thalamus in normal and schizophrenic subjects. *Psychiatry Res.* 151, 1–10. doi: 10.1016/j.psychres.2006.11.003
- Sepulcre, J., Goñi, J., Masdeu, J. C., Bejarano, B., Velez de Mendizábal, N., Toledo, J. B., et al. (2009). Contribution of white matter lesions to gray matter atrophy in multiple sclerosis: evidence from voxel-based analysis of T1 lesions in the visual pathway. *Arch. Neurol.* 66, 173–179. doi: 10.1001/archneurol.2008.562
- Sitek, K. R., Gulban, O. F., Calabrese, E., Johnson, G. A., Lage-Castellanos, A., Moerel, M., et al. (2019). Mapping the human subcortical auditory system using histology, postmortem MRI and in vivo MRI at 7T. *eLife* 8:e48932. doi: 10.7554/eLife.48932
- Smit, J. V., Janssen, M. L. F., van Zwieten, G., Jahanshahi, A., Temel, Y., and Stokroos, R. I. (2016). Deep brain stimulation of the inferior colliculus in the rodent suppresses tinnitus. *Brain Res.* 1650, 118–124. doi: 10.1016/j.brainres.2016.08.046
- Stanton, S. G., and Harrison, R. V. (2000). Projections from the medial geniculate body to primary auditory cortex in neonatally deafened cats. *J. Compar. Neurol.* 426, 117–129. doi: 10.1002/1096-9861(20001009)426:1<117:AID-CNE8<3.0.CO;2-S
- Stein, J. D., Khawaja, A. P., and Weizer, J. S. (2021). Glaucoma in adults—screening, diagnosis, and management: a review. *JAMA* 325, 164–174. doi: 10.1001/jama.2020.21899
- Strick, P. L., and Sterling, P. (1974). Synaptic termination of afferents from the ventrolateral nucleus of the thalamus in the cat motor cortex. A light and electron microscopy study. *J. Comp. Neurol.* 153, 77–106. doi: 10.1002/cne.901530107
- Usrey, W. M., and Allitto, H. J. (2015). Visual functions of the thalamus. *Annu. Rev. Vis. Sci.* 1, 351–371. doi: 10.1146/annurev-vision-082114-035920
- van Zwieten, G., Roberts, M. J., Schaper, F. L. V. W., Smit, J. V., Temel, Y., and Janssen, M. L. F. (2021). Noise-induced neurophysiological alterations in the rat medial geniculate body and thalamocortical desynchronization by deep brain stimulation. *J. Neurophysiol.* 125, 661–671. doi: 10.1152/jn.00752.2019
- Wagstyl, K., Larocque, S., Cucurull, G., Lepage, C., Cohen, J. P., Bludau, S., et al. (2020). BigBrain 3D atlas of cortical layers: cortical and laminar thickness gradients diverge in sensory and motor cortices. *PLoS Biol.* 18:e3000678. doi: 10.1371/journal.pbio.3000678
- Wang, J., Miao, W., Li, J., Li, M., Zhen, Z., Sabel, B., et al. (2015). Automatic segmentation of the lateral geniculate nucleus: application to control and glaucoma patients. *J. Neurosci. Methods* 255, 104–114. doi: 10.1016/j.jneumeth.2015.08.006
- Wei, Y., Scholtens, L. H., Turl, E., and van den Heuvel, M. P. (2019). Multiscale examination of cytoarchitectonic similarity and human brain connectivity. *Netw. Neurosci.* 3, 124–137. doi: 10.1162/netn_a_00057
- Winer, J. A. (1984). The human medial geniculate body. *Hear. Res.* 15, 225–247. doi: 10.1016/0378-5955(84)90031-5
- Winer, J. A. (1992). "The functional architecture of the medial geniculate body and the primary auditory cortex." in *The Mammalian Auditory Pathway: Neuroanatomy*, eds R. R. Fay, A. N. Popper, and D. B. Webster (New York, NY: Springer New York), 222–409.
- Wong, C., Chabot, N., Kok, M. A., and Lomber, S. G. (2014). Modified areal cartography in auditory cortex following early- and late-onset deafness. *Cereb. Cortex* 24, 1778–1792. doi: 10.1093/cercor/bht026
- Zvorykin, V. P. (1980). Novoe voproshe ob individual'nykh kolichestvennykh osobennostiakh lateral'nogo kolenchatogo tela cheloveka. *Arkh. Anat. Gistol. Embriol.* 78, 24–27.

Conflict of Interest: The authors declare that the research was conducted in the absence of any commercial or financial relationships that could be construed as a potential conflict of interest.

Publisher's Note: All claims expressed in this article are solely those of the authors and do not necessarily represent those of their affiliated organizations, or those of the publisher, the editors and the reviewers. Any product that may be evaluated in this article, or claim that may be made by its manufacturer, is not guaranteed or endorsed by the publisher.

Copyright © 2022 Kiwitz, Brandstetter, Schäffer, Bludau, Mohlberg, Omidyeganeh, Massicotte and Amunts. This is an open-access article distributed under the terms of the Creative Commons Attribution License (CC BY). The use, distribution or reproduction in other forums is permitted, provided the original author(s) and the copyright owner(s) are credited and that the original publication in this journal is cited, in accordance with accepted academic practice. No use, distribution or reproduction is permitted which does not comply with these terms.

Study 3

Deep learning networks reflect cytoarchitectonic features used in brain mapping

Kai Kiwitz^{1,2}, Christian Schiffer³, Hannah Spitzer⁴, Timo Dickscheid³, Katrin
Amunts^{1,2,3}

¹Cécile and Oskar Vogt Institute of Brain Research, Univ. Hospital Düsseldorf,
Heinrich-Heine University Düsseldorf, Germany

²Max Planck School of Cognition, Stephanstrasse 1a, Leipzig, Germany

³Institute of Neuroscience and Medicine (INM-1), Forschungszentrum Jülich, Germany

⁴Institute of Computational Biology, Helmholtz Zentrum München, Germany



OPEN Deep learning networks reflect cytoarchitectonic features used in brain mapping

Kai Kiwitz^{1,2}✉, Christian Schiffer³, Hannah Spitzer⁴, Timo Dickscheid³ & Katrin Amunts^{1,2,3}

The distribution of neurons in the cortex (*cytoarchitecture*) differs between cortical areas and constitutes the basis for structural maps of the human brain. Deep learning approaches provide a promising alternative to overcome throughput limitations of currently used cytoarchitectonic mapping methods, but typically lack insight as to what extent they follow cytoarchitectonic principles. We therefore investigated in how far the internal structure of deep convolutional neural networks trained for cytoarchitectonic brain mapping reflect traditional cytoarchitectonic features, and compared them to features of the current grey level index (GLI) profile approach. The networks consisted of a 10-block deep convolutional architecture trained to segment the primary and secondary visual cortex. Filter activations of the networks served to analyse resemblances to traditional cytoarchitectonic features and comparisons to the GLI profile approach. Our analysis revealed resemblances to cellular, laminar- as well as cortical area related cytoarchitectonic features. The networks learned filter activations that reflect the distinct cytoarchitecture of the segmented cortical areas with special regard to their laminar organization and compared well to statistical criteria of the GLI profile approach. These results confirm an incorporation of relevant cytoarchitectonic features in the deep convolutional neural networks and mark them as a valid support for high-throughput cytoarchitectonic mapping workflows.

The human brain is not only target of the application of artificial neural networks (ANNs) to study its organization, it also represents a natural network of enormous complexity and power, which inspired their development. This has created a unique, bi-directional relationship throughout the last decades between research on brain organization and the application and development of ANNs^{1–7}. Trying to understand the details of how modern ANNs internally operate is an ongoing endeavour and prerequisite to explain their results⁸, and led to the emerging research field of explainable AI. Due to the special relationship between brain organization and ANNs, such insights are of special interest when applying ANNs to study brain organization itself.

The brain contains neuronal networks formed by axons and dendrites, which connect neurons in different brain regions. Neurons of the cerebral cortex are organized in layers and columns⁹. The distribution, arrangement and presence of neurons (*cytoarchitecture*) differs between brain regions and is associated with connectivity and functional differences^{11,12}. Cytoarchitecture can be studied in histological sections stained for cell bodies¹³. Traditional cytoarchitectonic features include cell size, cell density, laminar thickness and arrangement, columnar arrangement of cells, cellular clustering, cortical thickness, as well as the sharpness of the white matter/grey matter border^{10,11,13–15}. Figure 1 illustrates the cytoarchitecture of the primary visual cortex (Brodmann Area 17, hOc1, or V1, from here on called hOc1), the secondary visual cortex (hOc2, Brodmann Area 18, or V2, from here on called hOc2), and the ventrally adjoining area hOc3v^{16,17}, which are part of a complex biological network for processing visual information¹⁸. While all three areas show the typical 6-layer structure of the isocortex, they differ with respect to their cytoarchitecture and role in information processing.

Previous studies of our own group have analysed the cytoarchitecture of areas hOc1, hOc2¹⁶ and hOc3v¹⁷. Borders between the areas were identified based on computerized image analysis and statistical tests^{16,17}. Such methods based on quantitative measures enable a reproducible identification of borders^{19–22}. The current state-of-the-art method for quantitative cytoarchitectonic analysis is based on the grey level index (GLI) as a measure of the volume fraction of cell bodies extracted along traverses¹⁹. The latter are defined along the Laplacian field from the cortical layer I/layer II border to the white matter border on GLI images^{20,21,23}. The resulting GLI profiles

¹Cécile and Oskar Vogt Institute of Brain Research, Univ. Hospital Düsseldorf, Heinrich-Heine University, Düsseldorf, Germany. ²Max Planck School of Cognition, Stephanstrasse 1a, Leipzig, Germany. ³Institute of Neuroscience and Medicine (INM-1), Forschungszentrum Jülich, Jülich, Germany. ⁴Institute of Computational Biology, Helmholtz Zentrum, München, Germany. ✉email: kai.kiwitz@med.uni-duesseldorf.de

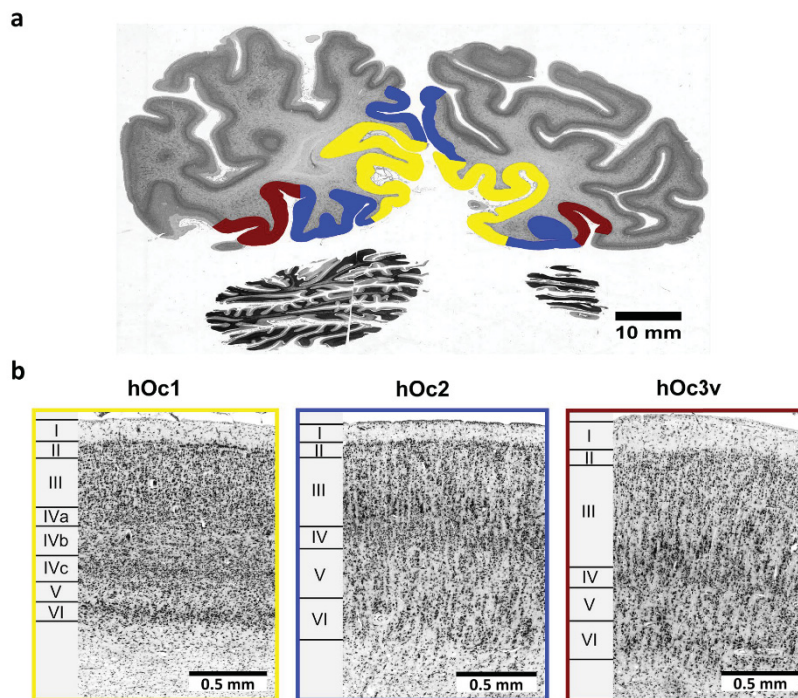


Figure 1. Cytoarchitecture of cortical areas of the visual system. (a) Histological cell-body stained section (section 901) from the occipital lobe of the BigBrain dataset with cortical areas hOc1 (yellow), hOc2 (blue) and hOc3v (brown)^{16,17}. (b) Cytoarchitecture of cortical areas hOc1, hOc2 and hOc3v extracted from (a). Roman numerals indicate cortical layers. Area hOc1 is characterized by a prominent cortical layer IV, subdivided into sublayers IVa, IVb and IVc. Sublayer IVc shows the highest cell-density and constitutes the cortical input layer for visual information from the thalamus²³. Cortical layer III and V contain small cells with the cell-sparse layer V being easily distinguishable from cortical layer VI^{10,16}. In area hOc2, the size of pyramidal cells in cortical layer III steadily increases from upper to lower levels of the layer. Cortical layer IV is thinner than in area hOc1 and the contrast in density between cortical layer V and VI is not as high. The overall clarity of a columnar arrangement also appears increased¹⁶. Neighbouring area hOc3v has a moderate cell-density^{16,17}. The three cortical areas show distinct structural-functional relationships revealed by neuroscientific investigations, including topographic organization^{54–57}, columnar organization^{58–60} and interhemispheric connectivity^{61–64}.

reflect the cytoarchitecture and feature vectors are extracted to analyse changes in cytoarchitecture while moving across the cortical ribbon. The feature vectors contain the mean GLI value and the first four central moments about the mean: mean, standard deviation, skewness and kurtosis, as well as values of the differential quotient of the profile^{19,21}. A sliding-window approach captures borders between cortical areas based on multivariate difference functions of the feature vectors¹⁹. This approach has allowed to identify areas in serial histological sections, to 3D reconstruct their extent, and to compute probabilistic maps as part of the *Jülich-Brain atlas*^{11,24–26}. It has been applied for more than 100 areas.

Alternative approaches have been proposed for cortical mapping, e.g. excess mass functionals in the feature vectors to establish a relation to differences in cortical lamination in consecutive profiles²². This reduces the complex shape of the profile to the number of local peaks and their differences²². Others have applied wavelet analysis to bundle profile data in large wavelet coefficients²⁷. However, it is not always straightforward to interpret such transformations of the extracted profiles with respect to the original histological data since it is necessary to determine which features of a wavelet transform should be analysed in a second step²². Additionally, wavelet analysis represents profile descriptions at an abstract level that can hardly be related to underlying cytoarchitectonic properties of the histological tissue.

All approaches have in common that the extracted profile features only partly reflect traditional cytoarchitectonic criteria, but focus on statistical image criteria to detect laminar differences in the cellular pattern. The

feature vector for statistical analysis in the current GLI profile approach allows to interpret them with respect to cytoarchitecture, e.g., mean cell packing density (mean GLI feature), or differences in cell density between supra- and infragranular cortical layers (e.g., skewness feature)^{21,23}. However, such a reasoning cannot be made unequivocally since one and the same GLI value can result from a lower numerical density of large neurons and a higher density of small neurons²³. While cytoarchitectonic analyses in mapping studies have benefited significantly from the GLI profile approach, recent developments of high-resolution models like the BigBrain dataset with more than 7400 stained histological sections¹⁸ challenge the throughput for future studies.

Deep learning techniques constitute a new and promising alternative in the dynamically evolving field of medical image analysis^{29–33}, which potentially enable the segmentation of cortical areas in more sections as compared to the GLI profile approach. Deep ANNs have already led to robust and accurate results for cell detection in histopathological images^{23,34–36}. The U-Net architecture³⁴ is highly effective for biomedical image segmentation in this regard by using a deep convolutional neural network (CNN) approach, which we adapted for segmenting cortical areas on histological data in our own lab. It showed that the approach generates spatially consistent segmentations across sections that are transferable to other brains with high throughput^{37,38}.

To further evaluate whether this approach is adequate to support cytoarchitectonic brain mapping, an in-depth comparison between the current GLI profile approach and deep learning-based mapping is required. We therefore analysed the internal structure of deep CNNs trained to segment different cortical areas in images of cell-body stained histological sections of the human brain. This included to evaluate in how far the internal structure of the trained networks reflect traditional cytoarchitectonic features on the cellular and laminar level of cortical areas. In addition, the laminar and cellular features reflected by the current GLI profile approach were compared to the features learned by the networks, and correspondences and dissimilarities between mapping results were analysed in regions of interest. The study was performed in the visual cortex of the BigBrain dataset—a frequently used, high-resolution brain model, for which all sections were histologically processed, stained, imaged and 3D-reconstructed¹⁸.

Methods

Cytoarchitectonic mapping based on GLI profiles. Cytoarchitectonic analysis was performed on histological sections of the BigBrain dataset¹⁸. This dataset consists of 7404 coronal, 20 µm thick, cell-body stained sections of a complete paraffin-embedded human brain¹⁸. The brain was originally obtained in accordance to legal and ethical regulations and guidelines as part of the body donor program of the Department of Anatomy of the Heinrich Heine University Düsseldorf. The body donor (65 years old, male) gave written informed consent for the general use of post-mortem tissue for aims of research and education. All usage in this work is covered by a vote of the ethics committee of the Medical Faculty of the Heinrich Heine University Düsseldorf (#4863). The numbering of the dataset starts at the occipital pole (section 1) and ends at the frontal pole (section 7404). For cytoarchitectonic analysis, a region of interest covering the primary visual cortex (hOc1) with its distinct cytoarchitecture, and the surrounding secondary visual cortex (hOc2) was chosen (Fig. 1). Both areas reach from the occipital pole to the parieto-occipital sulcus¹⁶ and are located between sections 1 and 2461 in the BigBrain dataset. The 3D-reconstructed BigBrain dataset and annotations of the areas are available online (<https://interactive-viewer.apps.hbp.eu/>).

The GLI profile approach was performed on three digitized sections (section 0961, 1021 and 1081) covering a distance of 2.4 mm. They represent the centre of the designated region of interest in the BigBrain dataset. Mean profile shapes have been extracted and borders between hOc1 and hOc2, as well as to ventrally and dorsally neighbouring areas hOc3v¹⁷ and hOc3d¹⁹ have been identified (Fig. 2). The resulting mappings on sections 0961 and 1081 served for training the deep CNNs. Mappings on section 1021 constituted a reference for analysing the CNNs' internal structure and validating their segmentation performance.

CNN based cytoarchitectonic mapping. Two CNNs were trained to segment cortical areas hOc1 and hOc2 on all 119 sections in between the training sections. The network architecture of the CNNs consisted of 10 blocks with 24 network layers modelled after the well-established U-Net architecture³⁴, including modifications proposed which have been shown to work well for the task of cytoarchitectonic area segmentation^{37,40}. We trained two separate instances of the same CNN architecture for cortical areas hOc1 and hOc2 by using the mappings on the training sections as well as classified volume information of the BigBrain dataset in its 2015 version (<https://bigbrain.loris.ca/main.php?>)⁴¹, including grey matter, white matter and background classifications. Other than conventional U-Nets, each instance comprised a high- and a low-resolution contracting branch with a larger field of view connected to a single expanding branch (Fig. 3), allowing the model to efficiently capture fine-grained cytoarchitectonic features, as well as coarse-grained morphological properties of the surrounding tissue. All branches consisted of 864 network units leading to a total of 2592 units per CNN. As the use of fine-tuned weights from a pre-trained network has shown to be beneficial in comparison to the use of random initialized weights⁴², we adopted weights from a successful auxiliary deep learning model developed in our lab, which has proven to boost segmentation performance among visual cortices³⁸. In each training iteration the CNNs were shown patches sampled equally from white matter, background, the cortical area of interest (hOc1 or hOc2) and other cortex to assure a balanced training. The high-resolution contracting branches of the CNNs were shown a 4.05 × 4.05 mm patch (2025 × 2025 pixels at 2 micron per pixel) capturing fine-grained cytoarchitectonic features; the low-resolution contracting branches were shown a 17.97 × 17.97 mm patch (1123 × 1123 pixels at 16 micron per pixel) to capture coarse-grained morphological properties of the surrounding tissue⁴⁰.

Feature visualizations and feature identification. In response to being presented with the validation section, each unit of the two CNNs generated an activation (*filter activation*). For an analysis of the internal

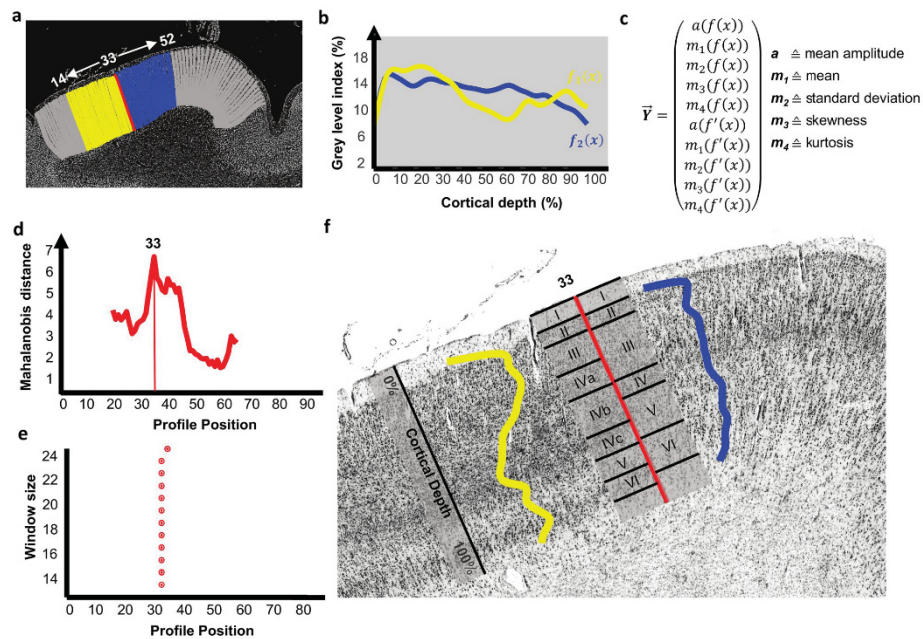


Figure 2. Illustration of the GLI profile approach for cytoarchitectonic analysis^{19–21,23,47}. (a) shows profiles (19 yellow and 19 blue) around a target profile (red, number 33) on a GLI image of a region of interest in the occipital lobe of the BigBrain dataset²⁸. The graph in (b) depicts mean profiles from each of the 19 profiles from (a). (c) shows the feature vector used to quantify the shape of the mean profiles in (b) by interpreting them as frequency distributions. The feature vector consists of the mean amplitude of the distribution, the first 4 central moments as well as the first derivatives of the later. (d) illustrates the multivariate Mahalanobis distance metric between feature vectors generated from a sliding window approach with window size 19. It indicates a significant global maximum of differences between feature vectors at profile position 33. Significant global maxima for different window sizes in (e) confirm the detection of a border at position 33. (f) shows the detected border (red bar) displayed on the histological section used in (a). Roman numerals indicate cortical layers. Superimpositions of the profiles from (b) reveal correspondences to cytoarchitectonic features and reflect differences in lamination and cellular composition between cortical area hOc1 on the left and hOc2 on the right side of the detected border²⁵. These include a clear differentiation of cortical layer IV reflected by differences in GLI profile shapes, as well as differences in the excess of the profile shapes at cortical depths relating to cortical layer IVc to VI in area hOc1 and IV to VI in area hOc2. In area hOc1, the broad and cell-dense cortical layer IVc contrasts the cell-sparse layer V which in return can easily be distinguished from the darkly stained layer VI. Whereas in area hOc2 the thinner cortical layer IV does not stand out from the less distinguishable layer V and VI to the same amount in the GLI profile shapes.

structure of the CNNs, these filter activations were calculated by using the Rectified Linear Unit (ReLU) outputs within the high-resolution contracting and expanding branches of the hOc1 and hOc2 CNNs. To reduce differences among output values, a normalization to an interval of [0.0, 1.0] was applied with the smallest value larger than 0 serving as the lower bound. Thus, each filter activation constitutes a whole image whose resolution is defined by the network layer it was calculated from. This resulted in 2592 filter activations for each of the hOc1 and hOc2 CNNs (5184 in total) on the validation section. Since the number of dimensions (118.383.390 pixels on the validation section) exceeded the number of data points (2592 filter activations) by a factor of over 10.000, dimensionality reducing methods like a principal component analysis are not suited to categorize similar components among the filter activations. Therefore, a three-step categorization workflow was applied to evaluate whether the internal structure of the CNNs reflect traditional cytoarchitectonic features: (i) identification of groups of similar filter activations across each CNN; (ii) identification of characteristic filter activations for each layer of a CNN and (iii) identification of cytoarchitectonically relevant features among the characteristic filter activations. In detail:

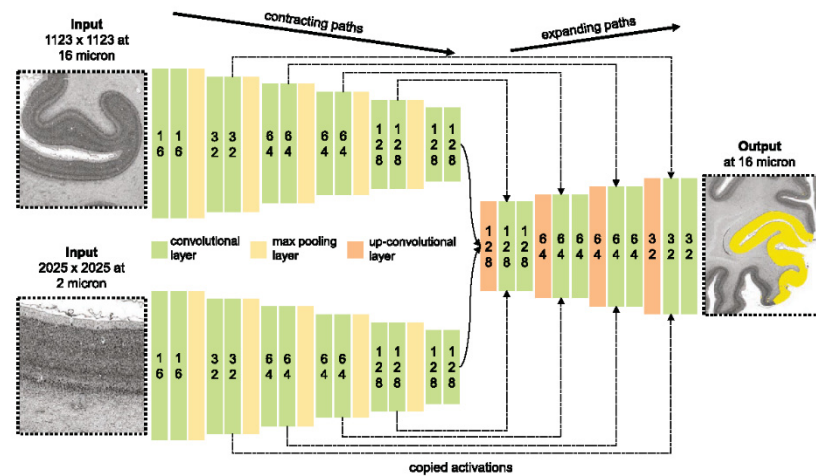


Figure 3. Scheme of the used CNN architecture inspired by the U-Net³⁴. The blocks in the contracting branches consist of two convolutional layers and a pooling layer. The output of each convolution is parsed through a batch normalization and a rectified linear unit (ReLU). Each block in the expanding branch consists of an up-convolutional and two convolutional layers, each followed by a batch normalization and a ReLU. High resolution activations from the contracting path are combined with the outputs of the up-convolutional layers in the expanding branch. Numbers in boxes indicate the number of network units in a respective layer. All branches consist of 864 network units leading to a total of 2592 units per CNN.

(i) Mutual Information served as a metric to identify similar filter activations for each CNN. We adopted the idea from medial image registration techniques that make use of mutual information of images^{43,44}. In our case, the normalized activation interval $[0.0, 1.0]$ of the ReLUs of two filter activations were used and transformed into one-dimensional and two-dimensional histograms with a binning frequency of 255 to calculate the mutual information of two filter activations. The joint histogram was determined using

$$p_{ij}^{xy} = \frac{1}{N} \sum_{x \in X} \sum_{y \in Y} 1\left(\frac{i}{256} \leq x < \frac{i+1}{256}\right) * 1\left(\frac{j}{256} \leq y < \frac{j+1}{256}\right)$$

relative to the size of the filter activation maps ($N = |X| = |Y|$) with an indicator function (1). This step was repeated for every combination of the 2592 filter activations of each CNN.

(ii) To identify characteristic filter activations for each layer of a CNN, a pairwise mutual information matrix for all filter activations was generated for each CNN. Compilations of twelve filter activations with the highest pairwise mutual information for each filter activation of a CNN served to identify characteristic filter activations.

The compilations were analysed at a location within the validation section belonging to cortical area hOc1 or hOc2. Due to the increasingly lower resolution of the filter activations in deeper network layers (> layer 12) the whole section was analysed for the respective network layers. Filter activations were colour-coded for the analysis with a colour map that emphasizes lightness changes over changes in hue—a principle adopted from human colour perception⁴⁵. As expected, filter activations with high mutual information exhibit very similar characteristics, justifying the choice of mutual information as a similarity metric (Fig. 4a). When a filter activation appeared similar to at least three other filter activations of the same network layer, it was determined to be characteristic for that network layer (Fig. 4b–d). This threshold was set to account for the different numbers of network units per network layer. A higher threshold prevents finding characteristic filter activations on superficial network layers with a small number of network units; whereas a lower threshold leads to a very high number of characteristic filter activations in deeper network layers with more units.

(iii) In a final step, the cytoarchitecturally relevant features among the characteristic filter activations were identified. Therefore, three categories of cytoarchitectonic features in accordance to traditional cytoarchitectonic features^{10,14} were defined:

- *first level features*, which are related to different shapes of cell bodies
- *second level features*, which are related to differences in thickness and composition of cortical layers
- *third level features*, which are related to differences at the level of cortical areas including their borders and extent.

Figure 4. Mutual information compilations (a) and identification of characteristic filter activations (b–d) of network layer four from the hOc1 CNN. The two left images in (a) show the region of interest on the validation section (section 1021) in which the filter activations are visualized. Images on the right show two compilations of filter activations containing the lowest (upper right) and highest (bottom right) mutual information compared to reference filter activations (central images) across all network layers. (b–d) illustrate compilations of highest mutual information compared to different reference filter activations (central images). (b) contains two compilations with no characteristic filter activation in the middle since the criterion for similar appearance is not met. (c) contains two compilations with characteristic filter activations with all criteria met. Green asterisks mark similar-appearing filter activations. (d) contains compilations that appear similar to the reference but do not meet the criterion of at least three filter activations from the same network layer (green asterisks). Most similar-appearing filter activations belong to other network layers (red asterisks).

When a characteristic filter activation fit into one of the three categories, it was identified to be cytoarchitecturally relevant and labelled a first, second or third level filter activation. The identification was performed by a neuroanatomical expert, who compared the characteristic filter activation to the three categories of traditional cytoarchitectonic features. Superimpositions of characteristic filter activations on the validation section enabled the identification of cytoarchitecturally relevant features among them. The size of the validation section alone constituted 15.1 Gigabyte with pixel dimensions of $94,321 \times 80,326$ (8-bit greyscale). To enable an analysis of such large datasets, we used the MicroDraw software⁶, due to its capability of displaying the superimpositions on large image data.

Comparison of feature visualizations to the GLI profile approach. First, second and third level filter activations were compared to cytoarchitectonic features as revealed by the GLI profile approach^{19,20,23}. The analysis included comparisons to cellular and laminar features reflected by the GLI profile approach, as well as mapping results of the border detection. The former was achieved by comparing first level filter activations to cell-related structures in a GLI image of the validation section. A comparison of second level filter activations to mean GLI profile shapes was used for a comparison of laminar features. Profile shapes were calculated from 25 profiles of the GLI image of the validation section. Locations of borders on the validation section detected by the GLI profile approach constituted a reference for comparing third level filter activations.

Results

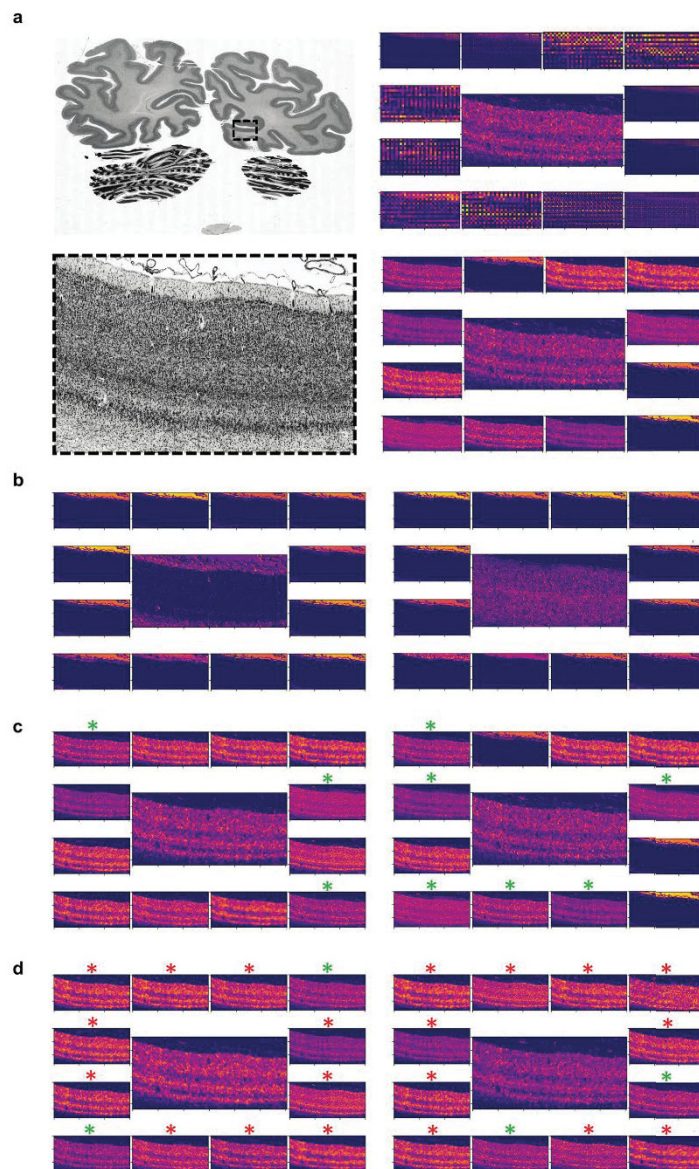
The analysis of the internal structure revealed a similar distribution of cytoarchitecturally relevant features among both CNNs trained to segment cortical areas hOc1 and hOc2. We detected first, second and third level filter activations in the hOc1 and hOc2 CNNs. First level filter activations were found on superficial network layers in the hOc1 and hOc2 CNNs, followed by second level filter activations on intermediate and third level filter activations in deeper network layers (Table 1). Thus, filter activations appeared in a similar successive manner within both CNNs. The most striking difference between the hOc1 and hOc2 CNNs constituted the internetwork quality of second level filter activations, which is described in more detail in the following sections.

Cytoarchitectonic features of cortical areas on the cellular and laminar level. First level filter activations were found on network layers one to six in the contracting branches of the hOc1 and hOc2 CNNs. In total, we found ten of them in the hOc1 CNN and 19 in the hOc2 CNN. They mainly responded to cell bodies in the cortex. When comparing the first level filter activations to the histologically stained validation section (Fig. 5a), cell-related properties of the histological image appear reflected in the filter activations. Examples for such correspondences are the cell-dense cortical layer IVc of area hOc1 (Fig. 5a) and large pyramidal cells in cortical layer IIIc of area hOc2 (Fig. 5b). In general, the first level filter activations did not show consistent variations.

Second level filter activations occurred on network layers five to ten in the contracting branch of the hOc1 CNN, as well as five, seven, eight, nine and ten of the hOc2 CNN. In total, we found 45 in the hOc1 and 17 in the hOc2 CNN. A superimposition of a second level filter activation from the hOc1 CNN on histological data shows locally restricted activations within bounds of cell-densely packed cortical layers III, IVa, IVc and VI (Fig. 6a). In general, the 45 filter activations revealed only little variations in the strength of activations in cortical layer III. Cell-dense cortical layers IVa, IVc and VI showed consistently high activations. No second level filter activations responding to cell-sparse layers of the cortex were found in the hOc1 CNN.

Two different classes of second level filter activations occurred in the hOc2 CNN. The two classes constituted 17 second level filter activations showing activations to cell-dense cortical layers II and IV and four responding to the more cell-sparse cortical layers III and V. Figure 6b presents a superimposition of a second level filter activation from the hOc2 CNN which stays within bounds of cell-sparse cortical layers III and V. In general, the second level filter activations of the hOc2 CNN showed varying strengths of activations related to cortical layer I, the background as well as the white matter.

Comparisons to cellular and laminar features reflected by the current GLI profile approach. The first level filter activations of the hOc1 and hOc2 CNNs revealed correspondences to cell-related structures in GLI images of the validation section. Examples constitute the dense cortical layer IVc in area hOc1 which appears as a dense white band in the GLI image (Fig. 5a) and big pyramidal cells in area hOc2 reflected by grossly-grained white dots in the GLI image (Fig. 5b). Note, that Fig. 5b depicts a part of cortical area hOc2 where the presence



	Distribution of first, second and third level filter activations in both networks					
	First level filter activations		Second level filter activations		Third level filter activations	
	hOc1 CNN	hOc2 CNN	hOc1 CNN	hOc2 CNN	hOc1 CNN	hOc2 CNN
Layer 1	x	x				
Layer 2	x	x				
Layer 3	x	x				
Layer 4	x	x				
Layer 5	x	x	x	x		
Layer 6	x	x	x			
Layer 7			x	x		
Layer 8			x	x		
Layer 9			x	x		
Layer 10			x	x		
Layer 11						
Layer 12						
Layer 13					x	x
Layer 14					x	x
Layer 15					x	
Layer 16					x	x
Layer 17					x	x
Layer 18					x	x
Layer 19					x	x
Layer 20					x	x
Layer 21					x	x
Layer 22					x	x
Layer 23					x	x
Layer 24					x	x

Table 1. Distribution of first, second and third level filter activations among the network layers of the two CNNs. The requirements for a filter activation to be classified as a first, second or third level filter activation are described in the methods section. Crossmarks indicate the existence of first, second or third level filter activations among the characteristic filter activations of a specific network layer.

of big pyramidal cells in cortical layer IIIc alternates (left side: present; right side: non-present). This special cyto-architectonic feature of cortical area hOc2¹⁴ is also reflected in the displayed filter activation and the GLI image.

Additionally, second level filter activations revealed correspondences to GLI profile shapes. Local maxima of the profile shapes reflect second level filter activations that respond to cell-densely packed cortical layers IVc and VI in area hOc1 (Fig. 6a). On the contrary, minima of the GLI profile shape correspond to the low filter activations of cell-sparse cortical layers IVa and V (Fig. 6a). The overall high response to cortical layer III also compares to the overall high GLI values in this layer. In area hOc2, local minima of the GLI profile shapes reflect second level filter activations responding to cell-sparse cortical layers III and V (Fig. 6b). High GLI values and local maxima of the profile shapes correspond to low filter activations in cell-dense cortical layers II and IV as well as the darkly stained cortical layer VI (Fig. 6b).

Comparisons of deep learning based mappings to the GLI profile approach. Third level filter activations are related to cortical areas and occurred in deeper layers 13 to 24 in the hOc1 and hOc2 CNNs (except for network layer 15 of the hOc2 CNN). In the hOc1 CNN, 123 of the third level filter activations showed clear cut activations labelling the extent of area hOc1, while ten filter activations showed consistent activations to the cortex surrounding area hOc1. The hOc2 CNN contained 41 third level filter activations labelling the extent of area hOc2, while 7 activations marked the surrounding cortex. When comparing the third level filter activations to the validation section, resemblances to the border position defined by the GLI profile approach become visible (Fig. 7). The superimpositions of two contrasting third level filter activations of the hOc1 and hOc2 CNNs are shown in Fig. 7a,c together with magnified images of the filter activations' outer boundaries. Combined superimpositions of the filter activations show resemblances to the border positions defined by the GLI profile approach. In general, third level filter activations appeared more clear-cut in the hOc1 CNN than in the hOc2 CNN.

Prediction precision. The two CNNs recognized areas hOc1 and hOc2 on all 119 unseen sections in-between the two training sections of the BigBrain dataset²⁵. The predictions were anatomically plausible with regards to topography and neighbouring cortical areas¹⁴. Figure 8 shows that the pixel-wise predictions for cortical area hOc1 and hOc2 resemble the reference labels on the training sections. Single patches of falsely predicted

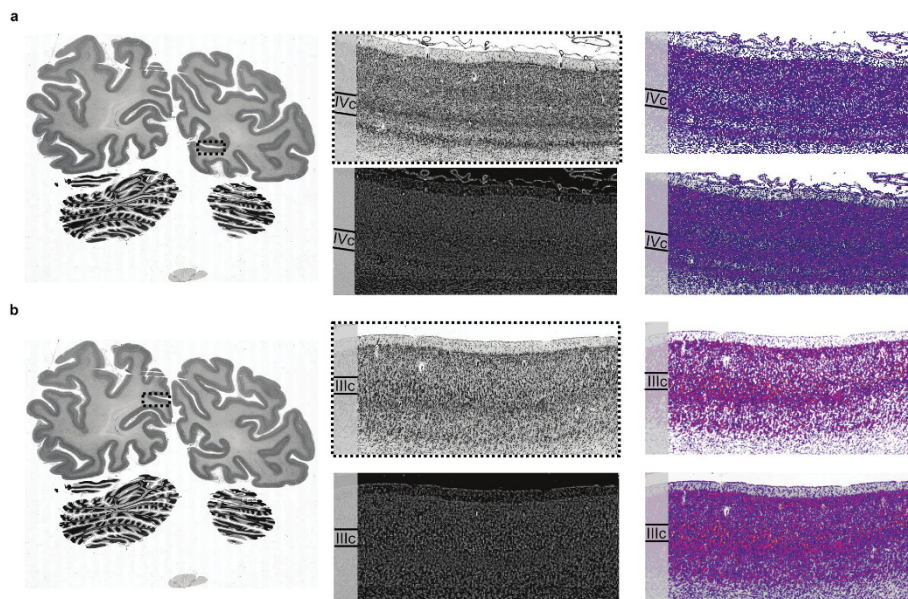


Figure 5. First level filter activations from network layer four of the hOc1 (a) and network layer one of the hOc2 CNN (b). The images on the left show the region of interest on the validation section (section 1021). The four images in the middle and right show microscopically magnified regions of interest of cortical area hOc1 (a) and hOc2 (b) depicted by dashed lines on the section on the left. In the middle, magnified histological cell-body stained images of the regions are displayed over the corresponding GLI images. Images on the right show the magnified characteristic filter activations (upper images) superimposed on cell-body stained images (lower images). Cortical sublayers with notable first level cytoarchitectonic features that are visible in the filter activations and the GLI images are marked by roman numerals.

pixels occurred, but were not connected to the accumulation of correctly predicted pixels that reflect cortical areas hOc1 and hOc2.

Discussion

Cytoarchitectonic brain mapping has repeatedly profited from milestone achievements in computerized image analysis in the last 30 years^{19, 21, 25, 47}. Deep learning-based approaches have the potential to build workflows with a higher degree of automatization and hence increase the limited throughput of these techniques while at the same time providing independent verification of mapping results. Yet, profound insights in how far such techniques operate on criteria that resemble cytoarchitectonic features used by human experts are still lacking. This motivated the present study of deep CNNs, in which we investigated the learned network features for reflected cytoarchitectonic features and compared the internal network structure to statistical image properties used by the current GLI profile approach.

Our analysis confirmed that cytoarchitectonic features are indeed reflected in the internal structure of the deep CNNs and characterize different levels of organization, from cells to their arrangement in cortical layers, and entire cortical areas. Interestingly, the networks seemed to be more sensitive to capture the horizontal cortical organization in layers and sublayers, while the vertical arrangement in columnar structures did not seem to play a role. They inherently incorporate the interdependencies among the three types of features of cortical cytoarchitecture by representing their increasing complexity in an orderly manner from more superficial to deeper network layers. This is most likely due to the hierarchical structure of the convolutional network architecture, reflecting more and more complex features in deeper network layers.

A closer look on these representations revealed the existence of different subsets of filter activations depending on the cortical area. The hOc1 CNN for example contained only one set of filter activations that responded to cell-dense cortical layers on intermediate network layers. Area hOc1 receives massive input from the lateral geniculate nucleus of the thalamus, resulting in a very broad and cell-dense sublayer IVc¹⁰. In contrast layer V is cell-sparse (Fig. 1). These unique cytoarchitectonic features may have led the hOc1 CNN to develop a single

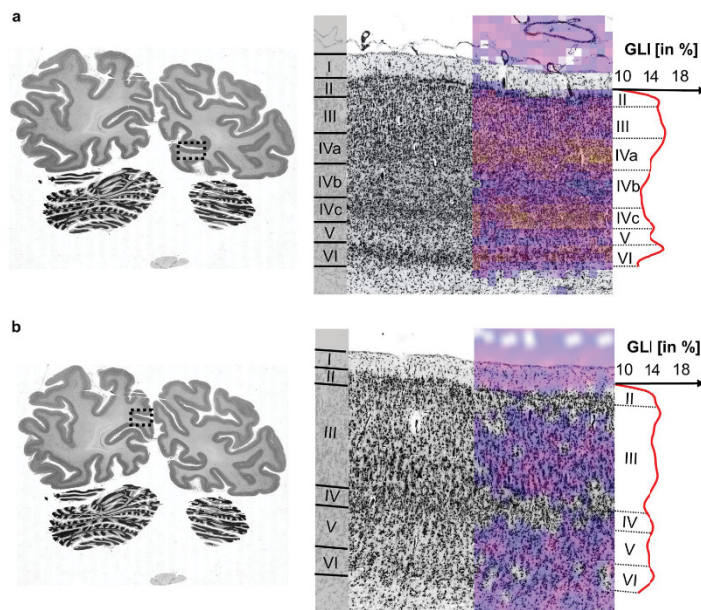


Figure 6. Second level filter activations from network layer 5 of the hOc1 (a) and network layer eight of the hOc2 (b) CNN. Big images on the right show the microscopically magnified regions of interest for cortical area hOc1 (a) and hOc2 (b) depicted by boxes on the left images (section 1021). They display cell-body stained histological images with the corresponding GLI profiles generated at this position. Roman numerals I to VI indicate cortical layers. Arabic letters indicate cortical sublayers. Superimposed characteristic filter activations show specific activations to cell-dense cortical layers of cortical area hOc1 (a) and cell-sparse cortical layers of cortical area hOc2 (b).

set of filter activations that resembles cell-dense cortical layers. Similarly, the hOc2 CNN contains a feature set for cell-dense cortical layers as well. This is not surprising, since a prominent cortical layer IV (although not subdivided into sublayers) constitutes an important cytoarchitectonic feature of area hOc2 as well. Furthermore, layer IV helps to distinguish area hOc2 from area hOc3v which follows ventrally^{16,17}. On the other hand, the hOc2 CNN contains one additional set of filter activations resembling cell-sparse cortical layers on intermediate network layers. The development of such a second set for cell-sparse cortical layers III and V stresses the reflection of cytoarchitectonic features in the hOc2 CNN in two ways alike. First, the clarity of the columnar patterns increases between cortical area hOc1 and hOc2¹⁶ and represents a cytoarchitectonic feature for differentiating the adjacent ventrally and dorsally located areas^{17,19}. Since the columnar arrangement can mainly be observed in cortical layers III, V and VI¹⁰, a feature set for the cell-sparse layers III and V may help to incorporate this information. Secondly, the need for a second set is also underlined by the marked cell sparseness of cortical layer V compared to the ventrally adjoining area and the lack of big pyramidal cells in cortical layer V compared to the dorsally adjoining area. These adjacent areas also show a diminished increase in cell-size in cortical layer III¹⁷ and a lower cell-density in the upper part of cortical layer III¹⁹. In general, these observations support the notion that the CNNs are capable to capture distinct cytoarchitectonic features of cortical areas. They seem to be able to develop distinct representations of traditional cytoarchitectonic features on the cellular and laminar level of cortical areas.

In addition to the representations of traditional cytoarchitectonic features, the deep CNNs revealed correspondences to statistical image properties of the GLI profile approach. These include detailed correspondences between filter activations and GLI profile shapes, which constitute the essential measurement of the GLI profile approach. In addition, filter activations of the deep CNNs also correspond to cell-related features, whereas the GLI profile approach mostly focuses on laminar differences in the cellular pattern. This potentially enables the CNNs to encompass information about the columnar arrangement of cell bodies which constitutes an important cytoarchitectonic feature¹⁰. Filter activations from deeper network layers even reveal the possibility for the CNNs to have access to border positions as defined by the GLI profile approach (Fig. 7). These comparisons reveal that

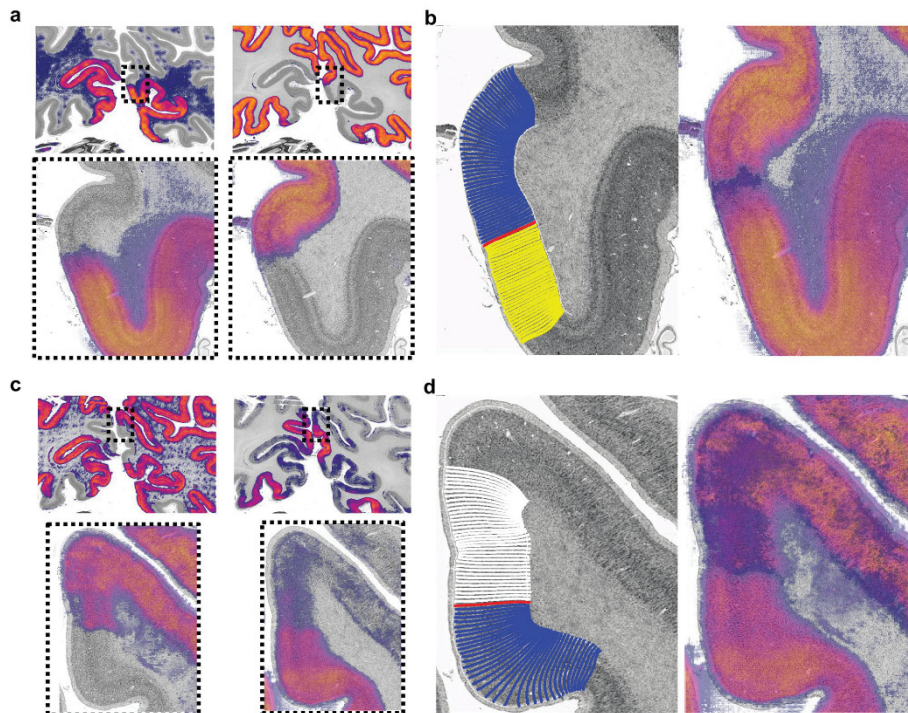


Figure 7. Third level filter activations of the hOc1 (a,b) and hOc2 (c,d) CNN. Images in (a) and (c) show two contrasting third level filter activations from network layer 23 of the hOc1 (a) and hOc2 (c) CNNs on the validation section (section 1021). The images in (b) and (d) compare the border detection result of the GLI profile approach (left) with the combined overlays of the two contrasting third level filter activations (right).

the learned internal feature representations of the CNNs compare well to the descriptive GLI profile shapes as well as to statistically defined borders of the GLI profile approach. Such correspondences to a well-established method provide further evidence for the CNNs' potential in cytoarchitectonic brain mapping approaches.

While the two approaches show many correspondences, they do not share the same data basis. The deep CNNs operate directly on image patches extracted from cell-body stained sections. The GLI profile approach on the other hand, operates on GLI images, which estimate the volume fraction of cell bodies in small measuring fields of 20×20 microns by thresholding the original image intensities and summarizing foreground pixels in each field resulting in a lower dimensional image. For this reason, both approaches are likely to deal with locally restricted changes of cytoarchitecture differently. Here, such locally restricted cytoarchitectonic phenomena can be found in transition regions at the border of cortical area hOc1 and hOc2. These transitions regions have previously been described in myeloarchitectonic works as *border tuft* ("i.e. Grenzbüschel") and *fringe area* "i.e. Randsaum"^{16,48,49}. Right at the beginning of area hOc2, close to the border, the *border tuft* region hosts a distinct set of large pyramidal cells^{16,49} in layer III, accompanied by a very cell-sparse cortical layer V^{16,49}. On the other side of the border, in area hOc1, the *fringe area* is cytoarchitectonically characterized by increased cell densities in cortical layers IVb, V and VI^{16,49}. Additionally, cell sizes in cortical layer III of area hOc2 alternate^{10,16,49}. These complex changes at a cytoarchitectonic border¹¹ may explain the slight shifts of the assumed internal border representations within the CNNs (Fig. 7). Slight activations to the background and white matter in some of the filter activations may originate from different parameter sensitivities of the CNNs in comparison to the GLI profile approach. A comparison of both approaches should be considered with care therefore, although the deep CNNs seemingly incorporate traditional cytoarchitectonic features.

A deep understanding of internal network structure is mandatory to accept deep learning-based brain mapping as a valid support in future cytoarchitectonic mapping approaches. The present study provides first arguments for introducing deep learning-based brain mapping on a routine basis. First of all, it enables a direct assessment of incorporated cytoarchitectonic features via filter activation analysis. This constitutes an advantage

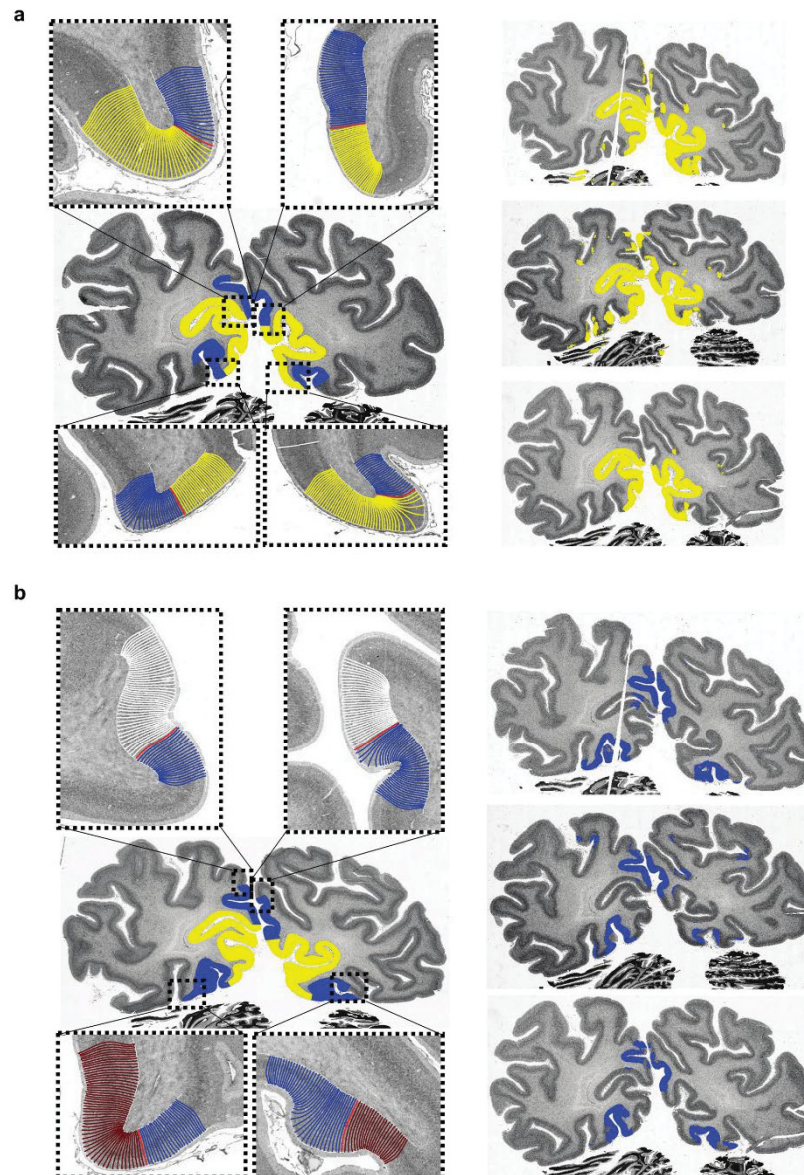


Figure 8. Segmentations of the hOc1 (a) and hOc2 (b) CNNs on three sections of the BigBrain dataset in comparison to borders detected by the GLI profile approach. Enlarged images of the training section (section 1081) in (a) show borders between cortical areas hOc1 (yellow) and hOc2 (blue). Enlarged images of the training section (section 0961) in (b) show borders between cortical area hOc2 (blue), hOc3d (white) and hOc3v (brown). Borders were detected using the GLI profile approach. The segmentations on three of the 119 sections (section 0991, 1036, 1066 from top to bottom) in-between the training sections are shown on the right in (a) for cortical area hOc1 (yellow) and in (b) for cortical area hOc2 (blue) for a comparison.

in comparison to the feature vector of the GLI profile approach. Secondly, the analysis of the internal structure also revealed different spatial resolutions from cell-related to cortical layer-related to area-related features. This is especially important to capture the multi-scale organization of the cortex⁴¹—a circumstance that the current GLI profile approach does not mimic. It captures different spatial resolutions only indirectly in the direction of cortical columns by incorporating central moments like the mean and skewness in a profile shape's feature vector.

A disadvantage is that the segmentation performance cannot be explained by the reflected cytoarchitectonic features per se. In fact, although highly improbable, the internal features that we identified to resemble cytoarchitectonic principles might not contribute to the final segmentation result at all. However, the resemblances of cytoarchitectonic principles is not a necessary nor a sufficient condition for successfully segmenting cortical areas. Several studies have been published in the past that were based on mathematical descriptions that were rather abstract, or tuned to detect architectonic gradients rather than to characterize the architecture itself. This resulted in reproducible and testable descriptions of borders without resembling traditional architectonic features directly^{22,27,50}. The here applied CNNs are interesting in so far, as they reproduce what experts see to a certain degree, which introduces another level of confidence. It is possible that the CNNs may have developed non-intuitive features representing other (yet) unknown aspects of cortical cytoarchitecture. Such relationships have to be systematically studied in more detail in the future. Future advances in explainable image segmentation networks might allow us to assess the relevance of individual features for the actual segmentation outputs in a more reliable fashion. Additionally, analyses of more cortical regions with distinct cytoarchitectonic features would help to solve the question in how far the features detected by the hOc1 and hOc2 CNNs can be generalized to other areas, e.g., motor and higher association areas, or allocortical areas which contain a different number of cortical layers. This would go beyond the scope of this work, and remains a project of future research.

However, the amount of filter activations reflecting cytoarchitectonic features and the existence of different subsets suggests that deep learning with convolutional networks is able to capture cytoarchitectonic features. This is especially the case for cortical layer information. Such information is worth considering for future improvements of the deep learning approach. One possible option in this case is the explicit inclusion of information about laminar surfaces itself, which have recently been published for the BigBrain dataset^{41,52}. Other incorporations of prior information, such as feeding in projected probabilistic maps³⁷ or pre-training with an auxiliary task³⁸ have already shown to improve the performance. Following this line, the present analysis gives valuable insights for such future considerations and provides strong evidence that deep convolutional networks are valid and suitable tools for high-throughput mapping workflows.

Data availability

The datasets generated and analysed during the current study are available in the EBRAINS repository [<https://kg.ebrains.eu/search/instances/Dataset/78801754-16c1-4df2-9b2e-1b10c28a10c2>].

Received: 25 June 2020; Accepted: 27 November 2020

Published online: 16 December 2020

References

- Liu, J. & Zhao, G. In *2018 International Joint Conference on Neural Networks (IJCNN). 2018 Proceedings* (IEEE, Piscataway, NJ, 2018), pp. 1–8.
- Nayebi, A. *et al.* Task-Driven Convolutional Recurrent Models of the Visual System. <http://arxiv.org/pdf/1807.00053v1> (2018).
- Kabrisky, M. *A Proposed Model for Visual Information Processing in the Human Brain* (University of Illinois Press, Urbana, 1966).
- Fukushima, K. Cognitron: a self-organizing multilayered neural network. *Biol. Cybern.* **20**, 121–136. <https://doi.org/10.1007/BF00342633> (1975).
- Shai, A. & Larkum, M. E. Deep learning. Branching into brains. *eLife Sci.* **6**, e33066. <https://doi.org/10.7554/eLife.33066> (2017).
- Guerguev, I., Lillcrap, T. P. & Richards, B. A. Towards deep learning with segregated dendrites. *eLife Sci.* **6**, e22901. <https://doi.org/10.7554/eLife.22901> (2017).
- Stanley, K. O., Clune, J., Lehman, J. & Miikkulainen, R. Designing neural networks through neuroevolution. *Nat. Mach. Intell.* **1**, 24. <https://doi.org/10.1038/s42256-018-0006-z> (2019).
- Rudin, C. Stop explaining black box machine learning models for high stakes decisions and use interpretable models instead. *Nat. Mach. Intell.* **1**, 206–215. <https://doi.org/10.1038/s42256-019-0048-x> (2019).
- Samek, W., Wiegand, T. & Müller, K.-R. Explainable Artificial Intelligence: Understanding, Visualizing and Interpreting Deep Learning Models (2017).
- von Economo, C. E. & Koskinas, G. N. *Die Cytoarchitektur der Hirnrinde des erwachsenen Menschen* (Springer, Berlin, 1925).
- Amunts, K. & Zilles, K. Architectonic mapping of the human brain beyond Brodmann. *Neuron* **88**, 1086–1107. <https://doi.org/10.1016/j.neuron.2015.12.001> (2015).
- Goulas, A., Zilles, K. & Hilgetag, C. C. Cortical gradients and laminar projections in mammals. *Trends Neurosci.* **41**, 775–788. <https://doi.org/10.1016/j.tins.2018.06.003> (2018).
- Meynert, T. *Der Bau der Gross-Hirnrinde und seine örtlichen Verschiedenheiten, nebst einem pathologisch-anatomischen Corollarium* (Heuser, Louisville, 1872).
- Brodmann, K. *Vergleichende Lokalisationslehre der Grosshirnrinde in ihren Prinzipien dargestellt aufgrund des Zellenbaues* (Barth, Leipzig, 1909).
- Vogt, C. & Vogt, O. *Allgemeine Ergebnisse unserer Hirnforschung* (J.A. Barth, Leipzig, 1919).
- Amunts, K., Malikovic, A., Mohlberg, H., Schormann, T. & Zilles, K. Brodmann's areas 17 and 18 brought into stereotaxic space—where and how variable? *NeuroImage* **11**, 66–84. <https://doi.org/10.1006/nimg.1999.0516> (2000).
- Rottschy, C. *et al.* Ventral visual cortex in humans. Cytoarchitectonic mapping of two extrastriate areas. *Hum. Brain Map.* **28**, 1045–1059. <https://doi.org/10.1002/hbm.20340> (2007).
- van Essen, D. C., Anderson, C. H. & Felleman, D. J. Information processing in the primate visual system: an integrated systems perspective. *Science* **255**, 419–423. <https://doi.org/10.1126/science.1734518> (1992).
- Schleicher, A., Amunts, K., Geyer, S., Morosan, P. & Zilles, K. Observer-independent method for microstructural parcellation of cerebral cortex. A quantitative approach to cytoarchitectonics. *NeuroImage* **9**, 165–177. <https://doi.org/10.1006/nimg.1998.0385> (1999).

20. Schleicher, A. *et al.* Quantitative architectural analysis. A new approach to cortical mapping. *Anat. Embryol.* **210**, 373–386. <https://doi.org/10.1007/s00429-005-0028-2> (2005).
21. Zilles, K., Schleicher, A., Palomero-Gallagher, N. & Amunts, K. in *Brain mapping. The methods*, edited by I. C. Mazziotta & A. W. Toga (Academic Press, Amsterdam, 2002), Vol. 2, pp. 573–602.
22. Schmitt, O., Hömke, L. & Dümbsen, L. Detection of cortical transition regions utilizing statistical analyses of excess masses. *NeuroImage* **19**, 42–63. [https://doi.org/10.1016/S1053-8119\(03\)00040-5](https://doi.org/10.1016/S1053-8119(03)00040-5) (2003).
23. Schleicher, A. *et al.* A stereological approach to human cortical architecture: identification and delineation of cortical areas. *J. Chem. Neuroanat.* **20**, 31–47. [https://doi.org/10.1016/S0891-0618\(00\)00076-4](https://doi.org/10.1016/S0891-0618(00)00076-4) (2000).
24. Zilles, K. & Amunts, K. Centenary of Brodmann's map—conception and fate. *Nat. Rev. Neurosci.* **11**, 139–145. <https://doi.org/10.1038/nrn2776> (2010).
25. Amunts, K., Schleicher, A. & Zilles, K. Cytoarchitecture of the cerebral cortex—more than localization. *NeuroImage* **37**, 1061–1065. <https://doi.org/10.1016/j.neuroimage.2007.02.037> (2007).
26. Amunts, K., Mohlberg, H., Blaudau, S. & Zilles, K. Julich-Brain: a 3D probabilistic atlas of the human brain's cytoarchitecture. *Science* **369**, 988–992 (2020).
27. Annessi, J., Pitiot, A., Dinov, I. D. & Toga, A. W. A myelo-architectonic method for the structural classification of cortical areas. *NeuroImage* **21**, 15–26. <https://doi.org/10.1016/j.neuroimage.2003.08.024> (2004).
28. Amunts, K. *et al.* BigBrain. An ultrahigh-resolution 3D human brain model. *Science* **340**, 1472–1475. <https://doi.org/10.1126/science.1235381> (2013).
29. Shen, D., Wu, G. & Suk, H.-I. Deep learning in medical image analysis. *Ann. Rev. Biomed. Eng.* **19**, 221–248. <https://doi.org/10.1146/annurev-bioeng-071516-044442> (2017).
30. Komura, D. & Ishikawa, S. Machine learning methods for histopathological image analysis. *Comput. Struct. Biotechnol. J.* **16**, 34–42. <https://doi.org/10.1016/j.csbj.2018.01.001> (2018).
31. Xing, F. & Yang, L. Robust nucleus/cell detection and segmentation in digital pathology and microscopy images: a comprehensive review. *IEEE Rev. Biomed. Eng.* **9**, 234–263. <https://doi.org/10.1109/RBME.2016.2515127> (2016).
32. Madabhushi, A. & Lee, G. Image analysis and machine learning in digital pathology: challenges and opportunities. *Med. Image Anal.* **33**, 170–175. <https://doi.org/10.1016/j.media.2016.06.037> (2016).
33. Litjens, G. *et al.* A survey on deep learning in medical image analysis. *Med. Image Anal.* **42**, 60–88. <https://doi.org/10.1016/j.media.2017.07.005> (2017).
34. Ronneberger, O., Fischer, P. & Brox, T. in *Medical Image Computing and Computer-Assisted Intervention – MICCAI 2015. 18th International Conference, Munich, Germany, October 5–9, 2015, Proceedings, Part III*, edited by N. Navab, I. Hornegger & W. M. Wells (Springer International Publishing, Cham, 2015), Vol. 1, pp. 234–241.
35. Akram, S. U., Kannala, J., Eklund, L. & Heikkilä, J. in *Deep Learning and Data Labeling for Medical Applications. First International Workshop, LABELS 2016, and Second International Workshop, DLMLA 2016, Held in Conjunction with MICCAI 2016, Athens, Greece, October 21, 2016, Proceedings*, edited by G. Carneiro, *et al.* (Springer International Publishing, Cham, 2016), pp. 21–29.
36. Song, Y. *et al.* Accurate cervical cell segmentation from overlapping clumps in pap smear images. *IEEE Trans. Med. Imag.* **36**, 288–300. <https://doi.org/10.1109/TMI.2016.2606380> (2017).
37. Spitzer, H., Amunts, K., Harmeling, S. & Dickscheid, T. in *2017 IEEE 14th International Symposium on Biomedical Imaging (ISBI 2017). From Nano to Macro : Tuesday, 18 April-Friday, 21 April 2017, Melbourne Convention and Exhibition Centre, Melbourne, Australia (IEEE, Piscataway, NJ, 2017)*, pp. 920–923.
38. Spitzer, H., Kivitz, K., Amunts, K., Harmeling, S. & Dickscheid, T. in *Medical image computing and computer assisted intervention – MICCAI 2018*, edited by A. F. Frangi, J. A. Schnabel, C. Davatzikos, C. Alberola-López & G. Fichtinger (Springer, Cham, 2018), pp. 663–671.
39. Kujovic, M. *et al.* Cytoarchitectonic mapping of the human dorsal extrastriate cortex. *Brain Struct. Funct.* **218**, 157–172. <https://doi.org/10.1007/s00429-012-0390-9> (2013).
40. Schiffer, C. *et al.* Convolutional neural networks for efficient mapping of cytoarchitectonic areas across full stacks of histological human brain sections. Preprint at <https://arxiv.org/abs/2011.12857> (2020).
41. Fournier, M., Lewis, L. B. & Evans, A. C. in *Medical computer vision and Bayesian and graphical models for biomedical imaging. MICCAI 2016 International Workshops, MCV and BAMB, Athens, Greece, October 21, 2016, Revised selected papers*, edited by H. Müller, *et al.* (Springer, Cham, Switzerland, 2017), pp. 14–25.
42. Oquab, M., Bottou, L., Laptev, I. & Sivic, J. in *2014 IEEE Conference on Computer Vision and Pattern Recognition (CVPR 2014) (IEEE, Piscataway, NJ, 2014)*, pp. 1717–1724.
43. Viola, P. & Wells, W. M. III. Alignment by maximization of mutual information. *Int. J. Comput. Vis.* **24**, 137–154. <https://doi.org/10.1023/A:1007958904918> (1997).
44. Pluim, J. P. W., Maintz, J. B. A. & Viergever, M. A. Mutual-information-based registration of medical images: a survey. *IEEE Trans. Med. Imaging* **22**, 986–1004 (2003).
45. The Matplotlib development team. *Perceptually Uniform Sequential Colormaps* (The Matplotlib development team, 2019).
46. Neuroanatomy Applied & Theoretical (NAAT). *MicroDraw* (Neuroanatomy Applied & Theoretical (NAAT), 2019).
47. Schleicher, A., Morosan, P., Amunts, K. & Zilles, K. Quantitative architectural analysis: a new approach to cortical mapping. *J. Autism Dev. Disorders* **39**, 1568. <https://doi.org/10.1007/s10803-009-0790-8> (2009).
48. Sanides, F. & Vitzthum, H. G. Zur Architektur der menschlichen Sehrinde und den Prinzipien ihrer Entwicklung. *Deutsche Zeitschrift f. Neuroheilkunde* **187**, 680–707. <https://doi.org/10.1007/BF00243937> (1965).
49. Sanides, F. & Vitzthum, H. G. Die Grenzerscheinungen am Rande der menschlichen Sehrinde. *Deutsche Zeitschrift f. Neuroheilkunde* **187**, 708–719. <https://doi.org/10.1007/BF00243938> (1965).
50. Schmitt, O. & Böhme, M. A robust transcortical profile scanner for generating 2-d traverses in histological sections of richly curved cortical courses. *NeuroImage* **16**, 1103–1119. <https://doi.org/10.1006/nimg.2002.1159> (2002).
51. Wagstyl, K. *et al.* Mapping cortical laminar structure in the 3D BigBrain. *Cereb. Cortex* **28**, 2551–2562. <https://doi.org/10.1093/cercor/bhy074> (2018).
52. Wagstyl, K. *et al.* Automated segmentation of cortical layers in BigBrain reveals divergent cortical and laminar thickness gradients in sensory and motor cortices. *bioRxiv* <https://doi.org/10.1101/580597> (2019).
53. Hubel, D. H. & Wiesel, T. N. Laminar and columnar distribution of geniculocortical fibers in the macaque monkey. *J. Comp. Neurol.* **146**, 421–450. <https://doi.org/10.1002/cne.901460402> (1972).
54. Wandell, B. A., Dumoulin, S. O. & Brewer, A. A. Visual field maps in human cortex. *Neuron* **56**, 366–383. <https://doi.org/10.1016/j.neuron.2007.10.012> (2007).
55. Wang, L., Mruczek, R. E. B., Arcaro, M. J. & Kastner, S. Probabilistic maps of visual topography in human cortex. *Cerebral Cortex* **25**, 3911–3931. <https://doi.org/10.1093/cercor/bhu277> (2015).
56. Zeki, S. M. Functional specialisation in the visual cortex of the rhesus monkey. *Nature* **274**, 423–428. <https://doi.org/10.1038/274423a0> (1978).
57. van Essen, D. C., Newsome, W. T. & Maunsell, J. H. The visual field representation in striate cortex of the macaque monkey. Asymmetries, anisotropies, and individual variability. *Vis. Res.* **24**, 429–448. [https://doi.org/10.1016/0042-6989\(84\)90041-5](https://doi.org/10.1016/0042-6989(84)90041-5) (1984).
58. Hubel, D. H. & Wiesel, T. N. Receptive fields of single neurons in the cat's striate cortex. *J. Physiol.* **148**, 574–591. <https://doi.org/10.1113/jphysiol.1959.sp006308> (1959).

59. Hubel, D. H. & Wiesel, T. N. receptive fields and functional architecture in two nonstriate visual areas (18 and 19) of the cat. *J. Neurophysiol.* **28**, 229–289. <https://doi.org/10.1152/jn.1965.28.2.229> (1965).
60. Ts'o, D. Y., Zarella, M. & Burkitt, G. Whither the hypercolumn?. *J. Physiol.* **587**, 2791–2805. <https://doi.org/10.1113/jphysiol.2009.171082> (2009).
61. Hubel, D. H. & Wiesel, T. N. Cortical and callosal connections concerned with the vertical meridian of visual fields in the cat. *J. Neurophysiol.* **30**, 1561–1573 (1967).
62. Myers, R. E. Commissural connections between occipital lobes of the monkey. *J. Comp. Neurol.* **118**, 1–16. <https://doi.org/10.1002/cne.901180102> (1962).
63. Zeki, S. M. Interhemispheric connections of prestriate cortex in monkey. *Brain Res.* **19**, 63–75. [https://doi.org/10.1016/0006-8993\(70\)90237-4](https://doi.org/10.1016/0006-8993(70)90237-4) (1970).
64. Clarke, S. & Miklosy, J. Occipital cortex in man. Organization of callosal connections, related myelo- and cytoarchitecture, and putative boundaries of functional visual areas. *J. Comp. Neurol.* **298**, 188–214. <https://doi.org/10.1002/cne.902980205> (1990).

Acknowledgements

This research received funding from the European Union's Horizon 2020 Framework Programme for Research and Innovation under the Specific Grant Agreement Numbers 720270 (Human Brain Project SGA1), 785907 (Human Brain Project SGA2) and 945539 (Human Brain Project SGA3). The work was further supported by the German Federal Ministry of Education and Research (BMBF) and the Max Planck Society for the Advancement of Science through their joint initiative between German Universities and German Research Organizations. Computing time was granted through JARA-HPC on the supercomputer JURECA at Jülich Supercomputing Centre (JSC).

Author contributions

K.K. proposed the concept for the manuscript, conducted the data analyses, interpreted the results, and wrote the manuscript. C.S. contributed to the concept of the manuscript, trained the neural networks and processed the data. H.S. developed initial versions of the neural network architecture and provided initial weights for neural network models trained in this work. T.D. provided crucial advice for quantitative data analysis of filter activations. K.A. contributed to the concept of the manuscript and provided advice on how to sharpen the scope of the manuscript with particular focus on current cytoarchitectonic analysis approaches. All authors critically revised the manuscript and provided their final approval to publish the work.

Funding

Open Access funding enabled and organized by Projekt DEAL.

Competing interests


The authors declare no competing interests.

Additional information

Correspondence and requests for materials should be addressed to K.K.

Reprints and permissions information is available at www.nature.com/reprints.

Publisher's note Springer Nature remains neutral with regard to jurisdictional claims in published maps and institutional affiliations.

 **Open Access** This article is licensed under a Creative Commons Attribution 4.0 International License, which permits use, sharing, adaptation, distribution and reproduction in any medium or format, as long as you give appropriate credit to the original author(s) and the source, provide a link to the Creative Commons licence, and indicate if changes were made. The images or other third party material in this article are included in the article's Creative Commons licence, unless indicated otherwise in a credit line to the material. If material is not included in the article's Creative Commons licence and your intended use is not permitted by statutory regulation or exceeds the permitted use, you will need to obtain permission directly from the copyright holder. To view a copy of this licence, visit <http://creativecommons.org/licenses/by/4.0/>.

© The Author(s) 2020

4 Discussion

The revised deep-learning based approach was able to generate accurate high-quality cortical and subcortical maps in the BigBrain. An analysis of the internal structure including a comparison to the profile-based approach provided further arguments for the validity of the approach. Our analyses therefore provide a first use-case demonstrating the potential of the revised deep-learning approach for cytoarchitectonic mapping in large series of sections in the BigBrain on a routine basis.

4.1 Accuracy and Quality of Deep-Learning Based Brain Mapping

First evidence for the accuracy of the revised deep-learning approach in the BigBrain is provided by Study 1. Herein, the methodology was able to reliably detect four cortical areas of the visual system, i.e. the primary visual cortex, area hOc1 (Amunts et al., 2000), the secondary visual cortex, hOc2 (Amunts et al., 2000), as well as higher visual areas hO3v (Rottschy et al., 2007) and hOc5 (Malikovic et al., 2007) on a large number of serial sections with high accuracy and consistency (Schiffer et al., 2021). Detected borders obtained by the current profile-based mapping approach corresponded well to the segmentations of the revised deep-learning approach (Kiwitz et al., 2020; Schiffer et al., 2021). At the same time, 3D volume and surface reconstructions of visual cortical areas hOc1, hOc2 and hOc5 matched previous reference values based on multiple brains (Amunts et al., 2007) – emphasizing the high quality of the maps (Schiffer et al., 2021). On top of that, the 3D-reconstructions were more anatomically consistent than interpolating 2D maps generated with the profile-based approach while the necessary manual annotation effort was the same (Schiffer et al., 2021).

The revised deep-learning approach was also able to increase the accuracy of the maps in comparison to earlier deep-learning implementations (Spitzer et al., 2018; Spitzer et al., 2017). The results now show anatomically plausible segmentations of the primary and secondary visual cortex with outlines corresponding to significant borders as detected by the current profile-based approach (**Figure 3**). Incorrectly segmented pixels mostly appeared at cortical

regions with a highly oblique cutting angle (Schiffer et al., 2021) – a limitation that is shared with the profile-based approach (Schleicher et al., 1999).

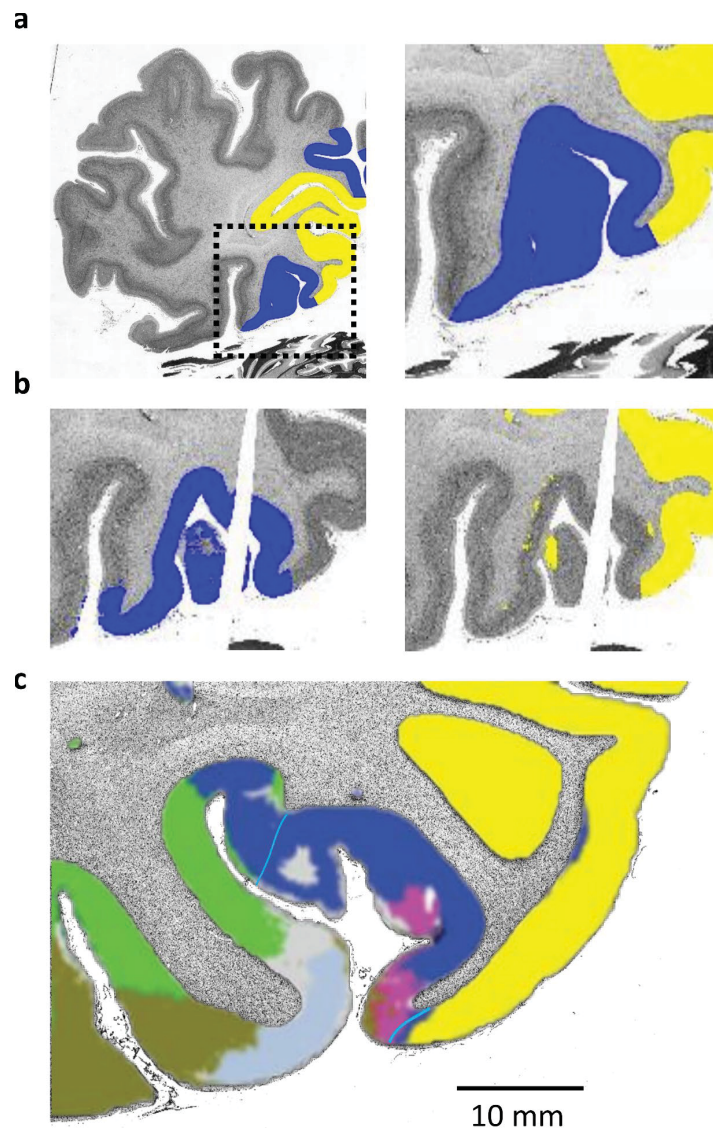


Figure 3: Accuracy of the revised deep-learning approach . The images in (a) show cortical maps of the primary (yellow) and secondary (blue) visual cortex on section 0961 of the BigBrain dataset generated using the profile-based approach. The dashed box indicates the magnified crop of the border region on the right. Images in (b) show the respective maps generated by the revised-deep-learning based approach on an adjacent section (section 0991) with matching area outlines (adapted and modified after Kiwitz et al. (2020)). Note that the slight shifts in outline are caused by the more rostral sectioning position in comparison to a). (c) shows an excerpt from **Figure 2** demonstrating the segmentation performance of an earlier deep-learning implementation for cytoarchitectonic mapping (adapted and modified with permission from Spitzer et al. (2017) © 2017 IEEE) with cortical borders defined by the profile-based approach depicted in cyan.

An extension of the use of the revised deep-learning approach to assess its applicability and quality regarding subcortical areas in Study 2 revealed similar results. Here, the revised deep-learning approach generated high-quality maps of the three subdivisions of the human MGB (Kiwitz et al., 2022). The maps follow previous microscopic analyses of cytoarchitectonic features of the MGB subdivisions (Winer, 1984) and resemble histological maps (**Figure 4**) of Morel (2007) and Ding et al. (2016). The illustration of the BigBrain MGB maps in **Figure 4** was chosen to approximately match the sectioning position of the illustrations adapted from Morel (2007) and Ding et al. (2016).

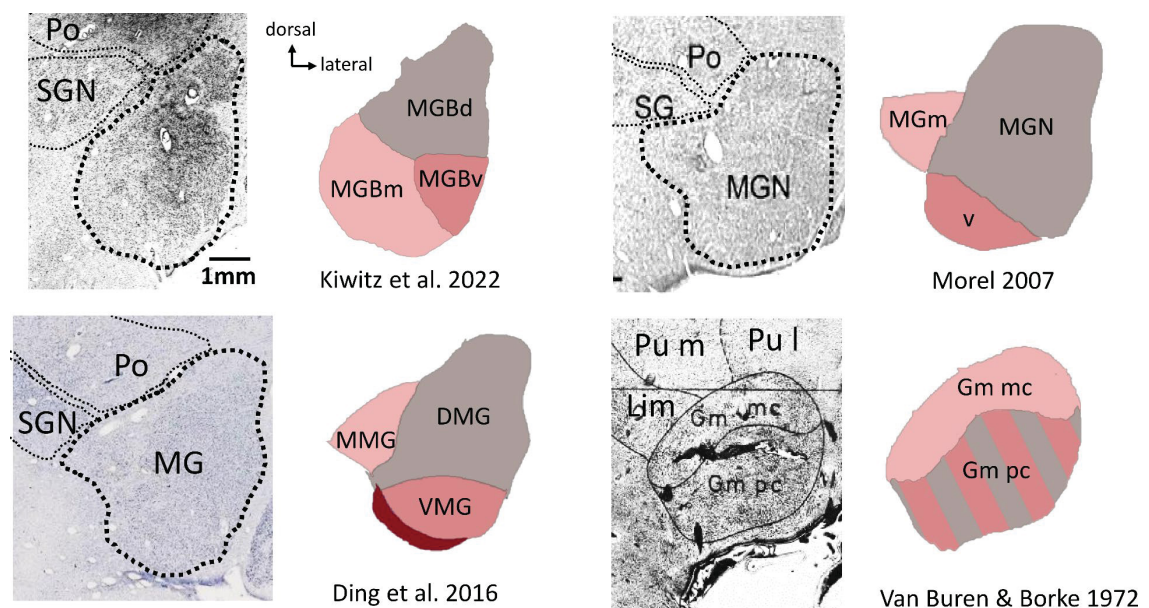


Figure 4. Subdivisions of the BigBrain MGB in comparison to previous histological maps. Four schematic illustrations of the MGB are shown alongside histologically cell-stained images from previous works. The nomenclature follows the original works with MGB (medial geniculate body), MGN (medial geniculate nucleus), MG (medial geniculate) and Gm (Geniculatum mediale) being equivalent in meaning. The maps of Morel (Morel (2007), reproduced with permission of The Licensor through PLSclear), Ding et al. (adapted and modified with permission from Ding et al. (2016) © 2016 WILEY) and van Buren & Borke (adapted and modified with permission from van Buren and Borke (1972) © 1972 Springer) have been re-colored to match the color scheme of the BigBrain MGB map (section 3282) of Kiwitz et al. (2022). Same-colored subdivisions show cytoarchitectonically equivalent subdivisions. The tripartism of the BigBrain MGB follows Morel (2007) and Ding et al. (2016) except for the limitans nucleus (dark red) previously described by Hassler (1959) mostly based on fiber stainings. The map of van Buren and Borke (1972) is representative for early works dividing the MGB into a parvocellular (pc) and magnocellular (mc) division (Clark, 1933). The striped pc division in illustrates the subdivision into a dorsal and a ventral part (Hassler, 1959). Note that the MGB BigBrain map has been mirrored to match the other left-hemispheric illustrations. The cell-body stained images have been edited to ensure a similar image contrast.

The topography of the dorsal subdivision is similar across the maps and unambiguously characterizes the dorsal subdivisions as a cap of the MGB (**Figure 4**). The size and topography of the medial and ventral subdivisions differs across the maps with an increased lateral expansion of the medial subdivision in the BigBrain (**Figure 4**). Our observations in the BigBrain showed a decrease in size of the ventral subdivision from caudal to more rostral sections accompanied by a lateral shift of the border with the medial subdivision – allowing the medial subdivision to occupy more volume. Despite these differences, our analyses further manifest the ventromedial location of the magnocellular medial subdivision (Mai and Majtanik, 2018), which has previously also been located ventrolaterally (Amunts et al. (2012)).

The BigBrain MGB maps generated using the revised deep-learning based approach provide insight into the topography of the MGB on a full series of histological sections. The three subdivisions of the MGB could be identified on 132 sections of the left and 165 sections of the right hemisphere (Kiwitz et al., 2022), which surpasses the less than 10 visually inspected sections reported by Ding et al. (2016) and Morel (2007). Our maps therefore provide an additional level of confidence regarding the cytoarchitectonic characterization and reliability of the methodological approach. Together with the previously published maps of the LGB layers in the BigBrain (Brandstetter et al., 2021), the MGB maps form a high-resolution reference of the human metathalamus.

All generated cortical and subcortical maps, as well as the associated reference annotations have been made publicly available via the EBRAINS Knowledge Graph (<https://kg.ebrains.eu/>). The high accuracy and quality of the maps provide first evidence for deep-learning based brain mapping to be used as a semi-automatic alternative to map cortical as well as subcortical areas in the BigBrain on a routine basis.

4.2 The Internal Structure of Deep-Learning Based Brain Mapping Approaches

Despite this promising proof-of-principle demonstration it still remained unknown in how far and to what extent the revised deep-learning approach actually operates on criteria that resemble traditional cytoarchitectonic features.

At the same time, it was not clear as to what extent a relation to the current quantitative image analysis of the profile- approach could be established – bringing an evaluation of how the deep-learning approach actually operates into focus.

4.2.1 Resemblances to Traditional Cytoarchitectonic Features

Following this line of thought, Study 3 revealed resemblances of the revised deep-learning approach to cytoarchitectonic features used by neuroanatomists. The resemblances included cellular, laminar as well as whole area related features (Kiwitz et al., 2020). It became apparent that the revised deep-learning approach developed different sets of feature representations depending on which cortical area it was trained to segment. Differences of these subsets especially corresponded to cytoarchitectonic differences on the laminar level. When trained to segment the primary visual cortex, a distinct set of feature representations to cell-dense cortical layers were found. Since the primary visual cortex receives massive input from the LGB, the broad and cell-dense input layer IVc may have caused the developed of such a preference (Kiwitz et al., 2020). In contrast to this, when trained to segment the secondary visual cortex, two distinct sets of feature representations to cell-dense as well as cell-sparse cortical layers appeared. The former stays in accordance to the cell-dense and prominent layer IV of the secondary visual cortex which constitutes an important cytoarchitectonic feature that is used to distinguish it from the adjoining area hOc3v (Amunts et al., 2000; Rottschy et al., 2007). The latter can be explained in two was alike: Firstly, the clarity of the columnar arrangement – mainly visible in the more cell-sparse cortical layers III, V and VI (Economo and Koskinas, 1925; **Figure 1**) - increases between the primary and secondary visual cortex (Amunts et al., 2000). Secondly, the cytoarchitectonic features of the cells sparse cortical layer V constitute an important characteristic to distinguish the secondary visual cortex from the ventrally and dorsally adjoining cortical areas (Kiwitz et al., 2020; Kujovic et al., 2013; Rottschy et al., 2007). The adjacent areas also show a diminished increase in cell-size in cortical layer III (Rottschy et al., 2007) and a lower cell-density in the upper part of cortical layer III (Kujovic et al., 2013) – further emphasizing the importance of the cell-sparse layers as a distinguishing factor for the deep-

learning approach to consider when segmenting the secondary visual cortex. In general, these observations support the notion that the revised deep-learning approach captures traditional cytoarchitectonic features of cortical areas with a special emphasis on cortical layers.

4.2.2 Comparisons to Profile-based Image Analysis

At the same time, the learned internal feature representations compared well to the profile shapes and statistically defined borders of the profile-based approach (Kiwitz et al., 2020). Whereas the profiles mostly reflect the vertical architecture of the cortex in the form of cortical columns along their trajectory from the white matter to the pial surface, the revised deep-learning approach complements this by having developed internal representations of cortical layers in the horizontal direction. Together with the cell-related and area-related feature representations, they form an internal representation of cortical cytoarchitecture at different spatial resolutions - a circumstance that the current profile-based approach does not mimic (Kiwitz et al., 2020). Such a multi-scale representation is of special importance to capture the multi-scale organization of the cortex (Amunts and Zilles, 2015). A further more concrete difference between the two approaches constitutes the possibility to directly assess the incorporated cytoarchitectonic features, which the current profile-based approach is not capable of unambiguously (Schleicher et al., 2000; Schmitt et al., 2003).

When comparing both approaches it should be taken into consideration however, that they operate on different data. While the revised deep-learning approach operates directly on patches of histological sections (Schiffer et al., 2021), the profile-based approach operates on lower dimensional thresholded GLI images (Schleicher et al., 1999; Schleicher and Zilles, 1990; Zilles et al., 2002). It cannot be ruled out that this difference may have an impact on the approaches' performance. A detailed analysis of cortical area-related internal representations of the revised deep-learning approach in Study 3 for example, has shown that assumed internal border representation between the primary and secondary visual cortex is slightly shifted (Kiwitz et al., 2020). The border between the primary and secondary visual cortex hosts various locally

restricted changes of cytoarchitecture in the form of transition areas (Economo and Koskinas, 1925; Sanides and Vitzthum, 1965). Such local peculiarities of cytoarchitecture may have a greater impact on the revised deep-learning approach due to its more direct operation on the histological data. The profile-based approach on the other side may just be too insensitive to detect these local changes in cytoarchitecture. A comparison between both approaches has to be undertaken with care therefore.

An additional limitation results from the inability to link the learned internal cytoarchitectonic feature representations to the actual segmentations. Despite having developed distinct sets of internal feature representations, the revised deep-learning based approach, although highly improbable, may not have used this information at all to produce anatomically plausible segmentations in the end. Other studies have used rather abstract mathematical descriptions to produce reproducible descriptions of borders without representing traditional architectonic features directly (Annese et al., 2004; Schmitt et al., 2003; Schmitt and Böhme, 2002). The direct incorporation of cytoarchitectonic features does not seem to be a necessary nor a sufficient condition for successfully segmenting cortical areas therefore (Kiwitz et al., 2020). Analyzing the internal feature representations of the revised deep-learning based approach provides another level of confidence in so far, as it reproduces what neuroanatomical experts see to a certain degree. The deep-learning approach may have indeed developed additional more non-intuitive features representing other (yet) unknown aspects of cortical cytoarchitecture. Studying such relationships in more detail in the future will allow us to assess the relevance of individual features for the actual segmentation performance in a more reliable fashion (Kiwitz et al., 2020).

However, the sheer abundance of internal cytoarchitectonic feature representations and their nature across different cortical areas suggests that they are advantageous for mapping cytoarchitectonic areas. In combination with the correspondences to the profile-based approach, these insights into the internal structure therefore provide important arguments for the validity of deep-learning based brain mapping.

4.3 Advantages of Deep-Learning Assisted Brain Mapping

4.3.1 *Time Efficiency*

While cytoarchitectonic analyses in cortical mapping studies have benefited significantly from the profile-based approach, recent developments of high-throughput tissue scanners challenge the throughput for future studies. This is especially relevant for the 3D-reconstructed BigBrain dataset with its more than 7400 stained histological sections (Amunts et al., 2013) at 20-micron isotropic resolution. Recent experience of our research group has shown that mapping a cortical area on every section in the BigBrain dataset would require roughly 1 year per area when applying the profile-based approach. Taken together the time for generating reference delineations, computing and quality checks, the revised deep-learning approach narrows down the mapping time of a large cortical area like the primary visual cortex to roughly 1-2 weeks (Schiffer et al., 2021). At the same time the approach is able to handle common mechanical damages like ruptures and tears resulting from histological processing of the tissue that impedes an application of the profile-based approach (Schiffer et al., 2021). This constitutes a major increase in efficiency and enables mapping in full histological series of the BigBrain in a reasonable amount of time.

4.3.2 *Mapping of Subcortical Nuclei*

Since up to today no quantitative image analysis approach for cytoarchitectonic mapping of subcortical structures exists, it relies on careful visual analysis – imposing a possible threat to objectivity. This threat is partially reflected by the diverging numbers of subdivisions of the MGB and their topography (**Figure 4**) among different investigators reported during the last 60 years (Harrison and Howe, 1974; Hassler, 1959; Morel, 2007; Morest, 1964; Winer, 1984). The high-resolution maps of the MGB generated in the BigBrain in Study 2 provide an additional level of confidence since the revised deep-learning approach has helped to identify the subdivisions continuously throughout the whole extent of the metathalamus in the BigBrain. However, the existence of valid segmentations does not prove the approach to be valid for mapping subcortical nuclei per se. As demonstrated for cortical areas, the internal feature representations seemed to focus mainly on laminar differences. Further studies

evaluating internal feature representations on a subcortical level where laminar organization principles are mostly not abundant are needed to estimate the validity in this regard. For now, the revised deep-learning approach extends the current methodological options by providing additional verifications of anatomical plausibility on top of (subjective) visual analyses. This is useful for generating high-resolution maps but still requires neuroanatomical experts to carefully interpret and check the resulting maps.

4.4 Current and Future Relevance of High-Resolution Brain Maps in the 3D – BigBrain

4.4.1 *Linking BigBrain Histology with Neuroimaging*

Recent improvements of spatial resolution of modern neuroimaging have made it possible to measure laminar brain activity (Huber et al., 2018; Jia et al., 2021) and identify functional subdivisions of subcortical structures (Rijk et al., 2021), as well as functionally homogenous cortical columns in the auditory and visual cortex (Martino et al., 2015; Nasr et al., 2016). The spatial resolution of such submillimeter measurements requires a similarly high level of anatomical detail of a reference space. The interoperability and its anatomical detail make cytoarchitectonic maps in the BigBrain (Amunts et al., 2013) an important histological reference in this regard to support the physiologically driven MRI measurements with the underlying cellular architecture. This becomes especially apparent when comparing the BigBrain to the limited anatomical detail of the MNI space.

The BigBrain has been used to integrate histological data and neuroimaging data before. Most of the studies conducted comparisons of structural and functional correlations on a whole brain scale (Paquola et al., 2020b; Wei et al., 2019), or specific parts of cortical lobes (Paquola et al., 2019; Royer et al., 2020). During this thesis work generated maps provide more specific anatomical regions of interest in the BigBrain including visual cortical areas and subcortical nuclei of the metathalamus. The combination of whole-brain coverage in the BigBrain and a high level of detail, e.g. detailed subdivisions of the MGN, represents an advantage in comparison to other subcortical histological atlases (Ding et al., 2016; Krauth et al., 2010; Morel, 2007; Sadikot

et al., 2011) as well as probabilistic cytoarchitectonic atlases like the Julich-Brain (Amunts et al., 2020).

Current efforts of our research group incorporate the high anatomical detail of the BigBrain and combine it with deep-learning based cell-segmentations (Upschulte et al., 2022) and 3D cell-reconstructions (Dickscheid et al., 2019) to advance the options for extracting region-specific information from the BigBrain at the cellular level (Behuet et al., 2021; Dickscheid et al., 2019). High-resolution maps play an important role in this regard since they provide more specific targeting spaces for region-of-interest analyses. This allows the maps to be an important bridge between macroscale connectivity and local microscale circuitry. One future candidate analysis in this regard is the transition region between the primary and secondary visual cortex which hosts several locally restricted cytoarchitectonic phenomena (Amunts et al., 2000; Economo and Koskinas, 1925; Kiwitz et al., 2020) that are partly involved in interhemispheric transmission of visual information covering the vertical meridian of the visual field (Caspers et al., 2015; Clarke and Miklossy, 1990). Discovering these cytoarchitectonic peculiarities bears the potential to reveal new structural-functional insights that will help to further understand information processing in the visual system.

At the same time the single-subject character of the BigBrain shares the drawback of missing interindividual variability, much like Brodmann's first map (Brodmann, 1909). Probabilistic atlases are therefore still important to consider when linking neuroimaging data with a reference space. We acknowledged this circumstance by having calculated additional probabilistic maps of the human metathalamus utilizing the well-established atlas framework of the Julich-Brain (Amunts et al., 2020). Despite modern neuroimaging being able to generate in-vivo probabilistic maps of cortical (Glasser et al., 2016; Wang et al., 2015) and subcortical structures (García-Gomar et al., 2019; Iglesias et al., 2018; Najdenovska et al., 2018; Pauli et al., 2018; Saranathan et al., 2021), as well as functional probabilistic maps of neural networks (Dworetsky et al., 2021; Hermosillo et al., 2022), the unique advantage of the Julich-Brain constitutes its direct resemblance of the human brain's microanatomy at cellular resolution. MRI-based mapping on the other hand is technically restricted to lower spatial

resolutions and usually requires the aid of histological atlases to overcome the still limited discernibility - resulting in an often limited fit between the reference space and the atlas information (Ewert et al., 2018). The interoperability of the Julich-Brain further enables its cytoarchitectonic brain maps to be an important building block of multimodal atlases (Fischl and Sereno, 2018; Glasser et al., 2016; Toga et al., 2006) – already envisioned by the Vogts who thought to combine Brodmann’s cytoarchitectonic parcellations with their fiber architectonic parcellations (Zilles and Amunts, 2010).

4.4.2 Brain Simulation and Modelling

The benefit of reference spaces and atlases like the Julich-Brain and the BigBrain is not limited to neuroimaging data integration though. Besides studying structure-function relationships in the human brain, the BigBrain especially can be used to develop better and more realistic human brain models. Incorporating cytoarchitectonic parameters has recently led to the development of biologically valid models of the macaque visual system including cortical areas of different architectural types (Schmidt et al., 2018), as well as models of the human cerebellar granular layer (Florimbi et al., 2021) and first models of the human visual system (Pronold et al., 2018). However, such models usually lack quantitative thalamic input parameters, requiring them to be indirectly estimated (Schmidt et al., 2018). High-resolution subcortical maps in the BigBrain can enrich such brain modelling approaches directly by providing such cellular-level information (Kiwitz et al., 2022).

A crucial point in establishing realistic models is the incorporation of connectivity data. Recent advances in reconstructing the white matter fiber architecture from Nissl-stained glia cells (Schurr and Mezer, 2021) could allow the histology of the BigBrain to be complemented by connectivity data of cortical and subcortical areas (Kiwitz et al., 2022). Others have already used PLI to detect target sites for transcallosal fibers in the visual cortex of the BigBrain (Caspers et al., 2015) and cortex-like canonical circuits in the avian forebrain (Stacho et al., 2020). Combining such information with the cytoarchitecture can increase the biological validity of mechanistic models of the human sensory systems (Vecchi et al., 2021) and enable more detailed

models of thalamic gating phenomena (Xiong et al., 2020) on a systems level. By providing high-resolution topographical information, the BigBrain maps further contribute to improve personalized brain models of specific neurological pathologies like epilepsy in the Virtual BigBrain (Bernard and Jirsa, 2016; Triebkorn et al., 2021, unpublished results).

All mentioned areas of usage depend on the feasibility to integrate data into and out of the BigBrain reference space. Recent advances in image registration procedures have led to improved registrations to other reference spaces (Xiao et al., 2019), as well as the publicly available BigBrainWarp toolbox (Paquola et al., 2021) and the EBRAINS VoluBA toolbox for spatial anchoring in the BigBrain space (<https://ebrains.eu/service/voluba/>). As the BigBrain dataset is continuously expanded by cortical and subcortical cytoarchitectonic maps, as well as intracortical surface models (DeKraker et al., 2020; Paquola et al., 2020a; Wagstyl et al., 2020), it provides an increasingly rich resource for such integrative approaches (Kiwitz et al., 2022). The scrutiny and application of deep-learning based methods for cortical and subcortical brain mapping in the BigBrain contributes to this development.

4.4.3 Conclusion

This thesis work provides a first use-case for using deep-learning based cytoarchitectonic brain mapping for cortical and subcortical structures in the BigBrain on a routine basis. The application of the revised deep-learning based approach has provided maps of visual cortical areas and the subcortical MGB which correspond to cortical delineations based on the current profile-based approach as well as subcortical histological atlases. On top of the high accuracy and quality of the maps, the revised deep-learning approach incorporated traditional cytoarchitectonic features with a special emphasis on laminar features. The learned internal feature representations also compared well to profile shapes and border positions of the profile-based approach. Yet, further studies are still needed to analyze in how far cytoarchitectonic features of subcortical nuclei are represented and in how far such feature representations are actually used to segment brain areas. The use of the revised deep-learning based approach significantly increases the throughput

for mapping purposes in the BigBrain in comparison to the profile-based approach. Additionally, it enables an independent verification of subcortical nuclei maps beyond sole visual inspection. High-resolution cortical and subcortical maps enable the interoperable BigBrain to be used as a histological reference space that surpasses commonly used reference spaces like MNI in anatomical detail. This will allow future investigators to integrate the maps with high-resolution neuroimaging data as well as to develop better and more realistic human brain models.

5 References

- Abdollahi, R.O., Kolster, H., Glasser, M.F., Robinson, E.C., Coalson, T.S., Dierker, D., Jenkinson, M., van Essen, D.C., Orban, G.A., 2014. Correspondences between retinotopic areas and myelin maps in human visual cortex. *NeuroImage* 99, 509–524. <https://doi.org/10.1016/j.neuroimage.2014.06.042>.
- Amunts, K., Armstrong, E., Malikovic, A., Hömke, L., Mohlberg, H., Schleicher, A., Zilles, K., 2007. Gender-specific left–right asymmetries in human visual cortex. *J. Neurosci.* 27, 1356–1364. <https://doi.org/10.1523/JNEUROSCI.4753-06.2007>.
- Amunts, K., Bechmann, I., Nitsch, R., Paulsen, F., Schmitt, O., Wree, A., Zilles, K., 2010. Nervensystem und Sinnesorgane, in: Zilles, K., Tillmann, B.N. (Eds.), *Anatomie*. Springer, Berlin, pp. 599–764.
- Amunts, K., DeFelipe, J., Pennartz, C., Destexhe, A., Migliore, M., Ryvlin, P., Furber, S., Knoll, A., Bitsch, L., Bjaalie, J.G., Ioannidis, Y., Lippert, T., Sanchez-Vives, M.V., Goebel, R., Jirsa, V., 2022. Linking Brain Structure, Activity, and Cognitive Function through Computation. *eNeuro* 9. <https://doi.org/10.1523/ENEURO.0316-21.2022>.
- Amunts, K., Lepage, C., Borgeat, L., Mohlberg, H., Dickscheid, T., Rousseau, M.-É., Bludau, S., Bazin, P.-L., Lewis, L.B., Oros-Peusquens, A.-M., Shah, N.J., Lippert, T., Zilles, K., Evans, A.C., 2013. BigBrain: An ultrahigh-resolution 3D human brain model. *Science* 340, 1472–1475. <https://doi.org/10.1126/science.1235381>.
- Amunts, K., Malikovic, A., Mohlberg, H., Schormann, T., Zilles, K., 2000. Brodmann’s areas 17 and 18 brought into stereotaxic space—where and how variable? *NeuroImage* 11, 66–84. <https://doi.org/10.1006/nimg.1999.0516>.
- Amunts, K., Mohlberg, H., Bludau, S., Zilles, K., 2020. Julich-Brain: A 3D probabilistic atlas of the human brain’s cytoarchitecture. *Science* 369, 988–992. <https://doi.org/10.1126/science.abb4588>.
- Amunts, K., Morosan, P., Hilbig, H., Zilles, K., 2012. Auditory System, in: Mai, J.K., Paxinos, G. (Eds.), *The human nervous system*, 3rd ed. Elsevier Academic Press, Amsterdam, Boston.

- Amunts, K., Zilles, K., 2015. Architectonic Mapping of the Human Brain beyond Brodmann. *Neuron* 88, 1086–1107.
<https://doi.org/10.1016/j.neuron.2015.12.001>.
- Annese, J., Pitiot, A., Dinov, I.D., Toga, A.W., 2004. A myelo-architectonic method for the structural classification of cortical areas. *NeuroImage* 21, 15–26. <https://doi.org/10.1016/j.neuroimage.2003.08.024>.
- Bailey, P., Bonin, G. von, 1951. *The isocortex of man*. University of Illinois Press, Urbana, Illinois.
- Behuet, S., Bludau, S., Kedo, O., Schiffer, C., Dickscheid, T., Brandstetter, A., Massicotte, P., Omidyeganeh, M., Evans, A., Amunts, K., 2021. A high-resolution model of the human entorhinal cortex in the ‘BigBrain’ – use case for machine learning and 3D analyses, in: Amunts, K., Grandinetti, L., Lippert, T., Petkov, N. (Eds.), *Brain-Inspired Computing*, vol. 12339. Springer International Publishing, Cham, pp. 3–21.
- Bernard, C., Jirsa, V., 2016. Virtual Brain for neurological disease modeling. *Drug Discovery Today: Disease Models* 19, 5–10.
<https://doi.org/10.1016/j.ddmod.2017.05.001>.
- Brandstetter, A., Bolakhrif, N., Schiffer, C., Dickscheid, T., Mohlberg, H., Amunts, K., 2021. Deep learning-supported cytoarchitectonic mapping of the human lateral geniculate body in the BigBrain, in: *Brain-Inspired Computing*, Cham. 2021. Springer International Publishing, Cham, pp. 22–32.
- Brodmann, K., 1909. *Vergleichende Lokalisationslehre der Grosshirnrinde in ihren Prinzipien dargestellt aufgrund des Zellenbaues*. Barth, Leipzig.
- Burkhalter, A., Bernardo, K.L., 1989. Organization of corticocortical connections in human visual cortex. *Proceedings of the National Academy of Sciences of the United States of America* 86, 1071–1075.
<https://doi.org/10.1073/pnas.86.3.1071>.
- Calford, M.B., Aitkin, L.M., 1983. Ascending projections to the medial geniculate body of the cat: evidence for multiple, parallel auditory pathways through thalamus. *J. Neurosci.* 3, 2365–2380.
<https://doi.org/10.1523/JNEUROSCI.03-11-02365.1983>.
- Campbell, A.W., 1904. Histological studies on cerebral localisation. *Proc. R. Soc. Lond.* 72, 488–492. <https://doi.org/10.1098/rspl.1903.0077>.

- Caspary, D.M., Llano, D.A., 2017. Auditory thalamic circuits and GABAA receptor function: Putative mechanisms in tinnitus pathology. *Hearing Research* 349, 197–207. <https://doi.org/10.1016/j.heares.2016.08.009>.
- Caspers, S., Axer, M., Caspers, J., Jockwitz, C., Jütten, K., Reckfort, J., Grässel, D., Amunts, K., Zilles, K., 2015. Target sites for transcallosal fibers in human visual cortex - A combined diffusion and polarized light imaging study. *Cortex; a journal devoted to the study of the nervous system and behavior* 72, 40–53. <https://doi.org/10.1016/j.cortex.2015.01.009>.
- Chakravarty, M.M., Bertrand, G., Hodge, C.P., Sadikot, A.F., Collins, D.L., 2006. The creation of a brain atlas for image guided neurosurgery using serial histological data. *NeuroImage* 30, 359–376. <https://doi.org/10.1016/j.neuroimage.2005.09.041>.
- Clark, W.E., 1933. The Medical Geniculate Body and the Nucleus Isthmi. *Journal of anatomy* 67, 536-548.1.
- Clarke, S., Miklossy, J., 1990. Occipital cortex in man: Organization of callosal connections, related myelo- and cytoarchitecture, and putative boundaries of functional visual areas. *Journal of Comparative Neurology* 298, 188–214. <https://doi.org/10.1002/cne.902980205>.
- DeKraker, J., Lau, J.C., Ferko, K.M., Khan, A.R., Köhler, S., 2020. Hippocampal subfields revealed through unfolding and unsupervised clustering of laminar and morphological features in 3D BigBrain. *NeuroImage* 206, 116328. <https://doi.org/10.1016/j.neuroimage.2019.116328>.
- Dickscheid, T., Haas, S., Bludau, S., Glock, P., Huysegoms, M., Amunts, K., 2019. Towards 3D reconstruction of neuronal cell distributions from histological human brain sections. *Advances in Parallel Computing* 34, 223–239. <https://doi.org/10.3233/APC190016>.
- Ding, S.-L., Royall, J.J., Sunkin, S.M., Ng, L., Facer, B.A.C., Lesnar, P., Guillozet-Bongaarts, A., McMurray, B., Szafer, A., Dolbeare, T.A., Stevens, A., Tirrell, L., Benner, T., Caldejon, S., Dalley, R.A., Dee, N., Lau, C., Nyhus, J., Reding, M., Riley, Z.L., Sandman, D., Shen, E., van der Kouwe, A., Varjabedian, A., Write, M., Zollei, L., Dang, C., Knowles, J.A., Koch, C., Phillips, J.W., Sestan, N., Wohnoutka, P., Zielke, H.R., Hohmann, J.G., Jones, A.R., Bernard, A., Hawrylycz, M.J., Hof, P.R., Fischl, B., Lein, E.S.,

2016. Comprehensive cellular-resolution atlas of the adult human brain. *The Journal of comparative neurology* 524, 3127–3481.
<https://doi.org/10.1002/cne.24080>.
- Dworetsky, A., Seitzman, B.A., Adeyemo, B., Neta, M., Coalson, R.S., Petersen, S.E., Gratton, C., 2021. Probabilistic mapping of human functional brain networks identifies regions of high group consensus. *NeuroImage* 237, 118164. <https://doi.org/10.1016/j.neuroimage.2021.118164>.
- Economo, C.F. von, Koskinas, G.N., 1925. *Die Cytoarchitektonik der Hirnrinde des erwachsenen Menschen*. Springer, Berlin.
- Eickhoff, S.B., Stephan, K.E., Mohlberg, H., Grefkes, C., Fink, G.R., Amunts, K., Zilles, K., 2005a. A new SPM toolbox for combining probabilistic cytoarchitectonic maps and functional imaging data. *NeuroImage* 25, 1325–1335. <https://doi.org/10.1016/j.neuroimage.2004.12.034>.
- Eickhoff, S.B., Stephan, K.E., Mohlberg, H., Grefkes, C., Fink, G.R., Amunts, K., Zilles, K., 2005b. A new SPM toolbox for combining probabilistic cytoarchitectonic maps and functional imaging data. *NeuroImage* 25, 1325–1335. <https://doi.org/10.1016/j.neuroimage.2004.12.034>.
- Espinosa, J.S., Stryker, M.P., 2012. Development and plasticity of the primary visual cortex. *Neuron* 75, 230–249.
<https://doi.org/10.1016/j.neuron.2012.06.009>.
- Evans, A.C., Janke, A.L., Collins, D.L., Baillet, S., 2012. Brain templates and atlases. *NeuroImage* 62, 911–922.
<https://doi.org/10.1016/j.neuroimage.2012.01.024>.
- Ewert, S., Pletting, P., Li, N., Chakravarty, M.M., Collins, D.L., Herrington, T.M., Kühn, A.A., Horn, A., 2018. Toward defining deep brain stimulation targets in MNI space: A subcortical atlas based on multimodal MRI, histology and structural connectivity. *NeuroImage* 170, 271–282.
<https://doi.org/10.1016/j.neuroimage.2017.05.015>.
- Fischl, B., Sereno, M.I., 2018. Microstructural parcellation of the human brain. *NeuroImage* 182, 219–231.
<https://doi.org/10.1016/j.neuroimage.2018.01.036>.
- Flechsig, P.E., 1898. Neue Untersuchungen über die Markbildung in den menschlichen Grosshirnblättern. *Neurologisches Centralblatt* 17, 977–996.

- Florimbi, G., Torti, E., Masoli, S., D'Angelo, E., Leporati, F., 2021. Granular layer simulator: Design and multi-GPU simulation of the cerebellar granular layer. *Frontiers in computational neuroscience* 15, 630795. <https://doi.org/10.3389/fncom.2021.630795>.
- García-Gomar, M.G., Strong, C., Toschi, N., Singh, K., Rosen, B.R., Wald, L.L., Bianciardi, M., 2019. In vivo probabilistic structural atlas of the inferior and superior colliculi, medial and lateral geniculate nuclei and superior olivary complex in humans based on 7 Tesla MRI. *Frontiers in neuroscience* 13, 764. <https://doi.org/10.3389/fnins.2019.00764>.
- Gennari, F., 1782. *Francisci Gennari ... De peculiari structura cerebri nonnulisque ejus morbis. Paucae aliae anatom. observat. accedunt. ex regio typographeo, Parma.*
- Giedd, J.N., Blumenthal, J., Jeffries, N.O., Castellanos, F.X., Liu, H., Zijdenbos, A., Paus, T., Evans, A.C., Rapoport, J.L., 1999. Brain development during childhood and adolescence: a longitudinal MRI study. *Nat Neurosci* 2, 861–863. <https://doi.org/10.1038/13158>.
- Glasser, M.F., Coalson, T.S., Robinson, E.C., Hacker, C.D., Harwell, J., Yacoub, E., Ugurbil, K., Andersson, J., Beckmann, C.F., Jenkinson, M., Smith, S.M., van Essen, D.C., 2016. A multi-modal parcellation of human cerebral cortex. *Nature* 536, 171–178. <https://doi.org/10.1038/nature18933>.
- Gong, B., Naveed, S., Hafeez, D.M., Afzal, K.I., Majeed, S., Abele, J., Nicolaou, S., Khosa, F., 2019. Neuroimaging in Psychiatric Disorders: A Bibliometric Analysis of the 100 Most Highly Cited Articles. *Journal of Neuroimaging* 29, 14–33. <https://doi.org/10.1111/jon.12570>.
- Grünthal, E., 1934. *Der Zellbau im Thalamus der Säuger und dem Menschen.: Eine beschreibend und vergleichend anatomische Untersuschung.* *Journal für Psychologie und Neurologie* 46, 41–112.
- Harrison, J.M., Howe, M.E., 1974. Anatomy of the afferent auditory nervous system of mammals, in: Ades, H.W., Axelsson, A., Baird, I.L., v. Békésy, G., Boord, R.L., Campbell, C.B.G., Densert, O., Eldredge, D.H., Engström, H., Fex, J., Harrison, J.M., Henson, O.W., Howe, M.E., Iurato, S., Michelsen, A., Møller, A.R., Pfeiffer, R.R., Rauch, S., Rauch, I., Shaw, E.A.G., Wersäll, J., Wever, E.G., Keidel, W.D., Neff, W.D. (Eds.), *Auditory System*, 5 / 1. Springer Berlin Heidelberg, Berlin, Heidelberg, pp. 283–336.

- Hassler, R., 1959. Anatomy of the Thalamus, in: Schaltenbrand, G., Bailey, P. (Eds.), *Introduction to Stereotaxic Operations With an Atlas of the Human Brain*. Georg Thieme Verlag, Stuttgart, New York, NY.
- Herculano-Houzel, S., 2009. The human brain in numbers: a linearly scaled-up primate brain. *Frontiers in human neuroscience* 3, 31.
<https://doi.org/10.3389/neuro.09.031.2009>.
- Hermosillo, R.J., Moore, L.A., Fezcko, E., Dworetzky, A., Pines, A., Conan, G., Mooney, M.A., Randolph, A., Adeyemo, B., Earl, E., Perrone, A., Carrasco, C.M., Uriarte-Lopez, J., Snider, K., Doyle, O., Cordova, M., Nagel, B.J., Feldstein Ewing, S.W., Satterthwaite, T., Dosenbach, N., Gratton, C., Petersen, S., Miranda-Domínguez, Ó., Fair, D.A., 2022. A Precision Functional Atlas of Network Probabilities and Individual-Specific Network Topography. Preprint. <https://doi.org/10.1101/2022.01.12.475422>.
- Horn, A., Li, N., Dembek, T.A., Kappel, A., Boulay, C., Ewert, S., Tietze, A., Husch, A., Perera, T., Neumann, W.-J., Reisert, M., Si, H., Oostenveld, R., Rorden, C., Yeh, F.-C., Fang, Q., Herrington, T.M., Vorwerk, J., Kühn, A.A., 2019. Lead-DBS v2: Towards a comprehensive pipeline for deep brain stimulation imaging. *NeuroImage* 184, 293–316.
<https://doi.org/10.1016/j.neuroimage.2018.08.068>.
- Hubel, D.H., Wiesel, T.N., 1962. Receptive fields, binocular interaction and functional architecture in the cat's visual cortex. *The Journal of physiology* 160, 106–154. <https://doi.org/10.1113/jphysiol.1962.sp006837>.
- Huber, L., Tse, D.H.Y., Wiggins, C.J., Uludağ, K., Kashyap, S., Jangraw, D.C., Bandettini, P.A., Poser, B.A., Ivanov, D., 2018. Ultra-high resolution blood volume fMRI and BOLD fMRI in humans at 9.4 T: Capabilities and challenges. *NeuroImage* 178, 769–779.
<https://doi.org/10.1016/j.neuroimage.2018.06.025>.
- Iglesias, J.E., Insausti, R., Lerma-Usabiaga, G., Bocchetta, M., van Leemput, K., Greve, D.N., van der Kouwe, A., Fischl, B., Caballero-Gaudes, C., Paz-Alonso, P.M., 2018. A probabilistic atlas of the human thalamic nuclei combining ex vivo MRI and histology. *NeuroImage* 183, 314–326.
<https://doi.org/10.1016/j.neuroimage.2018.08.012>.

- Jenkinson, M., Beckmann, C.F., Behrens, T.E.J., Woolrich, M.W., Smith, S.M., 2012. FSL. *NeuroImage* 62, 782–790.
<https://doi.org/10.1016/j.neuroimage.2011.09.015>.
- Jia, K., Zamboni, E., Rua, C., Goncalves, N.R., Kemper, V., Ng, A.K.T., Rodgers, C.T., Williams, G., Goebel, R., Kourtzi, Z., 2021. A protocol for ultra-high field laminar fMRI in the human brain. *STAR Protocols* 2, 100415.
<https://doi.org/10.1016/j.xpro.2021.100415>.
- Kanwisher, N., McDermott, J., Chun, M.M., 1997. The Fusiform Face Area: A Module in Human Extrastriate Cortex Specialized for Face Perception. *J. Neurosci.* 17, 4302–4311. <https://doi.org/10.1523/JNEUROSCI.17-11-04302.1997>.
- Kiwitz, K., Brandstetter, A., Schiffer, C., Bludau, S., Mohlberg, H., Omidyeganeh, M., Massicotte, P., Amunts, K., 2022. Cytoarchitectonic Maps of the Human Metathalamus in 3D Space. *Front. Neuroanat.* 16, 837485. <https://doi.org/10.3389/fnana.2022.837485>.
- Kiwitz, K., Mohlberg, H., Brandstetter, A., Bludau, S., Amunts, K. Probabilistic cytoarchitectonic map of the human Corpus geniculatum laterale (CGL, LGB, metathalamus): EBRAINS. <https://doi.org/10.25493/1H7R-M3R>.
- Kiwitz, K., Mohlberg, H., Brandstetter, A., Bludau, S., Amunts, K. Probabilistic cytoarchitectonic map of the human Corpus geniculatum mediale (CGM, MGB, metathalamus): EBRAINS. <https://doi.org/10.25493/75TH-FE9>.
- Kiwitz, K., Schiffer, C., Brandstetter, A., Mohlberg, H., Amunts, K., Dickscheid, T. Reference delineations of the human Corpus geniculatum mediale (CGM, MGB, MGBv, MGBd, MGBm, metathalamus) in individual sections of the BigBrain: EBRAINS. <https://doi.org/10.25493/3SM6-HGM>.
- Kiwitz, K., Schiffer, C., Dickscheid, T., Amunts, K. Reference delineations of Area hOc1 (V1, 17, CalcS) in individual sections of the BigBrain: EBRAINS. <https://doi.org/10.25493/3GSV-T4A>.
- Kiwitz, K., Schiffer, C., Dickscheid, T., Amunts, K. Reference delineations of Area hOc2 (V2, 18) in individual sections of the BigBrain: EBRAINS. <https://doi.org/10.25493/8MKD-D77>.
- Kiwitz, K., Schiffer, C., Dickscheid, T., Amunts, K. Reference delineations of Area hOc3v (LingG) in individual sections of the BigBrain: EBRAINS. <https://doi.org/10.25493/DBZG-QZ>.

- Kiwitz, K., Schiffer, C., Dickscheid, T., Malikovic, A., Amunts, K. Reference delineations of Area hOc5 (LOC) in individual sections of the BigBrain: EBRAINS. <https://doi.org/10.25493/4027-K9Y>.
- Kiwitz, K., Schiffer, C., Spitzer, H., Dickscheid, T., Amunts, K. Filter Activations of Convolutional Neuronal Networks Used in Cytoarchitectonic Brain Mapping: EBRAINS. <https://doi.org/10.25493/Z6NG-4MU>.
- Kiwitz, K., Schiffer, C., Spitzer, H., Dickscheid, T., Amunts, K., 2020. Deep learning networks reflect cytoarchitectonic features used in brain mapping. *Sci Rep* 10, 22039. <https://doi.org/10.1038/s41598-020-78638-y>.
- Kolster, H., Peeters, R., Orban, G.A., 2010. The retinotopic organization of the human middle temporal area MT/V5 and its cortical neighbors. *The Journal of neuroscience : the official journal of the Society for Neuroscience* 30, 9801–9820. <https://doi.org/10.1523/JNEUROSCI.2069-10.2010>.
- Komura, D., Ishikawa, S., 2018. Machine Learning Methods for Histopathological Image Analysis. *Computational and Structural Biotechnology Journal* 16, 34–42. <https://doi.org/10.1016/j.csbj.2018.01.001>.
- Krauth, A., Blanc, R., Poveda, A., Jeanmonod, D., Morel, A., Székely, G., 2010. A mean three-dimensional atlas of the human thalamus: generation from multiple histological data. *NeuroImage* 49, 2053–2062. <https://doi.org/10.1016/j.neuroimage.2009.10.042>.
- Kujovic, M., Zilles, K., Malikovic, A., Schleicher, A., Mohlberg, H., Rottschy, C., Eickhoff, S.B., Amunts, K., 2013. Cytoarchitectonic mapping of the human dorsal extrastriate cortex. *Brain Struct Funct* 218, 157–172. <https://doi.org/10.1007/s00429-012-0390-9>.
- Lashley, K.S., Clark, G., 1946. The cytoarchitecture of the cerebral cortex of Ateles; a critical examination of architectonic studies. *J. Comp. Neurol.* 85, 223–305. <https://doi.org/10.1002/cne.900850207>.
- Litjens, G., Kooi, T., Bejnordi, B.E., Setio, A.A.A., Ciompi, F., Ghafoorian, M., van der Laak, Jeroen A.W.M., van Ginneken, B., Sánchez, C.I., 2017. A survey on deep learning in medical image analysis. *Medical image analysis* 42, 60–88. <https://doi.org/10.1016/j.media.2017.07.005>.
- Llano, D.A., Sherman, S.M., 2008. Evidence for nonreciprocal organization of the mouse auditory thalamocortical-corticothalamic projection systems.

- Journal of Comparative Neurology 507, 1209–1227.
<https://doi.org/10.1002/cne.21602>.
- Madabhushi, A., Lee, G., 2016. Image analysis and machine learning in digital pathology: Challenges and opportunities. *Medical image analysis* 33, 170–175. <https://doi.org/10.1016/j.media.2016.06.037>.
- Mai, J.K., Majtanik, M., 2018. Toward a Common Terminology for the Thalamus. *Front. Neuroanat.* 12, 114.
<https://doi.org/10.3389/fnana.2018.00114>.
- Mai, J.K., Majtanik, M., Paxinos, G., 2016. Atlas of the human brain, 4th ed. Elsevier AP, Amsterdam, 448 pp.
- Malikovic, A., Amunts, K., Schleicher, A., Mohlberg, H., Eickhoff, S.B., Wilms, M., Palomero-Gallagher, N., Armstrong, E., Zilles, K., 2007. Cytoarchitectonic analysis of the human extrastriate cortex in the region of V5/MT+: a probabilistic, stereotaxic map of area hOc5. *Cerebral Cortex* 17, 562–574. <https://doi.org/10.1093/cercor/bhj181>.
- Malikovic, A., Amunts, K., Schleicher, A., Mohlberg, H., Kujovic, M., Palomero-Gallagher, N., Eickhoff, S.B., Zilles, K., 2016. Cytoarchitecture of the human lateral occipital cortex: mapping of two extrastriate areas hOc4la and hOc4lp. *Brain structure & function* 221, 1877–1897.
<https://doi.org/10.1007/s00429-015-1009-8>.
- Malmierca, M.S., Anderson, L.A., Antunes, F.M., 2015. The cortical modulation of stimulus-specific adaptation in the auditory midbrain and thalamus: a potential neuronal correlate for predictive coding. *Front. Syst. Neurosci.* 9, 19. <https://doi.org/10.3389/fnsys.2015.00019>.
- Markov, N.T., Ercsey-Ravasz, M.M., Ribeiro Gomes, A.R., Lamy, C., Magrou, L., Vezoli, J., Misery, P., Falchier, A., Quilodran, R., Gariel, M.A., Sallet, J., Gamanut, R., Huissoud, C., Clavagnier, S., Giroud, P., Sappey-Marinier, D., Barone, P., Dehay, C., Toroczkai, Z., Knoblauch, K., van Essen, D.C., Kennedy, H., 2014. A weighted and directed interareal connectivity matrix for macaque cerebral cortex. *Cerebral Cortex* 24, 17–36.
<https://doi.org/10.1093/cercor/bhs270>.
- Martino, F. de, Moerel, M., Ugurbil, K., Goebel, R., Yacoub, E., Formisano, E., 2015. Frequency preference and attention effects across cortical depths in

- the human primary auditory cortex. PNAS 112, 16036–16041.
<https://doi.org/10.1073/pnas.1507552112>.
- Martino, F. de, Yacoub, E., Kemper, V., Moerel, M., Uludağ, K., Weerd, P. de, Ugurbil, K., Goebel, R., Formisano, E., 2018. The impact of ultra-high field MRI on cognitive and computational neuroimaging. *NeuroImage* 168, 366–382. <https://doi.org/10.1016/j.neuroimage.2017.03.060>.
- Mazziotta, J.C., Toga, A.W. (Eds.), 2002. *Brain mapping: The methods*, 2nd ed. Academic Press, Amsterdam, Boston.
- McCormick, D.A., Bal, T., 1994. Sensory gating mechanisms of the thalamus. *Current Opinion in Neurobiology* 4, 550–556. [https://doi.org/10.1016/0959-4388\(94\)90056-6](https://doi.org/10.1016/0959-4388(94)90056-6).
- Meynert, T., 1872a. *Der Bau der Gross-Hirnrinde und seine örtlichen Verschiedenheiten, nebst einem pathologisch-anatomischen Corollarium*. Heuser.
- Meynert, T., 1872b. Vom Gehirne der Säugethiere, in: Stricker, S. (Ed.), *Handbuch der Lehre von den Geweben des Menschen und der Thiere.*, Bd. 2. Verlag von Wilhelm Engelmann, pp. 694–808.
- Morel, A., 2007. *Stereotactic atlas of the human thalamus and basal ganglia*. Informa Healthcare, New York, 149 pp.
- Morest, D.K., 1964. The neuronal architecture of the medial geniculate body of the cat. *Journal of anatomy* 98, 611–630.
- Najdenovska, E., Alemán-Gómez, Y., Battistella, G., Descoteaux, M., Hagmann, P., Jacquemont, S., Maeder, P., Thiran, J.-P., Fornari, E., Bach Cuadra, M., 2018. In-vivo probabilistic atlas of human thalamic nuclei based on diffusion-weighted magnetic resonance imaging. *Sci Data* 5, 180270. <https://doi.org/10.1038/sdata.2018.270>.
- Nasr, S., Polimeni, J.R., Tootell, R.B.H., 2016. Interdigitated color- and disparity-selective columns within human visual cortical areas V2 and V3. *J. Neurosci.* 36, 1841–1857. <https://doi.org/10.1523/JNEUROSCI.3518-15.2016>.
- Orban, G.A., van Essen, D., Vanduffel, W., 2004. Comparative mapping of higher visual areas in monkeys and humans. *Trends in Cognitive Sciences* 8, 315–324. <https://doi.org/10.1016/j.tics.2004.05.009>.

- Owen, A.M., McMillan, K.M., Laird, A.R., Bullmore, E., 2005. N-back working memory paradigm: a meta-analysis of normative functional neuroimaging studies. *Human Brain Mapping* 25, 46–59.
<https://doi.org/10.1002/hbm.20131>.
- Pantelis, C., Velakoulis, D., McGorry, P.D., Wood, S.J., Suckling, J., Phillips, L.J., Yung, A.R., Bullmore, E.T., Brewer, W., Soulsby, B., Desmond, P., McGuire, P.K., 2003. Neuroanatomical abnormalities before and after onset of psychosis: a cross-sectional and longitudinal MRI comparison. *Lancet* 361, 281–288. [https://doi.org/10.1016/S0140-6736\(03\)12323-9](https://doi.org/10.1016/S0140-6736(03)12323-9).
- Paquola, C., Benkarim, O., DeKraker, J., Larivière, S., Frässle, S., Royer, J., Tavakol, S., Valk, S., Bernasconi, A., Bernasconi, N., Khan, A., Evans, A.C., Razi, A., Smallwood, J., Bernhardt, B.C., 2020a. Convergence of cortical types and functional motifs in the human mesiotemporal lobe. *eLife Sciences* 9. <https://doi.org/10.7554/eLife.60673>.
- Paquola, C., Royer, J., Lewis, L.B., Lepage, C., Glatard, T., Wagstyl, K., DeKraker, J., Toussaint, P.-J., Valk, S.L., Collins, L., Khan, A.R., Amunts, K., Evans, A.C., Dickscheid, T., Bernhardt, B., 2021. BigBrainWarp: Toolbox for integration of BigBrain 3D histology with multimodal neuroimaging. *bioRxiv*, 2021.05.04.442563. <https://doi.org/10.1101/2021.05.04.442563>.
- Paquola, C., Seidlitz, J., Benkarim, O., Royer, J., Klimes, P., Bethlehem, R.A.I., Larivière, S., Vos De Wael, R., Rodríguez-Cruces, R., Hall, J.A., Frauscher, B., Smallwood, J., Bernhardt, B.C., 2020b. A multi-scale cortical wiring space links cellular architecture and functional dynamics in the human brain. *PLOS Biology* 18, e3000979. <https://doi.org/10.1371/journal.pbio.3000979>.
- Paquola, C., Vos De Wael, R., Wagstyl, K., Bethlehem, R.A.I., Hong, S.-J., Seidlitz, J., Bullmore, E.T., Evans, A.C., Misic, B., Margulies, D.S., Smallwood, J., Bernhardt, B.C., 2019. Microstructural and functional gradients are increasingly dissociated in transmodal cortices. *PLOS Biology* 17, e3000284. <https://doi.org/10.1371/journal.pbio.3000284>.
- Pauli, W.M., Nili, A.N., Tyszka, J.M., 2018. A high-resolution probabilistic in vivo atlas of human subcortical brain nuclei. *Sci Data* 5, 180063.
<https://doi.org/10.1038/sdata.2018.63>.
- Peruzzi, D., Bartlett, E., Smith, P.H., Oliver, D.L., 1997. A monosynaptic GABAergic input from the inferior colliculus to the medial geniculate body in

- rat. *J. Neurosci.* 17, 3766–3777. <https://doi.org/10.1523/JNEUROSCI.17-10-03766.1997>.
- Pijnenburg, R., Scholtens, L.H., Ardesch, D.J., Lange, S.C. de, Wei, Y., van den Heuvel, M.P., 2021. Myelo- and cytoarchitectonic microstructural and functional human cortical atlases reconstructed in common MRI space. *NeuroImage* 239, 118274. <https://doi.org/10.1016/j.neuroimage.2021.118274>.
- Pronold, J., v. Meegen, A., Bakker, R., van Albada, S.J., 2018. Multi-area spiking network model of human visual cortex. INM-ICS Retreat, Jülich, Germany. <https://juser.fz-juelich.de/record/849855?ln=de>.
- Raichle, M.E., Snyder, A.Z., 2007. A default mode of brain function: a brief history of an evolving idea. *NeuroImage* 37, 1083-90; discussion 1097-9. <https://doi.org/10.1016/j.neuroimage.2007.02.041>.
- Ramón y Cajal, S., 1909. *Histologie du système nerveux de l'homme & des vertébrés*. Maloine, Paris, 1012 pp.
- Rijk, M.M. de, van den Hurk, J., Rahnama'i, M.S., van Koeveringe, G.A., 2021. Parcellation of human periaqueductal gray at 7-T fMRI in full and empty bladder state: The foundation to study dynamic connectivity changes related to lower urinary tract functioning. *Neurourology and Urodynamics* 40, 616–623. <https://doi.org/10.1002/nau.24602>.
- Rosenke, M., Weiner, K.S., Barnett, M.A., Zilles, K., Amunts, K., Goebel, R., Grill-Spector, K., 2017. A cross-validated cytoarchitectonic atlas of the human ventral visual stream. *NeuroImage* 170, 257–270. <https://doi.org/10.1016/j.neuroimage.2017.02.040>.
- Rottschy, C., Eickhoff, S.B., Schleicher, A., Mohlberg, H., Kujovic, M., Zilles, K., Amunts, K., 2007. Ventral visual cortex in humans: Cytoarchitectonic mapping of two extrastriate areas. *Human Brain Mapping* 28, 1045–1059. <https://doi.org/10.1002/hbm.20348>.
- Royer, J., Paquola, C., Larivière, S., Vos De Wael, R., Tavakol, S., Lowe, A.J., Benkarim, O., Evans, A.C., Bzdok, D., Smallwood, J., Frauscher, B., Bernhardt, B.C., 2020. Myeloarchitecture gradients in the human insula: Histological underpinnings and association to intrinsic functional connectivity. *NeuroImage* 216, 116859. <https://doi.org/10.1016/j.neuroimage.2020.116859>.

- Sadikot, A.F., Chakravarty, M.M., Bertrand, G., Rymar, V.V., Al-Subaie, F., Collins, D.L., 2011. Creation of Computerized 3D MRI-Integrated Atlases of the Human Basal Ganglia and Thalamus. *Front. Syst. Neurosci.* 5, 71. <https://doi.org/10.3389/fnsys.2011.00071>.
- Saint Marie, R.L., Stanforth, D., Jubelier, E., 1997. Substrate for rapid feedforward inhibition of the auditory forebrain. *Brain research* 765, 173–176. [https://doi.org/10.1016/S0006-8993\(97\)00654-9](https://doi.org/10.1016/S0006-8993(97)00654-9).
- Sanides, F., Vitzthum, H.G., 1965. Die Grenzerscheinungen am Rande der menschlichen Sehrinde. *Deutsche Zeitschrift f. Nervenheilkunde* 187, 708–719. <https://doi.org/10.1007/BF00243938>.
- Saranathan, M., Iglehart, C., Monti, M., Tourdias, T., Rutt, B., 2021. In vivo high-resolution structural MRI-based atlas of human thalamic nuclei. *Sci Data* 8, 275. <https://doi.org/10.1038/s41597-021-01062-y>.
- Sarkisov, S.A., Filimonoff, I.N., Preobrashenskaya, N.S., 1949. Cytoarchitecture of the human cortex cerebri. Medgiz, Moscow.
- Saxe, R., Kanwisher, N., 2003. People thinking about thinking people. The role of the temporo-parietal junction in “theory of mind”. *NeuroImage* 19, 1835–1842. [https://doi.org/10.1016/s1053-8119\(03\)00230-1](https://doi.org/10.1016/s1053-8119(03)00230-1).
- Schaltenbrand, G., Bailey, P. (Eds.), 1959. Introduction to Stereotaxic Operations With an Atlas of the Human Brain. Georg Thieme Verlag, Stuttgart, New York, NY.
- Schiffer, C., Kiwitz, K., Amunts, K., Dickscheid, T. Ultrahigh resolution 3D cytoarchitectonic map of Area hOc1 (V1, 17, CalcS) created by a Deep-Learning assisted workflow: EBRAINS. <https://doi.org/10.25493/DGEZ-Q93>.
- Schiffer, C., Kiwitz, K., Amunts, K., Dickscheid, T. Ultrahigh resolution 3D cytoarchitectonic map of Area hOc2 (V2, 18) created by a Deep-Learning assisted workflow: EBRAINS. <https://doi.org/10.25493/FVBY-84C>.
- Schiffer, C., Kiwitz, K., Amunts, K., Dickscheid, T. Ultrahigh resolution 3D cytoarchitectonic map of Area hOc3v (LingG) created by a Deep-Learning assisted workflow: EBRAINS. <https://doi.org/10.25493/PH0C-EKX>.
- Schiffer, C., Kiwitz, K., Amunts, K., Dickscheid, T. Ultrahigh resolution 3D cytoarchitectonic map of Area hOc5 (LOC) created by a Deep-Learning assisted workflow: EBRAINS. <https://doi.org/10.25493/2V62-TTG>.

- Schiffer, C., Kiwitz, K., Brandstetter, A., Mohlberg, H., Amunts, K., Dickscheid, T. Ultrahigh resolution 3D cytoarchitectonic map of the human Corpus geniculatum mediale (CGM, MGB, MGBv, MGBd, MGBm, metathalamus): EBRAINS. <https://doi.org/10.25493/PNY0-NCW>.
- Schiffer, C., Spitzer, H., Kiwitz, K., Unger, N., Wagstyl, K., Evans, A.C., Harmeling, S., Amunts, K., Dickscheid, T., 2021. Convolutional neural networks for cytoarchitectonic brain mapping at large scale. *NeuroImage* 240, 118327. <https://doi.org/10.1016/j.neuroimage.2021.118327>.
- Schleicher, A., Amunts, K., Geyer, S., Kowalski, T., Schormann, T., Palomero-Gallagher, N., Zilles, K., 2000. A stereological approach to human cortical architecture: identification and delineation of cortical areas. *Journal of chemical neuroanatomy* 20, 31–47. [https://doi.org/10.1016/s0891-0618\(00\)00076-4](https://doi.org/10.1016/s0891-0618(00)00076-4).
- Schleicher, A., Amunts, K., Geyer, S., Morosan, P., Zilles, K., 1999. Observer-Independent Method for Microstructural Parcellation of Cerebral Cortex: A Quantitative Approach to Cytoarchitectonics. *NeuroImage* 9, 165–177. <https://doi.org/10.1006/nimg.1998.0385>.
- Schleicher, A., Palomero-Gallagher, N., Morosan, P., Eickhoff, S.B., Kowalski, T., Vos, K. de, Amunts, K., Zilles, K., 2005. Quantitative architectural analysis: A new approach to cortical mapping. *Anatomy and embryology* 210, 373–386. <https://doi.org/10.1007/s00429-005-0028-2>.
- Schleicher, A., Zilles, K., 1990. A quantitative approach to cytoarchitectonics: Analysis of structural inhomogeneities in nervous tissue using an image analyser. *Journal of microscopy* 157, 367–381. <https://doi.org/10.1111/j.1365-2818.1990.tb02971.x>.
- Schmidt, M., Bakker, R., Shen, K., Bezgin, G., Diesmann, M., van Albada, S.J., 2018. A multi-scale layer-resolved spiking network model of resting-state dynamics in macaque visual cortical areas. *PLOS Computational Biology* 14, e1006359. <https://doi.org/10.1371/journal.pcbi.1006359>.
- Schmitt, O., Böhme, M., 2002. A Robust Transcortical Profile Scanner for Generating 2-D Traverses in Histological Sections of Richly Curved Cortical Courses. *NeuroImage* 16, 1103–1119. <https://doi.org/10.1006/nimg.2002.1159>.

- Schmitt, O., Hömke, L., Dümbgen, L., 2003. Detection of cortical transition regions utilizing statistical analyses of excess masses. *NeuroImage* 19, 42–63. [https://doi.org/10.1016/S1053-8119\(03\)00040-5](https://doi.org/10.1016/S1053-8119(03)00040-5).
- Scholtens, L.H., Reus, M.A. de, van den Heuvel, M.P., 2015. Linking contemporary high resolution magnetic resonance imaging to the von Economo legacy: A study on the comparison of MRI cortical thickness and histological measurements of cortical structure. *Human Brain Mapping* 36, 3038–3046. <https://doi.org/10.1002/hbm.22826>.
- Schurr, R., Mezer, A.A., 2021. The glial framework reveals white matter fiber architecture in human and primate brains. *Science* 374, 762–767. <https://doi.org/10.1126/science.abj7960>.
- Seitz, R.J., Bohm, C., Greitz, T., Roland, P.E., Eriksson, L., Blomqvist, G., Rosenqvist, G., Nordell, B., 1990. Accuracy and precision of the computerized brain atlas programme for localization and quantification in positron emission tomography. *Journal of cerebral blood flow and metabolism : official journal of the International Society of Cerebral Blood Flow and Metabolism* 10, 443–457. <https://doi.org/10.1038/jcbfm.1990.87>.
- Seitz, R.J., Höflich, P., Binkofski, F., Tellmann, L., Herzog, H., Freund, H.J., 1998. Role of the premotor cortex in recovery from middle cerebral artery infarction. *Arch Neurol* 55, 1081–1088. <https://doi.org/10.1001/archneur.55.8.1081>.
- Shen, D., Wu, G., Suk, H.-I., 2017. Deep Learning in Medical Image Analysis. *Annual review of biomedical engineering* 19, 221–248. <https://doi.org/10.1146/annurev-bioeng-071516-044442>.
- Sherman, S.M., Guillery, R.W., 2002. The role of the thalamus in the flow of information to the cortex. *Philosophical Transactions of the Royal Society B: Biological Sciences* 357, 1695–1708. <https://doi.org/10.1098/rstb.2002.1161>.
- Smith, G.E., 1907. A New Topographical Survey of the Human Cerebral Cortex, being an Account of the Distribution of the Anatomically Distinct Cortical Areas and their Relationship to the Cerebral Sulci. *Journal of Anatomy and Physiology* 41, 237–254.
- Spitzer, H., Amunts, K., Harmeling, S., Dickscheid, T., 2017. Parcellation of visual cortex on high-resolution histological brain sections using

- convolutional neural networks, in: 2017 IEEE 14th International Symposium on Biomedical Imaging (ISBI 2017): From Nano to Macro : Tuesday, 18 April-Friday, 21 April 2017, Melbourne Convention and Exhibition Centre, Melbourne, Australia. 2017 IEEE 14th International Symposium on Biomedical Imaging (ISBI 2017), Melbourne, Australia. 4/18/2017 - 4/21/2017. IEEE, Piscataway, NJ, pp. 920–923.
- Spitzer, H., Kiwitz, K., Amunts, K., Harmeling, S., Dickscheid, T., 2018. Improving Cytoarchitectonic Segmentation of Human Brain Areas with Self-supervised Siamese Networks, in: Frangi, A.F., Schnabel, J.A., Davatzikos, C., Alberola-López, C., Fichtinger, G. (Eds.), Medical image computing and computer assisted intervention – MICCAI 2018, vol. 11072. Springer, Cham, pp. 663–671.
- Stacho, M., Herold, C., Rook, N., Wagner, H., Axer, M., Amunts, K., Güntürkün, O., 2020. A cortex-like canonical circuit in the avian forebrain. *Science* 369. <https://doi.org/10.1126/science.abc5534>.
- Stoessl, A.J., Brooks, D.J., Eidelberg, D., 2011. Milestones in neuroimaging. *Movement Disorders* 26, 868–978. <https://doi.org/10.1002/mds.23679>.
- Strominger, N.L., Demarest, R.J., Laemle, L.B., 2012. Cerebral Cortex, in: Strominger, N.L., Demarest, R.J., Laemle, L.B. (Eds.), *Noback's Human Nervous System, Seventh Edition: Structure and Function*. Humana Press, Totowa, NJ, pp. 429–451.
- Talairach, J., Tournoux, P., 1988. *Co-Planar Stereotaxic Atlas of the Human Brain-3-Dimensional Proportional System: An Approach to Cerebral Imaging*. Georg Thieme Verlag.
- Thompson, P.M., Mega, M.S., Woods, R.P., Zoumalan, C.I., Lindshield, C.J., Blanton, R.E., Moussai, J., Holmes, C.J., Cummings, J.L., Toga, A.W., 2001. Cortical change in Alzheimer's disease detected with a disease-specific population-based brain atlas. *Cereb Cortex* 11, 1–16. <https://doi.org/10.1093/cercor/11.1.1>.
- Toga, A.W., Thompson, P.M., Mori, S., Amunts, K., Zilles, K., 2006. Towards multimodal atlases of the human brain. *Nature reviews. Neuroscience* 7, 952–966. <https://doi.org/10.1038/nrn2012>.

- Tootell, R.B., Switkes, E., Silverman, M.S., Hamilton, S.L., 1988. Functional anatomy of macaque striate cortex. II. Retinotopic organization. *J. Neurosci.* 8, 1531–1568.
- Triebkorn, P., Kusch, L., Gandolfi, D., Mapelli, J., Solinas, S., Fousek, J., Wang, H., Mangin, J.-F., Poupon, C., Migliore, M., Jirsa, V., 2021, unpublished results. The Virtual Big Brain in Epilepsy: Enhancing Individual Epilepsy Prediction with High Resolution Brain Modelling. HBP Summit 2021.
- Ts'o, D.Y., Zarella, M., Burkitt, G., 2009. Whither the hypercolumn? *The Journal of physiology* 587, 2791–2805.
<https://doi.org/10.1113/jphysiol.2009.171082>.
- Upschulte, E., Harmeling, S., Amunts, K., Dickscheid, T., 2022. Contour proposal networks for biomedical instance segmentation. *Medical image analysis* 77, 102371. <https://doi.org/10.1016/j.media.2022.102371>.
- van Buren, J.M., Borke, R.C., 1972. Variations and Connections of the Human Thalamus: 1 the Nuclei and Cerebral Connections of the Human Thalamus. 2 Variations of the Human Diencephalon. Springer Berlin / Heidelberg, Berlin, Heidelberg, 589 pp.
- van der Zwaag, W., Schäfer, A., Marques, J.P., Turner, R., Trampel, R., 2016. Recent applications of UHF-MRI in the study of human brain function and structure: a review. *NMR in Biomedicine* 29, 1274–1288.
<https://doi.org/10.1002/nbm.3275>.
- Vecchi, A.O., Varnet, L., Carney, L.H., Dau, T., Bruce, I.C., Verhulst, S., Majdak, P., 2021. A comparative study of eight human auditory models of monaural processing: Preprint. <https://arxiv.org/pdf/2107.01753>.
- Vicq-d'Azyr, F., 1786. *Traite d'Anatomie de Cerveau*. Chez Louis Duprat-Duverger, Paris.
- Vogt, C., Vogt, O., 1919. *Allgemeine Ergebnisse unserer Hirnforschung*. J.A. Barth, Leipzig.
- Vogt, C., Vogt, O., 1941. Thalamusstudien I-III: mit 140 Abbildungen. *Journal für Psychologie und Neurologie* 50.
- Wagstyl, K., Larocque, S., Cucurull, G., Lepage, C., Cohen, J.P., Bludau, S., Palomero-Gallagher, N., Lewis, L.B., Funck, T., Spitzer, H., Dickscheid, T., Fletcher, P.C., Romero, A., Zilles, K., Amunts, K., Bengio, Y., Evans, A.C.,

2020. BigBrain 3D atlas of cortical layers: Cortical and laminar thickness gradients diverge in sensory and motor cortices. *PLOS Biology* 18, e3000678. <https://doi.org/10.1371/journal.pbio.3000678>.
- Wang, L., Mruczek, R.E.B., Arcaro, M.J., Kastner, S., 2015. Probabilistic Maps of Visual Topography in Human Cortex. *Cerebral Cortex* 25, 3911–3931. <https://doi.org/10.1093/cercor/bhu277>.
- Wang, X., Chen, N., Zuo, Z., Xue, R., Jing, L., Yan, Z., Shen, D., Li, K., 2013. Probabilistic MRI brain anatomical atlases based on 1,000 Chinese subjects. *PloS one* 8, e50939. <https://doi.org/10.1371/journal.pone.0050939>.
- Wei, Y., Scholtens, L.H., Turk, E., van den Heuvel, M.P., 2019. Multiscale examination of cytoarchitectonic similarity and human brain connectivity. *Network neuroscience* 3, 124–137. https://doi.org/10.1162/netn_a_00057.
- Weiner, K.S., Zilles, K., 2016. The anatomical and functional specialization of the fusiform gyrus. *Neuropsychologia* 83, 48–62. <https://doi.org/10.1016/j.neuropsychologia.2015.06.033>.
- Winer, J.A., 1984. The human medial geniculate body. *Hearing Research* 15, 225–247. [https://doi.org/10.1016/0378-5955\(84\)90031-5](https://doi.org/10.1016/0378-5955(84)90031-5).
- Winer, J.A., Kelly, J.B., Larue, D.T., 1999. Neural architecture of the rat medial geniculate body. *Hearing Research* 130, 19–41. [https://doi.org/10.1016/S0378-5955\(98\)00216-0](https://doi.org/10.1016/S0378-5955(98)00216-0).
- Winer, J.A., Miller, L.M., Lee, C.C., Schreiner, C.E., 2005. Auditory thalamocortical transformation: structure and function. *Trends in neurosciences* 28, 255–263. <https://doi.org/10.1016/j.tins.2005.03.009>.
- Wree, A., Schleicher, A., Zilles, K., 1982. Estimation of volume fractions in nervous tissue with an image analyzer. *Journal of Neuroscience Methods* 6, 29–43. [https://doi.org/10.1016/0165-0270\(82\)90014-0](https://doi.org/10.1016/0165-0270(82)90014-0).
- Xiao, Y., Fonov, V., Chakravarty, M.M., Beriault, S., Al Subaie, F., Sadikot, A., Pike, G.B., Bertrand, G., Collins, D.L., 2017. A dataset of multi-contrast population-averaged brain MRI atlases of a Parkinson's disease cohort. *Data in brief* 12, 370–379. <https://doi.org/10.1016/j.dib.2017.04.013>.
- Xiao, Y., Lau, J.C., Anderson, T., DeKraker, J., Collins, D.L., Peters, T., Khan, A.R., 2019. An accurate registration of the BigBrain dataset with the MNI PD25 and ICBM152 atlases. *Sci Data* 6, 210. <https://doi.org/10.1038/s41597-019-0217-0>.

- Xing, F., Yang, L., 2016. Robust Nucleus/Cell Detection and Segmentation in Digital Pathology and Microscopy Images: A Comprehensive Review. *IEEE reviews in biomedical engineering* 9, 234–263.
<https://doi.org/10.1109/RBME.2016.2515127>.
- Xiong, C., Liu, X., Kong, L., Yan, J., 2020. Thalamic gating contributes to forward suppression in the auditory cortex. *PloS one* 15, e0236760.
<https://doi.org/10.1371/journal.pone.0236760>.
- Zilles, K., Amunts, K., 2010. Centenary of Brodmann's map—conception and fate. *Nature Reviews Neuroscience* 11, 139–145.
<https://doi.org/10.1038/nrn2776>.
- Zilles, K., Amunts, K., 2012. Architecture of the Cerebral Cortex, in: Mai, J.K., Paxinos, G. (Eds.), *The human nervous system*, 3rd ed. Elsevier Academic Press, Amsterdam, Boston, pp. 836–895.
- Zilles, K., Schleicher, A., Kretschmann, H.-J., 1978. A quantitative approach to cytoarchitectonics. *Anatomy and embryology* 153, 195–212.
<https://doi.org/10.1007/BF00343374>.
- Zilles, K., Schleicher, A., Palomero-Gallagher, N., Amunts, K., 2002. Quantitative Analysis of Cyto- and Receptor Architecture of the Human Brain, in: Mazziotta, J.C., Toga, A.W. (Eds.), *Brain mapping: The methods*, 2nd ed. Academic Press, Amsterdam, Boston, pp. 573–602.

Acknowledgments

First and foremost, I would like to express my deepest gratitude to my supervisor Prof. Dr. Katrin Amunts. I owe much of what I have learned over the past few years to her guidance and exceptional expertise. It was an honor for me to realize this project under her supervision. I would like to thank Prof. Dr. Rüdiger Seitz for taking over the co-supervision of my PhD project. The meetings we had, especially at the beginning, were encouraging and guiding with regard to the integration of neuroimaging data. In addition, I would like to thank all my colleagues and friends at the Vogt Institute and INM-1. I would like to give special thanks to some of them:

- Ariane Bruno for giving me joyful days in the office and making sure I don't miss any important deadlines ;)
- Kimberley Lothmann for her happy nature and keeping in check my chatty nature with her even chattier nature ;)
- Christian Schiffer for helping me to open Pandora's box of computation and artificial neural networks
- Manuel Marx for always having my back
- Anna Stössel for helping me to solve all non-science related issues with ease and friendliness
- Marcel Huysegoms for giving me new motivation and pursue new ideas
- Casey Paquola for re-awakening my interest in my own work and encouraging me to find new solutions
- Andrea Brandstetter for getting me excited about the world beneath the cerebral cortex
- Evelyn Oermann for sharing her vast neuroanatomy knowledge and supporting my passion for teaching
- Sebastian Bludau for introducing me to important methodological approaches
- Felix Ströckens for encouraging me to believe in my writing skills and helping me to make this thesis more interesting to read

Last but not least, I would like to thank my love Rita. You not only gave me confidence in my abilities during this crucial period of my life, but also encouraged me to find my own way and rely on my strengths. You are the greatest gift for me.